

NASA Contractor Report 3410

NASA  
CR  
3410  
c. 1

# Atmospheric Studies Related to Aerospace Activities and Remote Sensing Technology

N. D. Sze, R. G. Isaacs, M. Ko,  
and M. B. McElroy

CONTRACT NAS1-15943  
MARCH 1981

**NASA**

LOAN COPY  
APWL TECHNICAL  
KIRTLAND AFB

0062284



TECH LIBRARY KAFB, NM



NASA Contractor Report 3410

# Atmospheric Studies Related to Aerospace Activities and Remote Sensing Technology

N. D. Sze, R. G. Isaacs, M. Ko,  
and M. B. McElroy  
*Atmospheric and Environmental Research, Inc.*  
*Cambridge, Massachusetts*

Prepared for  
Langley Research Center  
under Contract NAS1-15943

**NASA**

National Aeronautics  
and Space Administration

**Scientific and Technical  
Information Branch**

1981



## TABLE OF CONTENTS

	Page
1. INTRODUCTION . . . . .	1
2. MODEL SENSITIVITY STUDIES . . . . .	3
2.1 Overview . . . . .	3
2.2 Model Results . . . . .	5
2.3 Perturbation Studies . . . . .	9
2.4 Concluding Remarks . . . . .	21
3. TWO-DIMENSIONAL ZONAL MEAN MODELING . . . . .	22
3.1 Background . . . . .	22
3.2 Eulerian Mean Model . . . . .	28
3.3 Generalized Lagrangian Mean (GLM) Zonal Models . . . . .	36
3.4 Concluding Remarks . . . . .	42
4. REMOTE SENSING . . . . .	45
4.1 Background . . . . .	45
4.2 Role of Earth Curvature and Scattering in Diurnal Photo- chemical Modeling . . . . .	47
4.3 Optical Paths in a Spherical Shell Atmosphere . . . . .	49
4.3.1 Geometric Considerations . . . . .	49
4.3.2 Air Mass Factor Formulation . . . . .	50
4.3.3 The Chapman Function . . . . .	52
4.3.4 Other Analytical Treatments . . . . .	56
4.3.5 Numerical Forms (including refractive effects) . . . . .	57
4.3.6 Summary . . . . .	61
4.4 Treatment of Multiple Scattering in the Spherical Shell Geometry . . . . .	63
4.4.1 The General Problem . . . . .	63
4.4.2 Locally Plane-Parallel Approximation . . . . .	65
4.4.3 Method of Solution . . . . .	67
4.4.4 Single Scattering Results . . . . .	72
4.4.5 Multiple Scattering Results . . . . .	81

	Page
4.5 Application to Diurnally Dependent Photodissociation Rates . . . . .	86
4.6 Diurnal Calculations . . . . .	90
4.6.1 Role of Sphericity . . . . .	93
4.6.2 Role of Molecular Scattering . . . . .	94
4.7 Implications for Remote Sensing . . . . .	95
5. SUMMARY AND RECOMMENDATIONS . . . . .	101
5.1 Model Sensitivity Studies . . . . .	101
5.2 Two-Dimensional Zonal-Mean Modeling . . . . .	102
5.3 Remote Sensing . . . . .	102
APPENDIX A - Earth-Sun Geometry . . . . .	104
APPENDIX B - Procedure for Refracted Air Mass Calculation . . . . .	107
APPENDIX C - Integral Quadrature Technique . . . . .	110
APPENDIX D - Numerical Procedure for Diurnal Calculation . . . . .	114
APPENDIX E - Initialization of Lagrangian Trajectory . . . . .	117
APPENDIX F - High Altitude Aircraft Emissions . . . . .	120
REFERENCES . . . . .	124

## 1. INTRODUCTION

This report describes the results of a three phase program of atmospheric studies related to aerospace activities and remote sensing technology performed by Atmospheric and Environmental Research, Inc. (AER) under the sponsorship of NASA/Langley Research Center (contract no. NAS1-15943). The period of performance for this work is August 1979 - May 1980. Parallel efforts were undertaken to investigate: (a) the sensitivity of one-dimensional photochemical model simulations of projected supersonic aircraft operations to chemical rate constant data and parameterization of vertical eddy diffusion, (b) the feasibility of the development of a two-dimensional modeling capability based on the Generalized Lagrangian Mean (GLM) methodology, and (c) the role of multiple scattering and earth sphericity on the computation of photodissociation rates near dawn and dusk and subsequent effects on diurnal variations of stratospheric trace species.

The document is organized into three technical sections and six supporting appendices. Section 2 describes the results of 1-D model sensitivity studies of stratospheric ozone perturbation for a hypothetical fleet of high altitude aircraft. The implication of three models of OH chemistry and two choices of eddy diffusion profiles are discussed. In Section 3, approaches to formulation of multidimensional models are reviewed with emphasis on two-dimensional zonal-mean modeling. Difficulties associated with parameterization of eddy transport terms in Eulerian approaches are discussed and the Generalized Lagrangian Mean (GLM) formalism is presented as an alternative methodology. Several crucial areas that require further investigation to practically apply GLM to zonal modeling are identified. In Section 4, possible approaches and

approximations are examined for incorporating both sphericity and multiple scattering in diurnal calculations for free radical species with emphasis on behavior near dawn and dusk. Diurnally dependent photodissociation rates and species concentrations are evaluated using a first order technique and an approach to incorporate a priori information on diurnal variations of photochemically active species within occultation based inversion algorithms is discussed. A general summary is included in Section 5.

We would like to thank R. Specht for his responsive programming support during the course of this work and K.K. Tung for fruitful discussions during the preparation of Section 3 of this report.

## 2. MODEL SENSITIVITY STUDIES

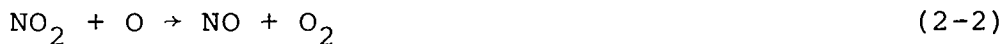
### 2.1 Overview

Earlier model calculations (Crutzen, 1970; Johnston, 1971; McElroy et al., 1974; CIAP, 1974) indicate that a potential fleet of operations of supersonic aircraft as contemplated by the United States in 1970 (500 aircraft flying approximately 7 hours per day at 17-18 km) could lead to major reduction in the stratospheric column O<sub>3</sub> abundance and thus cause an increase in the flux of ultra-violet radiation reaching the Earth's surface. This could result in a variety of environmental consequences, including a possible increase in the incidence of skin cancer (McDonald, 1971).

Removal of O<sub>3</sub> by aircraft injectant NO<sub>x</sub> radicals is primarily due to the pair of reactions



followed by,



The natural source for NO<sub>x</sub> in the stratosphere is thought to emanate from the reaction of O(<sup>1</sup>D) with N<sub>2</sub>O (Nicolet and Vergison, 1971; Crutzen, 1971; McElroy and McConnell, 1971),



Much of the revision in model predictions since 1976 (Duewer et al., 1977; Turco et al., 1978) may be ascribed to a change in the rate constant for the reaction of NO with HO<sub>2</sub>,



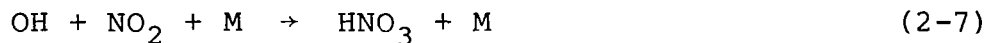
Recent measurements (Howard and Evenson, 1977) indicate that the rate constant for reaction (2-4) is faster than previously thought, by about a factor of 30. An increase in the rate constant for reaction (2-4) tends to shift the equilibrium in  $\text{HO}_x$  from  $\text{HO}_2$  toward  $\text{OH}$ . Below 30 km, removal of ozone by  $\text{HO}_x$  radicals proceeds mainly by,



We may note that reactions (2-5a) and (2-4) followed by photolysis of  $\text{NO}_2$ ,



do not affect odd oxygen removal. Thus addition of  $\text{NO}$  would reduce the catalytic role of  $\text{HO}_x$  as described by equations (2-5a,b). Furthermore, an increase in  $\text{OH}$  causes an increase in the rate for the reaction,



with subsequent decrease in the concentration of the free nitrogen radicals ( $\text{NO} + \text{NO}_2$ ) and reduction in the efficiency of the nitrogen cycle as a sink for odd oxygen.

There is little doubt that  $\text{OH}$  plays a pivotal role in stratospheric chemistry and in the perturbed environment. While the kinetic data base for  $\text{HO}_x$  reactions have been significantly improved over the past years, remaining uncertainties in  $\text{HO}_x$  chemistry still, perhaps, represent the

largest source of error for model predictions. In fact, a comparison between model calculations and observations reveals several significant discrepancies which might be attributed to errors in the calculated OH concentrations in the altitude region 15-35 km. It was argued elsewhere (Sze, 1978; Sze and Ko (1980) that significantly lower stratospheric OH concentrations than those calculated by current models are needed to account for the observed gradients of ClO (Anderson et al., 1979) and for the observed ratios of HNO<sub>3</sub>/NO<sub>2</sub> (NASA, 1977, 1979; McConnell and Evans, 1978) and HF/HCl (Sze, 1978).

Another area of major uncertainty concerns atmospheric transport of trace species. Current one-dimensional models parameterize vertical transport by the so-called eddy diffusion coefficients which were mainly derived from observation of N<sub>2</sub>O and CH<sub>4</sub>. These models therefore ignore horizontal transport, while the natural distribution of ozone exhibits significant latitudinal and seasonal variations.

In order to address the uncertainties associated with atmospheric transport and chemistry, a series of models will be investigated in an attempt to quantify the sensitivity of O<sub>3</sub> perturbations to different models of NO<sub>x</sub> injection by aircraft operations. Our approach will emphasize the uncertainties in the stratospheric OH distributions and their implications for perturbation studies.

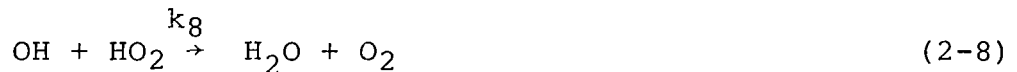
## 2.2 Model Results

The results presented in this section are calculated by a one-dimensional model (Sze, 1978; Sze and Ko, 1979) with the rate data for oxygen-nitrogen-chlorine reactions taken from NASA (1979), while those for HO<sub>x</sub> reactions are discussed in the text. The aircraft emission characteristics corresponding to different emission indices, fleet

size and engine types are summarized in Appendix F. The model atmosphere was taken from U.S. Standard Atmosphere Supplement (1966). The diffusion coefficients ( $K_z$ ) for most studies presented here taken from Wofsy (1976), although in some model studies, we also consider other choices of  $K_z$ .

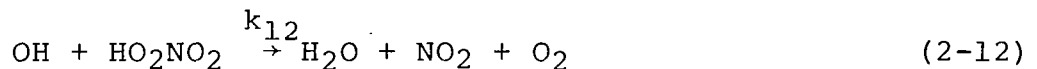
We shall consider three models (A, B and C) of OH chemistry that could have important implications for  $O_3$  perturbations associated with aircraft operations. The key characteristics of models A, B and C are defined in Table 2-1.

Model A uses the rate constants for key  $HO_x$  reactions as recommended by NASA (1979). Model B uses somewhat different rate constants for the following reactions,



The rate constants  $k_8$ ,  $k_9$ ,  $k_{10}$  and  $k_{11}$  in model B are adjusted within their experimental uncertainties so as to give a lower OH concentration above 18 km.

Model C is designed to investigate the possibility of reducing  $HO_x$  concentration, particularly in the lower stratosphere, by the reaction of OH with  $HO_2NO_2$ ,



Reaction (2-12) could be a major sink for  $HO_x$  if the more

TABLE 2-1 (a)

Reactions of Major Importance to Stratospheric OH Concentration\*

REACTION	MODEL A	MODEL B	MODEL C
$\text{OH} + \text{HO}_2 \rightarrow \text{H}_2\text{O} + \text{O}_2$	2.4(7)	1.2(7)	2.4(7)
$\text{OH} + \text{HNO}_3 \rightarrow \text{H}_2\text{O} + \text{NO}_3$	4.8(4)	9.0(4)	4.8(4)
$\text{HO}_2 + \text{HO}_2 \rightarrow \text{H}_2\text{O}_2 + \text{O}_2$	1.5(6)	3.0(6)	1.5(6)
$\text{OH} + \text{O}_3 \rightarrow \text{H}_2\text{O} + \text{O}_2$	$9.6(5) \exp(-\frac{940}{T})$	$1.2(6) \exp(-\frac{800}{T})$	$9.6(5) \exp(-\frac{940}{T})$
$\text{HO}_2 + \text{NO}_2 \xrightarrow{\text{M}} \text{HO}_2\text{NO}_2$	0	0	NASA (1979)
$\text{HO}_2\text{NO}_2 + h\nu \rightarrow \text{HO}_2 + \text{NO}_2$			Molina & Molina (1980)
$\text{HO}_2\text{NO}_2 \xrightarrow{\text{M}} \text{HO}_2 + \text{NO}_2$			Graham et al. (1978)
$\text{HO}_2\text{NO}_2 + \text{OH} \rightarrow \text{H}_2\text{O} + \text{NO}_2 + \text{O}_2$	3.0(5)	3.0(5)	$3.0(5) \exp(-\frac{200}{T})$
$\text{HO}_2\text{NO}_2 + \text{O} \rightarrow \text{H}_2\text{O} + \text{NO}_2 + \text{O}_2$	6.0(2)	6.0(2)	6.0(2)
$\text{HO}_2\text{NO}_2 + \text{Cl} \rightarrow \text{HCl} + \text{NO}_2 + \text{O}_2$	1.8(5)	1.8(5)	1.8(5)

\*Two body rates are in unit of  $\text{m}^3 \text{mol}^{-1} \text{s}^{-1}$

TABLE 2-1 (b)

Reactions of Major Importance to Stratospheric OH Concentration\*

REACTION	MODEL A	MODEL B	MODEL C
$\text{OH} + \text{HO}_2 \rightarrow \text{H}_2\text{O} + \text{O}_2$	4(-11)	2(-10)	4(-11)
$\text{OH} + \text{HNO}_3 \rightarrow \text{H}_2\text{O} + \text{NO}_3$	8.0(-14)	1.5(-13)	8.0(-14)
$\text{HO}_2 + \text{HO}_2 \rightarrow \text{H}_2\text{O}_2 + \text{O}_2$	2.5(-12)	5(-12)	2.5(-12)
$\text{OH} + \text{O}_3 \rightarrow \text{H}_2\text{O} + \text{O}_2$	$1.6(-12)\exp(-\frac{940}{T})$	$2(-12)\exp(-\frac{800}{T})$	$1.6(-12)\exp(-\frac{940}{T})$
$\text{HO}_2 + \text{NO}_2 \xrightarrow{\text{M}} \text{HO}_2\text{NO}_2$	0	0	NASA (1979)
$\text{HO}_2\text{NO}_2 + h\nu \rightarrow \text{HO}_2 + \text{NO}_2$			Molina & Molina (1980)
$\text{HO}_2\text{NO}_2 \xrightarrow{\text{M}} \text{HO}_2 + \text{NO}_2$			Graham et al. (1978)
$\text{HO}_2\text{NO}_2 + \text{OH} \rightarrow \text{H}_2\text{O} + \text{NO}_2 + \text{O}_2$	5.0(-13)	5.0(-13)	$1.5(-11)\exp(-\frac{200}{T})$
$\text{HO}_2\text{NO}_2 + \text{O} \rightarrow \text{H}_2\text{O} + \text{NO}_2 + \text{O}_2$	1.0(-15)	1.0(-15)	1.0(-15)
$\text{HO}_2\text{NO}_2 + \text{Cl} \rightarrow \text{HCl} + \text{NO}_2 + \text{O}_2$	3(-13)	3(-13)	3(-13)

\* Same as Table 2-1 (a) except that  
Two body rates are in units of  $\text{cm}^3 \text{ molecule}^{-1} \text{ s}^{-1}$

recent cross-section data for HO<sub>2</sub>NO<sub>2</sub> reported by Molina and Molinda (1980) are valid and if k<sub>12</sub> is faster than 1.2x10<sup>6</sup> m<sup>3</sup> mol<sup>-1</sup> s<sup>-1</sup> (2x10<sup>-12</sup> cm<sup>3</sup> s<sup>-1</sup>).

Figure (2-1) shows the calculated OH profiles for models A, B and C. Note that the OH concentration in model B is about a factor of two smaller than that in model A above ~30 km, while the OH concentration in model C is about a factor of two to three smaller than that in model A below ~30 km. It should be noted that current measurements of OH are restricted above 30 km. Concentrations of OH below 30 km can only be indirectly inferred from other observed quantities such as the gradients of ClO and the HNO<sub>3</sub>:NO<sub>2</sub> and HF:HCl ratios.

Figures (2-2) through (2-4) show the calculated profiles of ClO, HNO<sub>3</sub>/NO<sub>2</sub> and HF/HCl, along with available observations. We may note that results from Model C provide significantly better agreement with observations (Figures 2-2, 2-3, 2-4) than model A.

### 2.3 Perturbation Studies

For each model of HO<sub>x</sub> chemistry, we consider two different NO<sub>x</sub> injection altitudes, one at 15-16 km and the other at 20-21 km. Table 2-2 summarizes the calculated column perturbations which may result from the operation of 1000 aircraft, flying 7 hours per day at two different cruise altitudes. Figures (2-5a,b) and (2-6a,b) present the calculated local ozone and NO<sub>x</sub> perturbations associated with supersonic aircraft operation.

Model A predicts increases of about 1.6 and 4 percent in column ozone for the 15 and 20 km injections respectively. On the other hand, model C predicts a small increase in column ozone for the low altitude injection but a fairly large decrease of about 6 percent for the high altitude injection case. The calculated column ozone perturbations

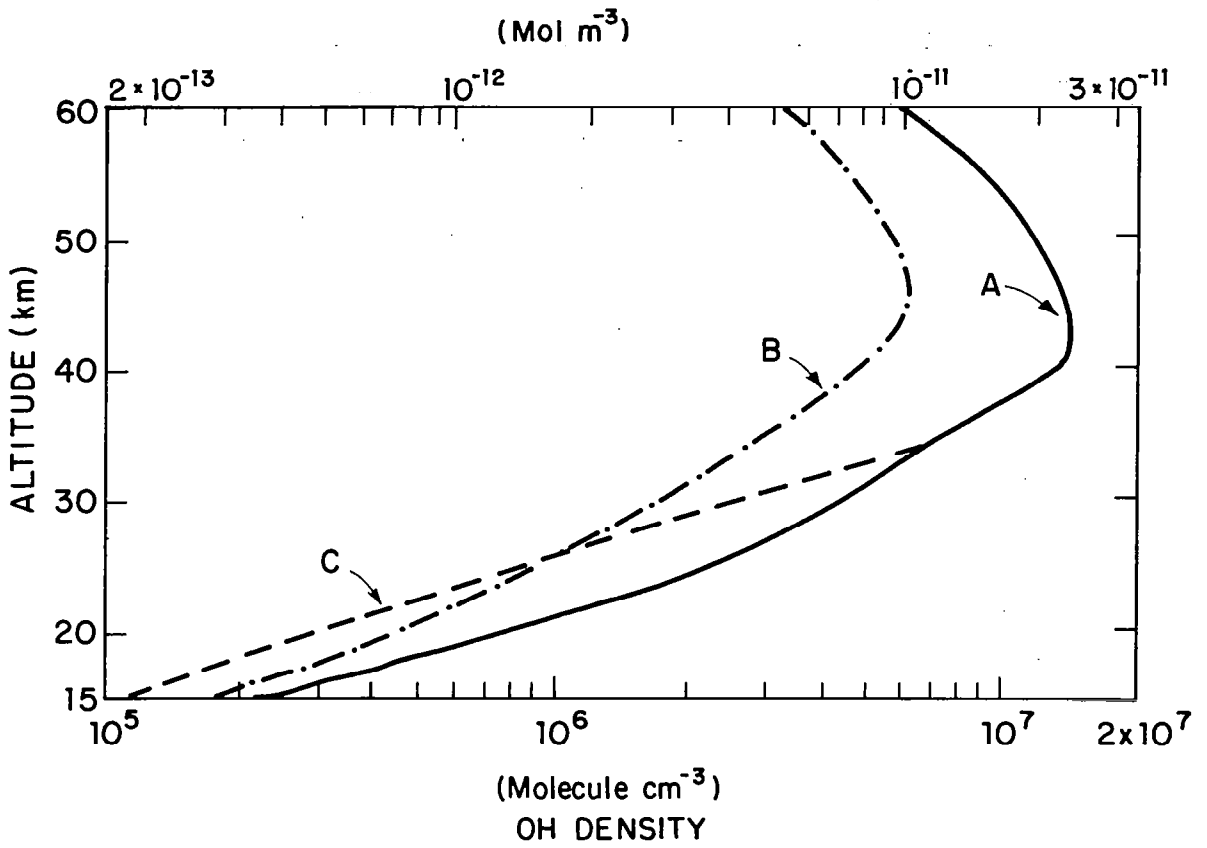


Figure 2-1

Calculated OH profiles for models A, B and C. The rate constants for  $\text{HO}_x$  reactions of different models are given in Table 2-1.

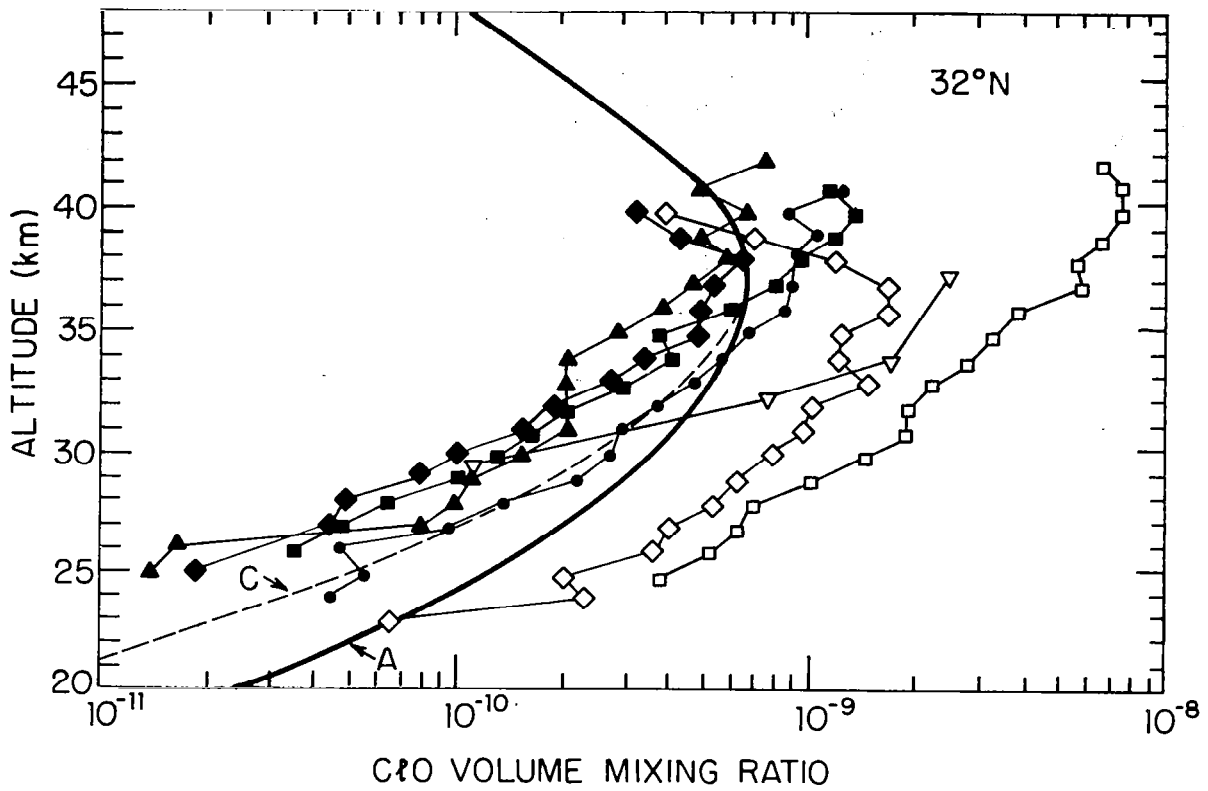


Figure 2-2

Calculated altitude profiles of ClO mixing ratio corresponding to 41° zenith angle. The observations from Anderson et al. (1979) and Menzies (1979) are included for comparison.

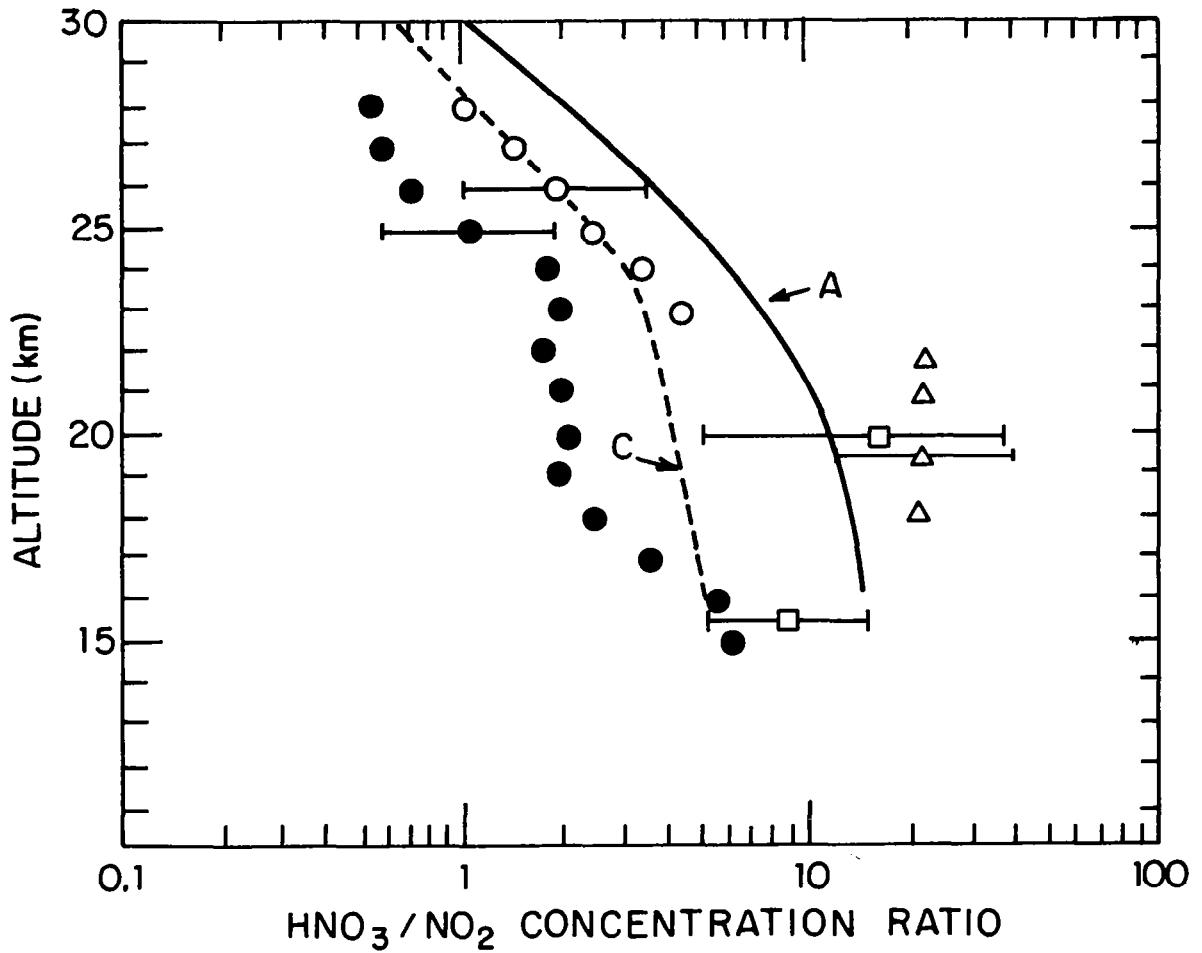


Figure 2-3

Calculated ratio of HNO<sub>3</sub>/NO<sub>2</sub> from models A and C. The computed ratios correspond to sunset ( $\chi = 90^\circ$ ) at 30°N. The data points are:

- Evans et al. (1976) sunset
- Harries et al. (1976) Harries (1978) noon 44°N
- Fontanella et al. (1975) sunset 45-50°N
- △ Lowenstein et al. (1978) daytime 20-40°N

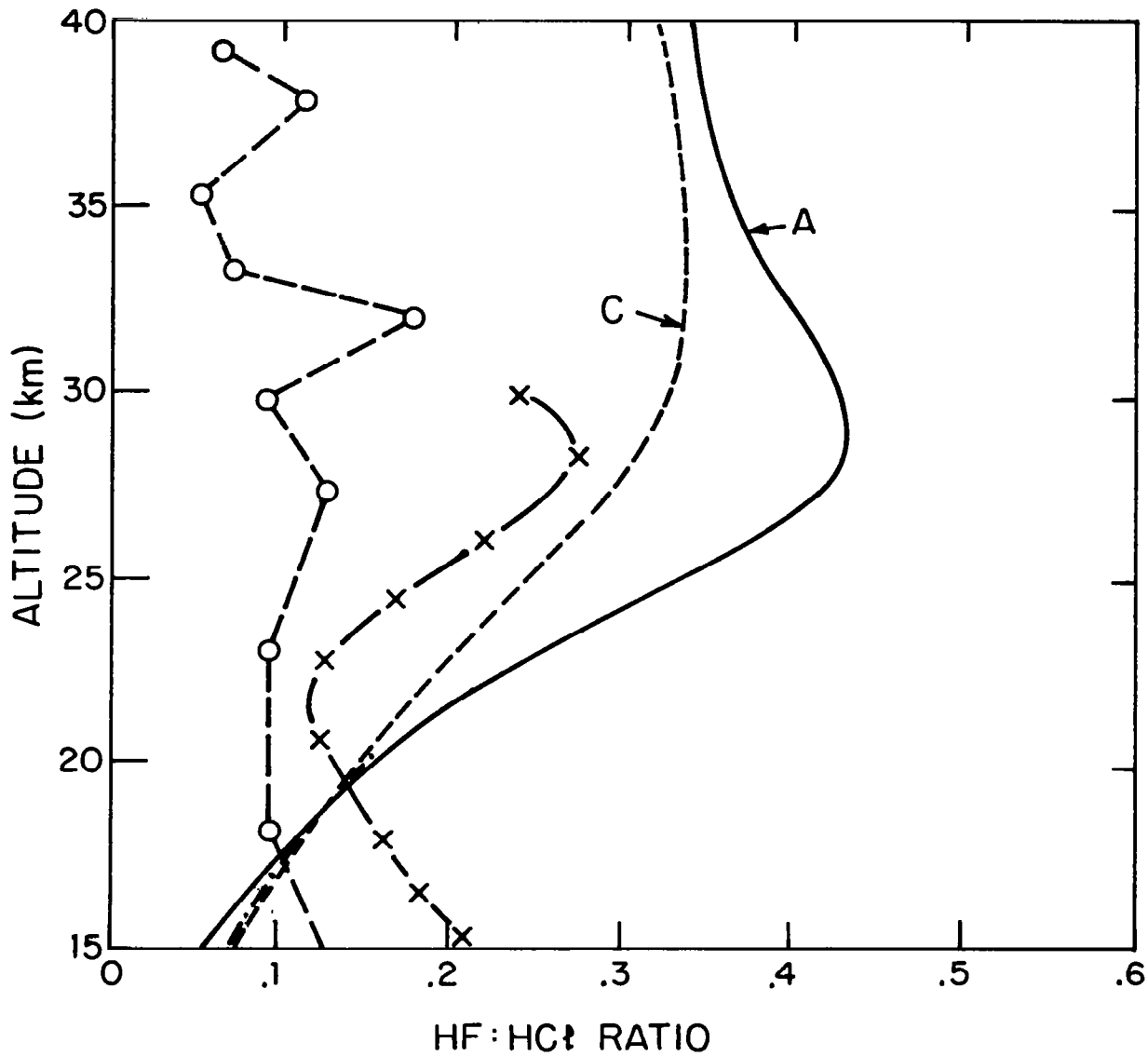


Figure 2-4

Calculated HF:HCl ratios corresponding to 30°N, equinox condition. The observations are:

- x-x Buijs et al. (1977)
- o-o Farmer and Raper (1977)

TABLE 2-2

Sensitivity of Column Ozone Perturbation  
to Supersonic Aircraft Cruise OperationNumber Correspond to  $\Delta O_3$  in percent

	15 km injection	20 km injection
Model A	+ 1.7	+ 4.0
Model B	+ .32	- 3.9
Model C	+ .25	- 6.0

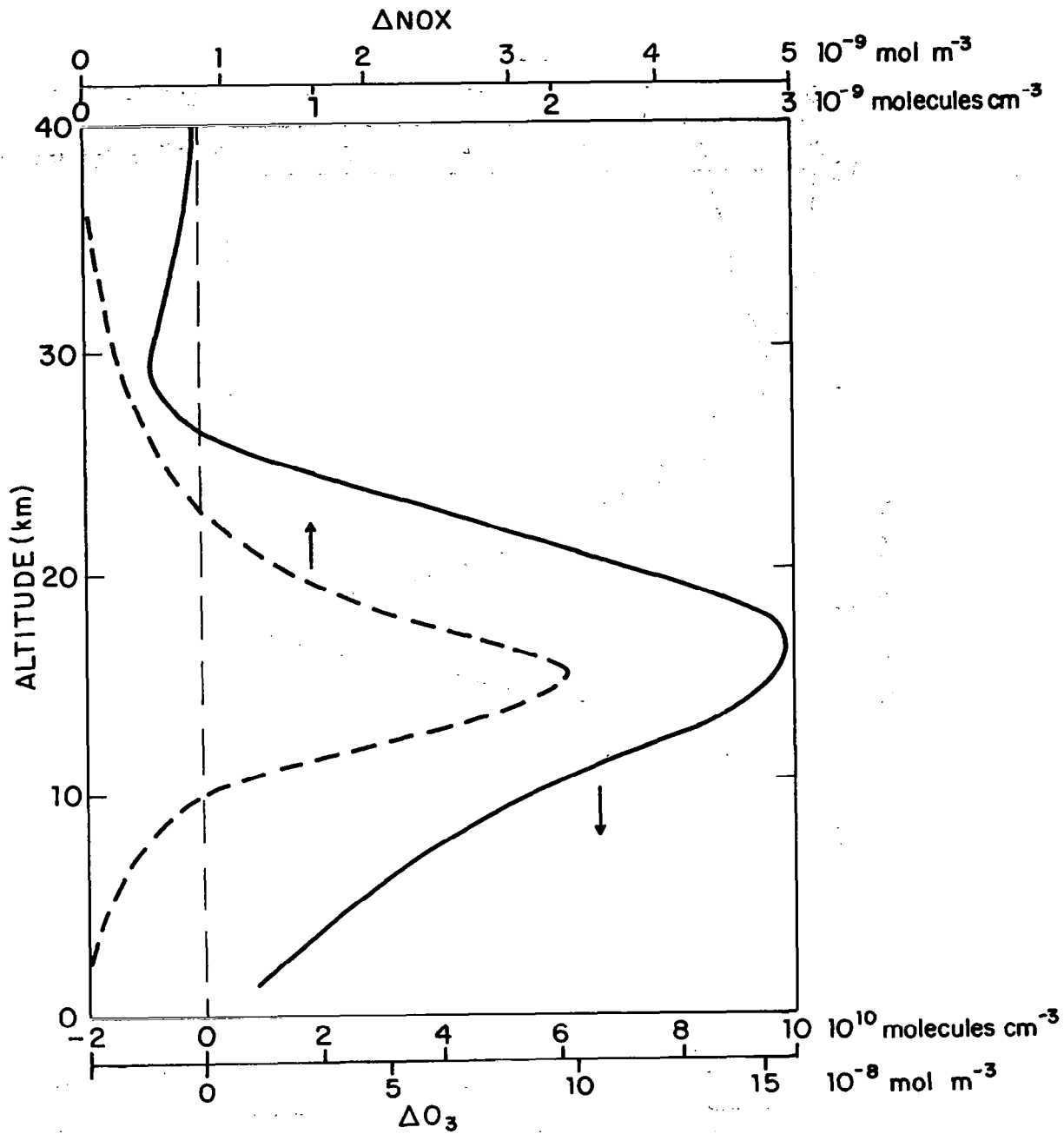


Figure 2-5a

Calculated changes in  $\text{O}_3$  and  $\text{NO}_x$  profiles for model A due to an injection of  $1.4 \times 10^8$  molecules (NO)  $\text{cm}^{-2} \text{ s}^{-1}$  at 15-16 km.

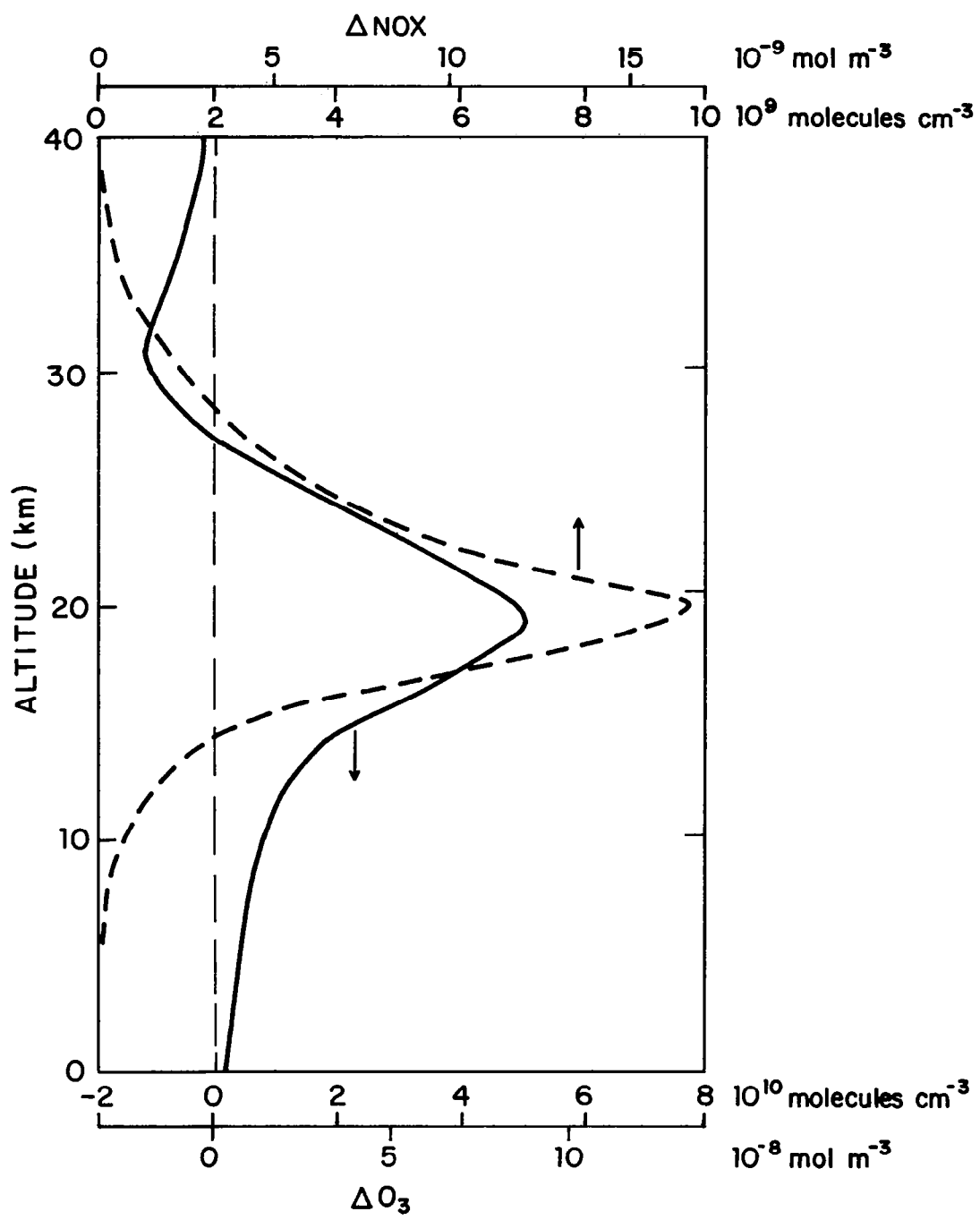


Figure 2-5b  
 Same as Figure 2-5a but with injection at 20-21 km.

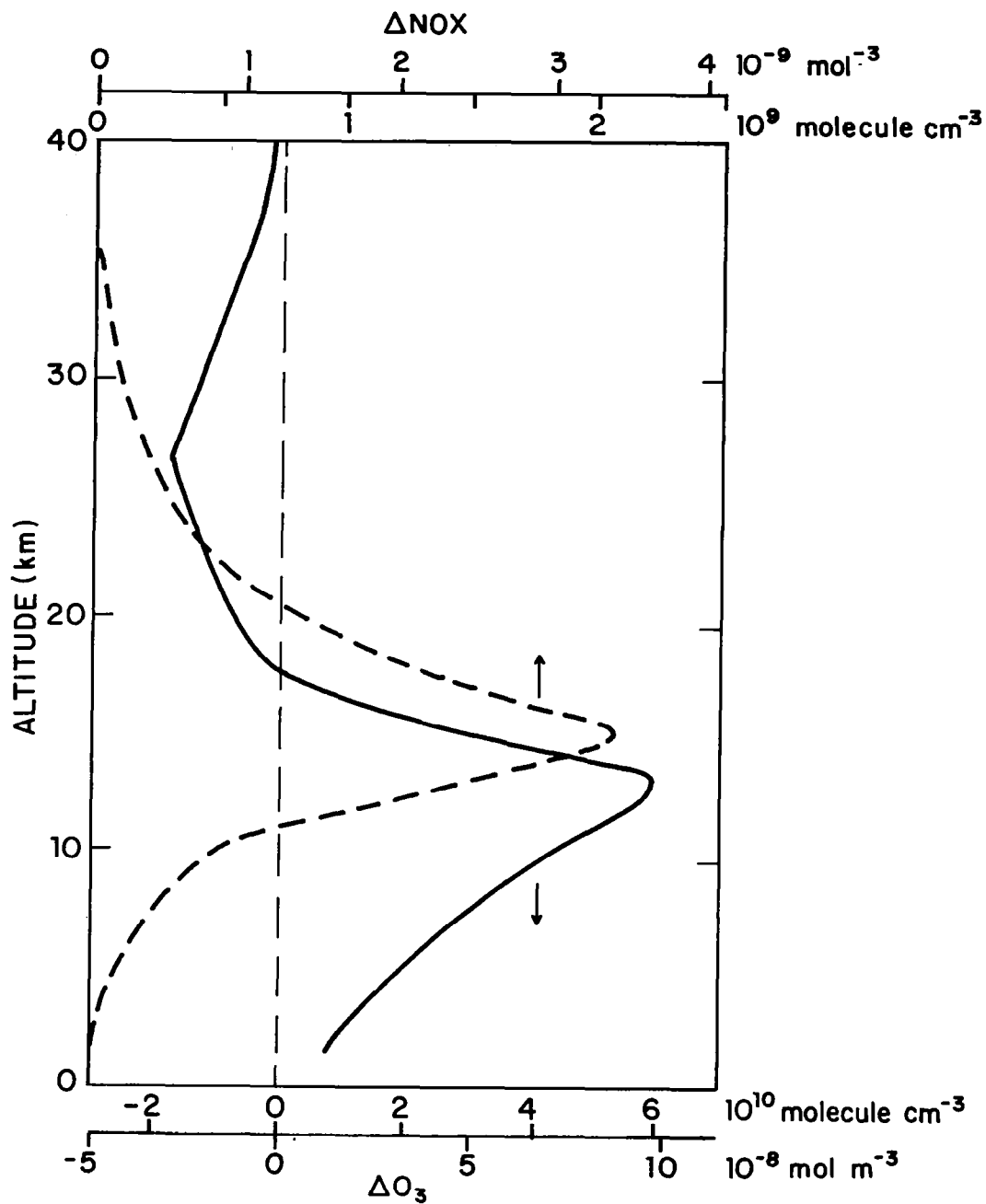


Figure 2-6a

Calculated changes in  $O_3$  and  $NO_x$  profiles for model C due to an injection of  $1.4 \times 10^8$  molecules (NO)  $\text{cm}^{-2} \text{ s}^{-1}$  at 15-16 km.

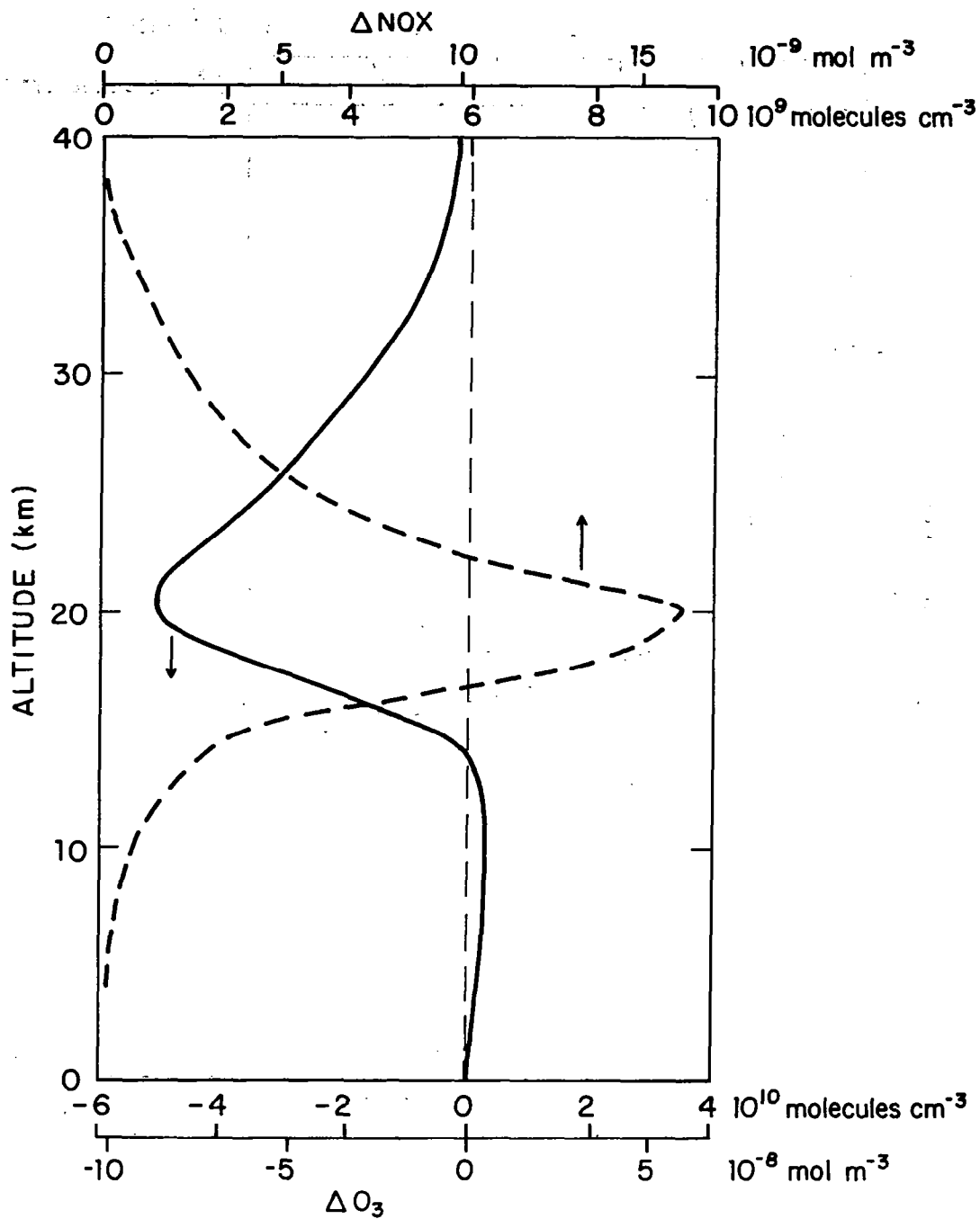


Figure 2-6b

Same as Figure 2-6a but with injection at 20-21 km.

from model B are similar to but somewhat smaller than those of model C. We may note that the range of calculated ozone perturbations span from +4 percent (model A) to -6 percent (model C) for the high altitude injection case. The range is considerably smaller in the low altitude injection case.

It seems clear that sensitivity of column ozone perturbations to  $\text{NO}_x$  injection depends not only on the cruise altitudes but also on the subtle differences in  $\text{HO}_x$  chemistry as illustrated by models A, B and C. While model A uses the best estimates of rate constants for the  $\text{HO}_x$  reactions, it fails to account for several observations as discussed earlier. On the other hand, model C seems to give better agreement with observations (see Figures 2-2, 2-3, 2-4), although several of the rate constants for reactions involving  $\text{HO}_2\text{NO}_2$  need future laboratory studies. Until better kinetic data are available, it is difficult to rule out any of the models discussed here.

The results presented above are based on Wofsy's (1976) eddy diffusion profile. Since ozone below 30 km is controlled mainly by dynamical transport, it is useful to find out how sensitive are model results to the choice of diffusion coefficients. Table 2-3 summarizes the results of models A and C which are calculated based on Chang's (1976)  $K_z$  profile. The results seem to be not much different from those calculated by using Wofsy's (1976)  $K_z$  profile.

It should be recognized that our analysis on the sensitivity of column ozone perturbation to eddy diffusion profile is restricted to a one-dimensional model. A more realistic description of the ozone problem clearly requires a two-dimensional model, since the distribution of ozone as well as aircraft injection are essentially two-dimensional in nature. Thus the one-dimensional sensitivity study of  $K_z$  profiles may be quite artificial, in the sense that the sensitivity of ozone perturbation to transport could be

TABLE 2-3

Sensitivity of Column Ozone Perturbations  
to Eddy Diffusion CoefficientNumber Corresponds to  $\Delta O_3$  (%) using Chang's (1976)  $K_z$ 

	15 km injection	20 km injection
Model A	+ 1.3	+ 1.5
Model B	~ 0.0	- 5.5

quite different in a 2-D model in which both horizontal and vertical transports are considered.

#### 2.4 Concluding Remarks

We have performed a series of model calculations to study the sensitivity of column ozone perturbations to the injection of  $\text{NO}_x$  associated with the operation of supersonic aircraft. Because of the coupling nature of hydrogen, nitrogen and chlorine chemistry, addition of  $\text{NO}_x$  could either increase or decrease local stratospheric  $\text{O}_3$ . A model with high background OH concentrations (e.g., model A) tends to predict an increase in column ozone for low and high altitude  $\text{NO}_x$  injections. On the other hand, a model with lower stratospheric OH (e.g., models B and C) tends to predict a small increase ( $\sim 1\%$ ) in column ozone for the low altitude injection case but a fairly significant reduction in column ozone for the high altitude injection case. More reliable kinetic data are clearly needed to narrow the uncertainties discussed here. For instance, the rate constant for the reaction of OH with  $\text{HO}_2\text{NO}_2$  needs to be measured on a high priority basis. Accurate determination of this rate constant could either rule out or substantiate model C.

Changes in local ozone and  $\text{NO}_x$  concentrations in the stratosphere may also affect the radiation budget. Recent calculations by Wang and Sze (1980) indicated that a doubling in  $\text{NO}_x$  may perturb the stratospheric temperatures and surface temperatures by as much as +1 K and +.15 K respectively, mainly through redistribution of stratospheric ozone (Wang and Sze, 1980). While changes in stratospheric temperature by 1 K are unlikely to be important in stratospheric chemistry, changes in surface temperature by .15 K are considered to be quite significant when compared with surface temperature changes caused by other atmospheric trace gases (Wang et al., 1976).

### 3. TWO-DIMENSIONAL ZONAL-MEAN MODELING

#### 3.1 Background

One of the tasks in atmospheric modeling is to attempt to simulate the behavior of a trace gas in the atmosphere. The local concentration of a trace gas is governed by the three-dimensional continuity equation

$$\left(\frac{\partial}{\partial t} + \underline{v} \cdot \nabla\right) f = Q/\rho \quad (3.1-1)$$

where  $f(t, \underline{x})$  is the mixing ratio,  $\underline{v}(t, \underline{x})$  the velocity wind fields describing the general circulation,  $\rho(t, \underline{x})$  the air number density and  $Q(t, \underline{x})$  is the local net production or loss (by chemical and/or physical transformation) of the trace gas. Equation (3.1-1) gives the time rate of change of  $f$  in the Eulerian description of fluid motion. The quantities  $f$ ,  $\underline{v}$ ,  $\rho$  and  $Q$  are to be considered as Eulerian field quantities as functions of time and spatial location with coordinates  $\underline{x}$ .

In order to solve equation (3.1-1) for the specie concentration, one must be able to provide values of  $\underline{v}$  and temperature  $T$  ( $T$  is necessary for calculation of reaction rates) as functions of space and time either by parameterization or by solving the system of dynamic equations. The atmospheric circulation is governed by the coupled system of dynamic and thermodynamic equations (cf. Lorentz, 1967) momentum equation

$$\frac{d\underline{v}}{dt} = -2\underline{\Omega} \times \underline{v} - \frac{1}{\rho M} \nabla p - \nabla \phi \quad (3.1-2)$$

thermodynamic equation

$$\frac{d\theta}{dt} = J \quad (3.1-3)$$

continuity equation

$$\frac{d\rho}{dt} = -\rho \nabla \cdot \underline{y} \quad (3.1-4)$$

equation of state: ideal gas law

$$p = \rho RT \quad (3.1-5)$$

where  $\frac{d}{dt} \equiv \frac{\partial}{\partial t} + \underline{y} \cdot \nabla$  is the total time derivative.

The above are to be considered as equations for the Eulerian field variables  $\underline{y}$ ,  $\rho$ ,  $p$  and  $\theta$ . The newly introduced symbols have the following meaning:

- $\underline{\Omega}$  = angular velocity of Earth
- $M$  = average mass of an air molecule
- $p$  = pressure
- $\Phi$  = the geopotential  $gz$  where  $g$  is acceleration due to gravity,  $z$  is geometrical altitude
- $\theta$  = potential temperature related to temperature  $T$  by  $\theta = T \left(\frac{p_0}{p}\right)^K$  with  $K = R/C_p$ ;  $R$  the gas constant and  $C_p$  the specific heat at constant pressure
- $J$  = the diabatic influence with  $C_p J \frac{T}{\theta}$  the heating rate per unit mass
- $R$  = the gas constant
- $T$  = temperature

Note that we have left out frictional forces in the momentum equation (3.1-2) under the assumption that they are unimportant for large scale motion.

The system of equations (3.1-2) to (3.1-5) is coupled to the specie equation through the  $J$  term which depends on distribution of gases such as  $O_3$ ,  $CO_2$ ,  $N_2O$  and  $CH_4$  in the atmosphere. Thus, in principle, equations (3.1-1) through

(3.1-5) must be solved simultaneously as a system.

In practice, the system of equations presents a formidable numerical problem and put enormous demand on both computer core memory and computation time. This is particularly true if one is interested in a realistic chemical scheme in order to simulate the distribution of the various species in the atmosphere. Besides, the set of exact equations also simulates phenomena of little interest for large scale motions. The following physical assumptions are usually adopted:

- A) Replacement of the vertical momentum equation by the hydrostatic equilibrium condition, i.e., the pressure gradient force is balanced by geopotential term)

$$\frac{\partial p}{\partial z} = -M \rho g \quad (3.1-6)$$

It is observed that motions due to deviation away from hydrostatic equilibrium are restricted to oscillations about the equilibrium state with time scales of order hour. The adoption of equation (3.1-6) effectively filters out vertically travelling sound waves.

- B) Discard terms containing the vertical velocities in the remaining two components of the momentum equation. This approximation appears to be justified because of the fact that the vertical component of the velocity is about two orders of magnitude smaller than the horizontal components.
- C) Replace  $r$  in the resulting equation by  $a$  where  $r$  is the distance from the Earth's center;  $a$  is the radius of the Earth.

The above assumptions lead to a system of equations usually referred to as the primitive equations. Next, it

would be desirable to write the momentum equation in scalar form. For this purpose, it is convenient to introduce a coordinate system where the pressure  $p$  is used as the vertical coordinates in conjunction with  $\lambda$  the longitude and  $\phi$  the latitude. In this coordinate system, the components of the velocity vectors are

$$u = a \cos\phi \frac{d\lambda}{dt}$$

$$v = a \frac{d\phi}{dt}$$

$$w = \frac{dp}{dt}$$

The continuity equation takes the form

$$\frac{1}{a \cos\phi} \frac{\partial u}{\partial \lambda} + \frac{1}{a \cos\phi} \frac{\partial}{\partial \phi} (v \cos\phi) + \frac{\partial w}{\partial p} = 0 \quad (3.1-7)$$

This is sometimes written in the form

$$\nabla \cdot \underline{v} = 0 \quad (3.1-8)$$

However, equation (3.1-8) holds only in pressure coordinates. Since equation (3.1-7) is derived using only the hydrostatic equation, it is more general than the incompressible fluid assumption. Finally, from equation (3.1-7), one can derive (cf. Lorentz, 1967)

$$\frac{ds}{dt} = \frac{\partial s}{\partial t} + \frac{1}{a \cos\phi} \frac{\partial}{\partial \lambda} (us) + \frac{1}{a \cos\phi} \frac{\partial}{\partial \phi} (v \cos\phi s) + \frac{\partial}{\partial p} (ws) \quad (3.1-9)$$

for any scalar  $s$ .

In this coordinate system, the primitive equations are (cf. Lorentz, 1967; Holton, 1975)

$$\frac{\partial f}{\partial t} + \frac{1}{a \cos \phi} \frac{\partial}{\partial \lambda} (fu) + \frac{1}{a \cos \phi} \frac{\partial}{\partial \phi} (fv \cos \phi) + \frac{\partial}{\partial p} (fw) = \frac{Q}{\rho} \quad (3.1-10)$$

$$\begin{aligned} \frac{\partial u}{\partial t} + \frac{1}{a \cos \phi} \frac{\partial}{\partial \lambda} (u^2) + \frac{1}{a \cos \phi} \frac{\partial}{\partial \phi} (uv \cos \phi) + \frac{\partial}{\partial p} (uw) \\ - \frac{uv \tan \phi}{a} - 2\Omega v \sin \phi - \frac{g}{a \cos \phi} \frac{\partial z}{\partial \lambda} = 0 \end{aligned} \quad (3.1-11)$$

$$\begin{aligned} \frac{\partial v}{\partial t} + \frac{1}{a \cos \phi} \frac{\partial}{\partial \lambda} (vu) + \frac{1}{a \cos \phi} \frac{\partial}{\partial \phi} (v^2 \cos \phi) + \frac{\partial}{\partial p} (vw) \\ + \frac{u^2 \tan \phi}{a} + 2\Omega u \sin \phi - \frac{g}{a} \frac{\partial z}{\partial \phi} = 0 \end{aligned} \quad (3.1-12)$$

$$\frac{\partial \theta}{\partial t} + \frac{1}{a \cos \phi} \frac{\partial}{\partial \lambda} (\theta u) + \frac{1}{a \cos \phi} \frac{\partial}{\partial \phi} (\theta v \cos \phi) + \frac{\partial}{\partial p} (\theta w) = J \quad (3.1-13)$$

$$\frac{1}{a \cos \phi} \frac{\partial u}{\partial \lambda} + \frac{1}{a \cos \phi} \frac{\partial}{\partial \phi} (v \cos \phi) + \frac{\partial w}{\partial p} = 0 \quad (3.1-14)$$

$$p = \rho R T \quad (3.1-15)$$

$$g \frac{\partial z}{\partial p} = - \frac{1}{\rho M} \quad (3.1-16)$$

In the above equations, the terms  $\frac{uv \tan \phi}{a}$  and  $\frac{u^2 \tan \phi}{a}$  are curvature terms arising from the non-Euclidean nature of the coordinate frames. The geopotential term  $\frac{1}{a} \frac{\partial \Phi}{\partial \phi}$  and  $\frac{1}{a \cos \phi} \frac{\partial \Phi}{\partial \lambda}$  has been written out explicitly with  $\Phi = gz$ .

In this arrangement, equations (3.1-10) through (3.1-13) are prognostic equations for  $f$ ,  $u$ ,  $v$  and  $\theta$  respectively, while equations (3.1-14) and (3.1-15) can be

considered as diagnostic equations for  $w$  and  $\rho$ . Since  $p$  is being used as an independent variable, equation (3.1-16) serves the purpose of transforming between geometrical altitude and the pressure coordinate.

We will now discuss ways of reducing the system of primitive equations to 2 dimensions for numerical modeling.

Taking any of the dependent Eulerian variables in the primitive equations, e.g.,  $f$ , by averaging over one of the spatial coordinates, one obtains  $\bar{f}(t, \underline{y})$  where  $\underline{y}$  is the vector representing the two remaining coordinates.

The corresponding equations governing the averaged variables can be obtained by applying the averaging operation to the primitive equations. In atmospheric modeling studies, one is interested in averaging over the longitudinal coordinate to obtain  $\bar{f}$  as a function of time, latitude and altitude, which can be viewed as the zonal-mean concentration. However, the exact physical interpretation of  $\bar{f}$  must depend on the averaging process involved.

In all of the 2-D zonal-mean models currently in use (cf. Hidalgo and Crutzen, 1977; Louis et al., 1974; Whitten et al., 1977; Borucki et al., 1976; Vupputuri, 1973; Harwood and Pyle, 1975) the Eulerian-mean operation is used exclusively. In the context of the present discussion, the most important feature in a Eulerian-zonal-mean model is the treatment of tracer transport. In these models, the flux into or out of a volume element is comprised of two terms: the flux due to advection by the zonal-mean velocity and the contribution due to the so-called "eddy fluxes". Several studies (Sawyer, 1965; Mahlman, 1975; Matsuno, 1979; Plumb, 1979) have found the above feature in the Eulerian-mean model to be undesirable and further work (Andrew and McIntyre, 1978; Dunkerton, 1978; Matsuno and Nakamura, 1979; Matsuno, 1980; Mahlman et al., 1980) eventually led to the development of

the generalized Lagrangian-mean (GLM) theory. As demonstrated by Andrew and McIntyre (1978), the flux of a trace gas in the GLM formulation is given as an advection term by a GLM velocity. Further studies by Dunkerton (1978) showed that this GLM velocity could be approximated from consideration of atmospheric heat balance.

It is the purpose of this section to discuss the possibility of applying the GLM theory to numerical zonal-mean modeling of atmospheric trace gases. In the next section, we will begin with a review of the current Eulerian-mean models in order to put the problem into proper perspective.

### 3.2 Eulerian-Mean Model

In the Eulerian-mean model, the averaging process is performed over Eulerian field quantities by integrating over one of the coordinates while holding all other coordinates fixed. In the case of the atmospheric models, the integration over the longitude is done along constant latitude circles, altitudes and time. Thus, given  $g(t, \phi, p, \lambda)$ , (where  $t$  is time,  $\phi$  the latitude,  $p$  the pressure height coordinates and  $\lambda$  the longitude), one obtains

$$\bar{g}(t, \phi, p) = \frac{\int g(t, \phi, p, \lambda) d\lambda}{\int d\lambda} \quad (3.2-1)$$

It is convenient to define  $g'$ , the deviations from the mean, by

$$g'(t, \phi, p, \lambda) = \bar{g}(t, \phi, p) - g(t, \phi, p, \lambda) \quad (3.2-2)$$

It follows from equation (3.2.1) that

$$\overline{g'(t, \phi, p, \lambda)} = 0 \quad (3.2-3)$$

and

$$\overline{gh} = \overline{g\bar{h}} + \overline{g'h'} \quad (3.2-4)$$

When the Eulerian-mean operation is applied to equations (3.1-10) to (3.1-16), using the fact that the "—" operation commutes with the coordinate differential operators, we have

$$\frac{\partial \overline{f}}{\partial t} + \frac{1}{a \cos \phi} \frac{\partial}{\partial \phi} (\overline{f} \overline{v} \cos \phi) + \frac{\partial}{\partial p} (\overline{f} \overline{w}) = \left(\frac{\overline{Q}}{\rho}\right) - F_f \quad (3.2-5)$$

$$\frac{\partial \overline{u}}{\partial t} + \frac{1}{a \cos^2 \phi} \frac{\partial}{\partial \phi} (\overline{u} \overline{v} \cos^2 \phi) + \frac{\partial}{\partial p} (\overline{u} \overline{w}) - 2\Omega \overline{v} \cos \phi = -F_u \quad (3.2-6)$$

$$\begin{aligned} \frac{\partial \overline{v}}{\partial t} + \frac{1}{a \cos \phi} \frac{\partial}{\partial \phi} (\overline{v} \cos^2 \phi) + \frac{\partial}{\partial p} (\overline{v} \overline{w}) + \frac{u \tan \phi}{a} \\ + 2 \overline{u} \Omega \sin \phi - \frac{g}{a} \frac{\partial \overline{z}}{\partial \phi} = -F_v \end{aligned} \quad (3.2-7)$$

$$\frac{\partial \overline{\theta}}{\partial t} + \frac{1}{a \cos \phi} \frac{\partial}{\partial \phi} (\overline{\theta} \overline{v} \cos \phi) + \frac{\partial}{\partial p} (\overline{\theta} \overline{w}) = \overline{J} - F_\theta \quad (3.2-8)$$

$$\frac{1}{a \cos \phi} \frac{\partial}{\partial \phi} (\overline{v} \cos \phi) + \frac{\partial \overline{w}}{\partial p} = 0 \quad (3.2-9)$$

$$\frac{p}{\rho} = R\overline{T} \quad (3.2-10)$$

$$g \frac{\partial \overline{z}}{\partial p} = -\frac{1}{M\overline{\rho}} = -\frac{R\overline{T}}{M\overline{p}} \quad (3.2-11)$$

$$\text{where } F_f = \frac{1}{a \cos\phi} \frac{\partial}{\partial\phi} (\overline{f'v'} \cos\phi) + \frac{\partial}{\partial p} (\overline{f'w'})$$

$$F_u = \frac{1}{a \cos^2\phi} \frac{\partial}{\partial\phi} (\overline{v'u'} \cos^2\phi) + \frac{\partial}{\partial p} (\overline{u'w'})$$

$$F_v = \frac{1}{a \cos\phi} \frac{\partial}{\partial\phi} (\overline{v'^2} \cos\phi) + \frac{\partial}{\partial p} (\overline{v'w'}) + \frac{\overline{u'^2} \tan\phi}{a}$$

$$F_\theta = \frac{1}{a \cos\phi} \frac{\partial}{\partial\phi} (\overline{\theta'v'} \cos\phi) + \frac{\partial}{\partial p} (\overline{\theta'w'})$$

are the eddy flux divergence terms. Note that in equation (3.2-6), we have incorporated the curvature term  $(\frac{uv \tan\phi}{a})$  into the  $\frac{\partial}{\partial\phi}$  term. It should be emphasized that the eddy flux terms are not constrained by the system of equations and must be specified or parameterized in terms of other variables.

In zonal-mean models, a further physical assumption is usually adopted. From scale analysis, it can be shown (cf. Holton, 1975) that equation (3.2-7) reduces to

$$2\Omega \sin\theta \bar{u} = \frac{g}{a} \frac{\partial \bar{z}}{\partial\phi} \quad (3.2-12)$$

to lowest order of a Rossby number expansion. This is the geostrophic assumption which provides a good approximation for midlatitude dynamics though some authors (Harwood and Pyle, 1975) argued that the approximation is reasonable up to about 5°. The geostrophic assumption filters out occurrence of gravity waves and other equatorial waves that cause the quasi-biennial oscillations in the stratosphere. Equation (3.2-12) is awkward to use as  $\bar{z}$  is not one of the dependent variables. One can differentiate the equation

with respect to  $p$  and use the hydrostatic equation to obtain the thermal wind relation

$$p \frac{\partial \bar{u}}{\partial p} = - \frac{\left(\frac{R}{M}\right) \left(\frac{p}{p_0}\right)^K}{2\Omega \sin\phi} \frac{1}{a} \frac{\partial \bar{\theta}}{\partial \phi} \quad (3.2-13)$$

to replace equation (3.2-7). This eliminates  $F_v$  as an extra variable. However, one still needs ways of determining  $F_f$ ,  $F_u$  and  $F_\theta$  to close the system of equations.

All existing zonal-mean models use the method of parameterization via eddy diffusion tensor originally proposed by Reed and German (1965). Using mixing length type arguments, Reed and German argued that for a quantity  $x$  which is conserved along its flow, the eddy fluxes are related to the gradient zonal-mean quantity  $\bar{x}$  via

$$\begin{pmatrix} \overline{v'x'} \\ \overline{w'x'} \end{pmatrix} = \begin{pmatrix} K_{\phi\phi} & K_{\phi p} \\ K_{p\phi} & K_{pp} \end{pmatrix} \begin{pmatrix} \frac{1}{a \cos\phi} \frac{\partial \bar{x}}{\partial \phi} \\ \frac{\partial \bar{x}}{\partial p} \end{pmatrix} \quad (3.2-14)$$

where  $K$  is a symmetric tensor. Following the procedure similar to the one suggested by Reed and German (1965), Luther (1973) analyzed the heat transfer, temperature and wind variance data of Oort and Rasmussen (1971) and derived a set of  $K$  tensors as a function of time and space. It should be noted that the data only covered part of the northern hemisphere. Extrapolations were used to deduce the  $K$ 's at places where there is no data based on results of Newell et al., (1966) and Wofsy and McElroy (1973). Furthermore, the  $K$ 's for the southern hemisphere are obtained by reflecting the northern hemispheric values in the appropriate seasons. The set of  $K$ 's from Luther (1973) is by far the most complete with a set of values for each

month covering the meridional plane from the surface to 60 km. In almost all of the zonal models, this set of  $K$ 's provides the basis for eddy transport. We would like to emphasize here the limitation of this approach:

- (i) The original argument of Reed and German (1965) was presented to treat turbulence diffusive type motions. Thus, the approach may not be appropriate if there is organized wave-type motion in the zonal direction. This has been demonstrated in studies of 3-D circulation by Mahlman (1975), Matsuno and Nakamura (1979), Plumb (1979) and Matsuno (1980) in the case of planetary wave motions. To date, no satisfactory justification for applying the eddy diffusion theory to stratospheric motion has been presented.
- (ii) The argument only applies to conservative flow. Thus, strictly speaking, it can only be applied to inert tracers or to potential temperatures in adiabatic flow. However, in zonal-mean models, it is applied to chemical species with finite chemical lifetimes and to the potential temperature where the condition of adiabatic flow is not strictly satisfied.

The treatment of  $F_u$  presents special problems and will be discussed later.

We will now examine some of the zonal-mean models and discuss the various approaches adopted. The models can be separated into two groups depending on the number of the primitive equations it attempts to solve. In the first group of models, only equation (3.2-5) is solved as a prognostic equation. The variables necessary as input for the equation, i.e.,  $\bar{v}$ ,  $\bar{w}$  and  $\bar{T}$  (necessary for calculation of

reaction rate constants) are parameterized. In addition, a chemical scheme has to be set up to calculate the production and loss term  $Q$ . The models of Hidalgo and Crutzen (1977), Louis et al., (1974), Widhopf (1975), the NASA Ames Model (Whitten et al., 1977; Borucki et al., 1976) and the Meteorology Office Model (Hinds, 1979) fall into this category.

Strictly speaking, the  $\bar{v}$ ,  $\bar{w}$  and  $\bar{T}$  specified must satisfy equations (3.2-7) through (3.2-9). The circulations used in most of these zonal models are based on the work of Louis et al., (1974) who computed the circulation patterns for each season by solving the continuity equation (3.2-9) and energy equation (3.2-8) using the compiled observations of local meridional temperature distribution and heat transfer rates. However, interpolations and adjustments are usually made subsequently by the individual authors. In those cases,  $\bar{w}$  is obtained by solving equation (3.2-9) once  $\bar{v}$  has been chosen in order to assure mass conservation. In models that use pressure coordinates, the hydrostatic equilibrium assumption is implicit in equation (3.2-9). In some models, e.g., the NASA Ames Model, geometrical altitude is used instead. In this particular model, the zonal-mean continuity equation takes the form

$$\frac{\partial \bar{\rho}}{\partial t} + \frac{1}{a \cos \theta} \frac{\partial}{\partial \phi} (\bar{\rho} \bar{v} \cos \theta) + \frac{\partial}{\partial z} (\bar{\rho} \bar{z}) = -F_{\rho} \quad (3.2-15)$$

where  $F_{\rho} = \frac{1}{a \cos \phi} \frac{\partial}{\partial \phi} (\overline{\rho'v'}) \cos \theta + \frac{\partial}{\partial t} (\overline{\rho'z'})$  and  $\dot{z} = \frac{dz}{dt}$  is the vertical velocity. Equation (3.2-15) is then reduced to

$$\frac{1}{a \cos \phi} \frac{\partial}{\partial \phi} (\bar{\rho} \bar{v} \cos \theta) + \frac{\partial}{\partial z} (\bar{\rho} \bar{z}) = 0$$

by assuming that  $\frac{\partial \bar{\rho}}{\partial t} = 0$ , and  $F_{\rho} = 0$ . It is not clear how these additional assumptions are to be justified.

We will next discuss how to obtain  $\overline{Q/\rho}$  once a photochemical scheme has been set up. The term  $Q/\rho$  consists of sums of terms each of which take one of the following forms

$$J_i f_i; \rho k_{ij}(T) f_i f_j; \rho^2 k_{ijk}(T) f_i f_j f_k$$

for photolytic processes and two-body and three-body reactions respectively. Note that the temperature dependence of the reaction rates  $k_{ij}$  and  $k_{ijk}$  are explicitly displayed. The longitudinal behavior of  $J_i$  and  $f_i$  arise from the diurnal effect since each longitude is at a different local time at any instant in time. A similar problem arises in the 1-D model and is usually taken care of by putting diurnal averaged photolysis rates in the chemical scheme so that the resulting species concentrations represent diurnally averaged values. In addition, the longitudinal distribution of the gas may be affected by wave motion in the zonal direction. No attempts are made to treat such effects. In the zonal averaging process, the term  $\overline{Q/\rho}$  is obtained by taking the sum of the corresponding products of the zonal-measured quantities. Eddy flux terms are ignored.

Finally, it should be noted that because of the uncertainties in the input data, most authors adjust the wind fields and eddy diffusion tensors to obtain agreement between calculated results and observations as a way to calibrate their model. This must be taken into account in model validation studies. Also, as the input data are based on observations of the present atmosphere, such models are not suitable for large scale perturbation studies since there is no way to predict future circulation patterns.

The next group of zonal models actually solve the system of equations simultaneously. The approach will be outlined below. For a more detailed treatment, the reader

is referred to the work of Harwood and Pyle (1975) and Vupputuri (1973).

Equations (3.2-6) and (3.2-8) can be written as

$$\frac{\partial \bar{u}}{\partial t} = A \quad (3.2-16)$$

$$\frac{\partial \bar{\theta}}{\partial t} = B \quad (3.2-17)$$

where A and B do not contain any time derivatives. If one differentiates equation (3.2-16) by p and equation (3.2-17) by  $\phi$  and takes the appropriate linear combination of the resulting equation, by virtue of the thermal wind relations equation (3.2-13), one obtains

$$p \frac{\partial A}{\partial p} + \frac{\left(\frac{R}{M}\right) \left(\frac{p}{p_0}\right)^K}{2\Omega \sin\phi} \frac{1}{a} \frac{\partial B}{\partial \phi} = 0 \quad (3.2-18)$$

Note that there is no time derivative in equation (3.2-18). Equation (3.2-9) implies the existence of a function  $\psi$  where

$$\bar{v} = - \frac{1}{\cos\phi} \frac{\partial \psi}{\partial p} \quad (3.2-19)$$

$$\bar{w} = \frac{1}{a \cos\phi} \frac{\partial \psi}{\partial \phi}$$

Using equation (3.2-19) to eliminate  $\bar{v}$  and  $\bar{w}$  in equation (3.2-18), we obtain a second order partial linear differential equation for  $\psi$  where the coefficients are functions of  $\bar{u}$ ,  $\bar{\theta}$ ,  $\bar{J}$ ,  $F_u$ ,  $F_\theta$  and their spatial derivatives. The system of equations can now be solved as follows. Give  $\bar{f}$ ,  $\bar{\theta}$ ,  $\bar{u}$ ,  $\bar{v}$  and  $\bar{w}$  at one instance in time, one can compute  $\bar{Q}/\rho$ ,  $\bar{J}$ ,  $F_f$ ,  $F_\theta$  and  $F_u$  and solve the prognostic equations (3.2-5), (3.2-6) and (3.2-8) for  $\bar{f}$ ,  $\bar{u}$  and  $\bar{\theta}$  at a later time. With

these new values, one solves equation (3.2-18) for  $\psi$  with appropriate boundary conditions and generate new  $\bar{v}$  and  $\bar{w}$  via equation (3.2-19). The terms  $\overline{Q/\rho}$  are to be calculated as discussed before. The treatment of  $\bar{J}$  is similar in that the term is obtained by using zonal-mean values in the expression while ignoring eddy flux terms.  $F_f$  and  $F_\theta$  are to be parameterized by eddy diffusion tensors. The treatment of  $F_u$  is more difficult because the u momentum is definitely not conserved in the flow. Attempts to parameterize  $F_u$  in terms of potential vorticity and potential temperature has little success (Green, 1970; Wiin-Neilsen and Sela, 1971). Vupputuri (1979) employed an ad hoc parameterization while Harwood and Pyle (1975) deduced the momentum fluxes from Nimbus V SCR data. Until a more satisfactory theoretical approach is available, the satellite data approach seems to be preferable at this stage.

Thus, even in the case when one actually computes the circulation and temperature, one still has to depend on observations to parameterize the eddy flux terms. It is also noted in the calculation of Harwood and Pyle (1977) that the fluxes due to the mean circulation are often in opposite direction to eddy fluxes. Thus, the net transport is the difference between the two terms. This suggests the act of splitting the transport term into the advection and eddy fluxes components may not be appropriate. It is the desire to get away from eddy flux formulation that led to the development of the generalized Lagrangian-mean zonal models.

### 3.3 Generalized Lagrangian-Mean (GLM) Zonal Models

An alternative to the Eulerian approach of fluid motion is the classical Lagrangian approach. In such an approach, one is interested in how a quantity changes as one follows the motion of the fluid. More specifically, the property

g is given by the function  $g(t, \underline{s})$  where  $\underline{s}(t, \underline{x}^0)$  is the position vector of a fluid particle labelled by  $\underline{x}^0$ . This method has been used to study the general circulation in three dimensions in several studies (cf. Riehl and Fultz, 1957; Krishnamurti, 1961; Danielson, 1968; Mahlman, 1969, 1973). Further developments in an attempt to apply the Lagrangian type dynamics treatment to zonal-mean quantities led to the development of the Generalized Lagrangian-Mean (GLM) theory (Andrew and McIntyre, 1978; Kida, 1977; Dunkerton, 1978; Matsuno and Nakamura, 1979; Matsuno, 1980).

It should be noted that the GLM zonal approach is actually a combination of Eulerian-Lagrangian descriptions of fluid motion. One actually starts with the Eulerian equation (3.1.1) and applies the GLM operator obtaining

$$\frac{\partial \bar{f}^L}{\partial t} = - \frac{\bar{v}^L}{a} \frac{\partial \bar{f}^L}{\partial \phi} - \bar{w}^L \frac{\partial \bar{f}^L}{\partial p} + \overline{Q/\rho}^L \quad (3.3-1)$$

where  $\bar{f}^L(t, \phi, p)$  is the Eulerian field resulting from the application of the GLM operator to  $f(t, \phi, p, \lambda)$ ;  $\bar{v}^L$  and  $\bar{w}^L$  are the components of the GLM velocity fields obtained by averaging the Eulerian velocity field. Before discussing the definition of the GLM operator, it should be noted that the tracer transport in equation (3.3-1) is given by advection only, thus, eliminating any possibility of cancellation between advection and eddy terms.

The GLM operation can be defined by the following set of equations (Andrew and McIntyre, 1978). Given an Eulerian field  $g(t, \underline{x})$  we defined  $\bar{g}^L$  by

$$\bar{g}^L = \overline{g(t, \underline{x} + \underline{\xi}(t, \underline{x}))} \quad (3.3-2a)$$

where  $\underline{\xi}$  satisfies

$$\left(\frac{\partial}{\partial t} + \bar{\mathbf{v}}^L \cdot \nabla\right) (\underline{\mathbf{x}} + \underline{\xi}(t, \underline{\mathbf{x}})) = \underline{\mathbf{v}}(t, \underline{\mathbf{x}} + \underline{\xi})$$

or

$$\left(\frac{\partial}{\partial t} + \bar{\mathbf{v}}^L \cdot \nabla\right) \underline{\xi}(t, \underline{\mathbf{x}}) = \underline{\mathbf{v}}(t, \underline{\mathbf{x}} + \underline{\xi}) - \bar{\mathbf{v}}^L \quad (3.3-2b)$$

and

$$\overline{\underline{\xi}(t, \underline{\mathbf{x}})} = 0 \quad (3.3-2c)$$

In the above equations, "—" denotes Eulerian averaging along the longitudinal coordinates,  $\underline{\xi}(t, \underline{\mathbf{x}})$  is the disturbance induced displacement field,  $\underline{\mathbf{v}}(t, \underline{\mathbf{x}})$  is the fluid velocity field (an Eulerian field quantity) and  $\bar{\mathbf{v}}^L$  is the GLM velocity field obtained by applying  ${}^{-L}$  to  $\bar{\mathbf{v}}^L$  to  $\underline{\mathbf{v}}$ , i.e.,  $\bar{\mathbf{v}}^L = \overline{\underline{\mathbf{v}}(t, \underline{\mathbf{x}} + \underline{\xi}(t, \underline{\mathbf{x}}))}$ . Note that from equation (3.3-2a), instead of averaging over constant latitudes and altitude, the averaging is done following the fluid particles to their displaced position. This gives a Lagrangian flavor to the approach though  $\underline{\xi}(t, \underline{\mathbf{x}})$  does not necessarily have to represent actual fluid motion. In the formulation,  $\bar{\mathbf{v}}^L$  and  $\underline{\xi}$  are implicitly defined by equations (3.3-2b) and (3.3-2c) and can be obtained by solving the equations given  $\underline{\mathbf{v}}(t, \underline{\mathbf{x}})$  together with appropriate initial conditions. And as long as equations (3.3-2b) and (3.3-2c) are satisfied, equation (3.3-1) can be obtained by applying  ${}^{-L}$  to equation (3.3-1).

To date, most of the work in GLM analysis has been done from a three-dimensional point of view, i.e., the motion (usually wave type) in 3 dimensions is specified, the properties of wave transport are then studied in the context of GLM theory (cf. Matsuno and Nakamura, 1979; Matsuno, 1980, Mahlman et al., 1980).

In a zonal model, one would like to integrate equation (3.3-1) in time to obtain  $\bar{f}^L$  as a function of time. Thus, it is necessary to obtain  $\bar{v}^L$  and  $\bar{w}^L$  without a priori knowing the 3-dimensional general circulation. Secondly, one has to be more specific in the definition of  $\xi$  so that a physical interpretation can be given to the GLM operation and that  $\bar{f}^L$  can be compared to observations. We will discuss these problems in what follows.

(a) Interpretation of  $\xi$  and  $\bar{v}^L$

In the formulation of Andrew and McIntyre (1978), the definition of  $\xi$  is purposely left vague in order that the formalism can be applied to any averaging operations. The quantity  $\xi(t, \underline{x})$  is loosely referred to as the disturbance induced displacement vector. One can imagine the situation in which a parcel of air molecules is initially at rest on a latitudinal circle at constant altitude  $[\underline{x}]$ . (Note that  $[\underline{x}]$  stands for a latitude circle at constant altitude). At  $t = t_0$ , the molecules start executing motions given by  $\xi(t, \underline{x})$ , i.e., the coordinate of the particle initially located at  $\underline{x}$  is given at time  $t$  by  $\underline{x} + \xi(t, \underline{x})$ . Then according to equation (3.3-2a), instead of averaging over the particles that happen to be located at  $\underline{x}$  at time  $t$ , the averaging is done following the fluid particles as they travel along the trajectory  $\xi(t, \underline{x})$ . If  $\xi(t, \underline{x})$  satisfies equations (3.3-2b) and (3.3-2c), then the averaging proceeding qualifies as GLM operation, and  $\bar{v}^L$  can be interpreted as the motion associated with the center of mass of the air parcel originally located at  $\underline{x}$ . This interpretation has been presented by Andrew and McIntyre (1978) using their mechanical analog and is essentially the same as interpretations presented by other authors (Dunkerton, 1978; Mahlman et al., 1980).

The above interpretation of  $\bar{v}^L$  is contingent upon the fact that  $\xi(t, \tilde{x})$  satisfies equations (3.3-2b) and (3.3-2c). In general, this will not hold for Lagrangian trajectory of the fluid. However, since  $\xi(t, \tilde{x})$  is defined by the current positions of the particles as well as  $\tilde{x}$ , one can redefine  $\xi$  as  $\xi(t, \tilde{x}_0)$  so that equations (3.3-2b) and (3.3-2c) are satisfied (Tung, private communication). The details of this manipulation will be presented in Appendix E.

Under the initialization process,  $\bar{f}^L$  can be interpreted as the average mixing ratio of the air molecules that would have been located at  $\tilde{x}_0$  in the absence of the disturbance induced displacement. Similarly,  $\overline{Q/\rho}^L$  is the average production rate of the same set of molecules and  $\bar{v}^L$  and  $\bar{w}^L$  are the components of the velocity associated with the center of mass of that air parcel.

Note that a parcel of air has a tendency to spread out because of diffusion. Thus, the magnitude of  $\xi(t, \tilde{x}_0)$  would get progressively larger. It will then become increasingly difficult to relate  $\bar{f}^L$  to actual observations as the individual molecules that enter into the averaging process are distributed over the entire atmosphere. The same applies to the computation of  $\overline{Q/\rho}^L$  in the sense that  $\overline{Q/\rho}^L$  at some particular latitude and height may differ significantly from the corresponding products of the  $\bar{f}^L$ 's at the same point.

#### (b) Determination of $\bar{v}^L$ and $\bar{w}^L$

In order to use equation (3.3-1) as a prognostic equation, one needs the values  $\bar{v}^L$  and  $\bar{w}^L$ . If the three-dimensional motion is known, one can conceivably solve equation (3.3-2b) and (3.3-2c) for  $\xi$  and  $\bar{v}^L$  with choice of initial conditions. However, if one is interested in a zonal model than can include feedback mechanisms between chemistry and dynamics, one would have to be able to obtain

$\bar{v}^L$  and  $\bar{w}^L$  without a priori knowledge of the motion.

One possible approach is to try to obtain  $\bar{v}^L$  and  $\bar{w}^L$  from the GLM momentum equation. Unfortunately, as demonstrated in Andrew and McIntyre (1978), the price paid for the simplification in equation (3.3-1) is that  ${}^L$  no longer commutes with the coordinate differential operators. For example, the GLM flow of an incompressible fluid satisfying  $\nabla \cdot \underline{v} = 0$  is not non-divergent, i.e.  $\nabla \cdot \bar{\underline{v}}^L \neq 0$ , in contrast to the case of Eulerian mean flow. Another result of the non-commutability of the operator  ${}^L$  and  $\nabla$  is that the GLM momentum equation contains terms involving  $\xi$ , i.e.

$$\bar{\nabla} p^L = \nabla \bar{p}^L + (\text{term involving } \xi \text{ and derivative of } \xi)$$

These terms are reminiscent of the eddy flux terms in the Eulerian mean formulation and require parameterization.

Dunkerton (1978) suggested an alternative approach to the problem from analysis of the thermodynamic equation. Using a linearized version of GLM theory for steady waves, Dunkerton showed that under certain conditions

$$\bar{w}^L = \frac{\bar{Q}}{\Gamma_d - \Gamma} \quad (3.3-3)$$

$$\frac{1}{a \cos \phi} \frac{\partial}{\partial \phi} (\bar{v}^L \cos \phi) + \frac{\partial \bar{w}^L}{\partial p} = 0 \quad (3.3-4)$$

where  $\bar{Q}$  is the Eulerian mean diabatic heating rate,  $\Gamma_d - \Gamma$  is the lapse rate. The 3-D equation for potential temperature can be written

$$\left( \frac{\partial}{\partial t} + \underline{v} \cdot \nabla \right) T = Q \quad (3.3-5)$$

where  $Q$  is the diabatic heating. Upon GLM averaging one obtains

$$\frac{\partial \bar{T}^L}{\partial t} + \frac{\bar{v}^L}{a} \frac{\partial \bar{T}^L}{\partial \phi} + \bar{w}^L \frac{\partial \bar{T}^L}{\partial p} = \bar{Q}^L \quad (3.3-6)$$

Equation (3.3-3) can be derived from equation (3.3-6) if the following assumptions are made (Dunkerton, 1978)

- (i)  $\frac{\partial \bar{T}^L}{\partial t}$  negligible
- (ii)  $\frac{\bar{v}^L}{a} \frac{\partial \bar{T}^L}{\partial \phi}$  negligible
- (iii)  $\bar{Q}^L \approx \bar{Q}$
- (iv)  $\bar{T}^L \approx \bar{T}$  so that  $\frac{\partial \bar{T}^L}{\partial p} \approx \frac{1}{\Gamma_d - \Gamma}$

Equation (3.3-4) is the continuity equation obtainable from the GLM equation by discarding terms of  $O(\xi^2)$ . Using the heating rate of Murgatroyd and Singleton (1961), Dunkerton solved equations (3.3-3) and (3.3-4) for  $\bar{v}^L$  and  $\bar{w}^L$  and obtained results that are capable of explaining the gross features of tracer transport.

Although the assumption used in deriving equations (3.3-3) and (3.3-4) may not be valid in the whole atmosphere, the result of Dunkerton is beautiful in its conceptual simplicity in relating the circulation to diabatic heat balance. However, the application of the results to zonal modeling may not be straight forward. The situation is particularly difficult in dealing with finite amplitude motions.

### 3.4 Concluding Remarks

In this section, we have presented a brief review of the generalized Lagrangian mean description of atmospheric circulation. Most of the studies done to date in GLM

theory have been concerned with applying the technique in analyzing the transport due to specific wave motions [in 3 dimension] in the atmosphere. In this section we have taken the view of trying to use equation (3.3-1) as the prognostic equation in zonal modeling.

The zonal mean tracer equation (3.3-1) is attractive in that the only transport of tracer is due to advection by the Lagrangian mean velocity only. From our studies, we identified several crucial areas that need to be investigated in order that the GLM tracer equation can be profitably applied to zonal modeling. The first of these has to do with the basic interpretation of equation (3.3-1). As demonstrated in Section (3.3) and Appendix E, the disturbance induced displacement vector can be related to the actual fluid motion. Then  $\bar{f}^L$  can be interpreted as the average mixing ratio of the air molecules in an air parcel originally located at  $[\overset{\circ}{x}]$  where  $[\overset{\circ}{x}]$  stands for the coordinates of the set of points on a latitude circle at constant altitude. Though the idea of keeping track of the identity of the molecules may be very useful in the analysis of mass transport, it may introduce complications in modeling of trace gases. As an air parcel is spread out thinner and thinner over an ever increasing region of the atmosphere, it becomes almost impossible to relate  $\bar{f}^L$  to the local observed concentrations. This suggests that one may want to relax the rigid relation between  $\xi$  and the trajectory introduced in Appendix E and employ different initializations during the time integration of equation (3.3-1) using each initialization for only short time intervals.

An ideal zonal model should be able to compute the circulation given the ambient concentrations of the trace gas and the state of the atmosphere. Thus, it would be nice if there is some way to solve for  $\bar{v}^L$  and  $\bar{w}^L$  as functions of  $\bar{f}^L$ s and temperature. Such an approach will require research into the reformulation of the momentum

equation. By defining some kind of generalized differential operators, it may be possible to cast the momentum equation in a form that has no explicit dependence in  $\xi$ .

The above areas involve long term developments. On the more immediate term, one can still explore the merits of the GLM model by using  $\bar{v}^L$  and  $\bar{w}^L$  derived from given three-dimensional motion fields. The initial analysis could be applied to studies of inert tracers, thereby avoiding the question about  $\overline{Q/\rho}^L$ . Numerical experiments dealing with inert tracer release can be done. Such experiments will be more meaningful if the results can be compared with results from similar experiments using Eulerian mean models. One can then compare the center of mass motion obtained from the Eulerian model to see if it bears any resemblance to  $\bar{v}^L$  and  $\bar{w}^L$ .

One could also concentrate on cases with small disturbances and make use of the results of Dunkerton (1978) to generate the wind fields. The heating rate of Murgatroyd and Singleton (1961) was used in the original analysis by Dunkerton (1978). We feel that a more careful treatment of the diabatic heating could be used to generate  $\bar{v}^L$  and  $\bar{w}^L$  so that they can be used in subsequent tracer studies. Again, the study of such General Lagrangian Mean transport can be carried out most profitably in conjunction with parallel Eulerian mean model studies. One can take the results of Eulerian mean cell models which contain calculated  $\bar{v}$ ,  $\bar{w}$ , and the temperature distribution. The temperature structure can be used to generate the Lagrangian velocity field  $\bar{v}^L$  and  $\bar{w}^L$  via Dunkerton's approach. At the same time, one can use the Eulerian model to perform tracer experiments and try to determine if there is any relationship between the center of mass motion of the tracer and the  $\bar{v}^L$  and  $\bar{w}^L$ .

## 4. REMOTE SENSING

### 4.1 Background

Spectroscopic measurements using remote sensing techniques can provide information on the altitude distribution of constituents in the upper atmosphere. Using a solar occultation approach, for example, inversion methods have been demonstrated to obtain ozone, aerosol, and nitrogen dioxide profiles from solar extinction data in the .38-1.0  $\mu\text{m}$  wavelength region (Chu and McCormick, 1979). Since occultation measurements are made at definite times of the day, i.e., twilight or dawn for solar occultation, it is clear that diurnal variation of species must be considered in the interpretation of results. Particularly rapid variation of photochemically active species (such as OH, HO<sub>2</sub>, ClO, NO, etc.) (see Logan et al. 1978) may introduce ambiguities in the treatment of species abundances determined along a particular line of sight since such experiments are essentially looking through different local times and altitudes (Herman, 1979). Conversely, inversion results may provide a stringent test for diurnal model calculations.

Additional constraints relate to the role of molecular multiple scattering on both transmitted radiances and dissociative fluxes required for photochemical modeling. As pointed out by Callis (1974), molecular scattering of solar radiation can significantly affect photolysis rates in the lower atmosphere ( $z < 40$  km). A number of studies (Callis et al. 1975; Luther and Gelinas, 1976; Luther et al. 1978; Anderson and Meier, 1979) have examined multiple scattering effects on photolysis rates and species concentrations employing the plane-parallel approximation of radiative transfer. Near dawn and dusk, however, the inherent curvature of the atmosphere becomes an important

consideration and realistic treatments of the effect of multiple scattering require radiative transfer calculations performed within the pertinent "spherical cap" geometry.

In this section possible approaches and approximations are described for incorporating both sphericity and multiple scattering in diurnal calculations for free radical species (e.g., ClO, ClNO<sub>3</sub>, HO<sub>2</sub>, OH, etc.) with emphasis on the behavior of concentrations at dawn and dusk. The effect of molecular scattering and surface reflection is included in the calculation of relevant photodissociation rates. In support of these aims, the following tasks have been performed:

- . investigation of optimal methods to evaluate the primary source function in the spherical shell geometry
- . formulation of the multiple scattering problem including surface reflection
- . evaluation of profiles of atmospheric optical properties at dissociative wavelengths
- . evaluation of single scattered dissociative fluxes and comparison with both pure absorption and multiple scattering results
- . evaluation of single scattered photodissociation rates and comparison with both pure absorption and multiple scattering results
- . evaluation of single scattered photodissociation rates for the spherical shell atmosphere near dawn/dusk
- . calculation of diurnal variations of radical species using single scatter photodissociation rates for the spherical geometry and comparison with plane-parallel pure absorption results
- . formulation of an approach to include higher orders of scattering and investigation of its convergence to multiple scattering results
- . formulation of an approach to incorporate a priori information on diurnal variations of photochemically active absorbers within occultation based inversion algorithms.

These results may be used to classify the atmosphere into regions where: (a) molecular scattering may be ignored, (b) single scattering can adequately account for the effect of molecular scattering, and (c) higher order scattering must be considered. Such information is crucial to the development of computationally efficient model algorithms.

#### 4.2 Role of Earth Curvature and Scattering in Diurnal Photochemical Modeling

Photodissociative processes play a significant role in current descriptions of atmospheric chemistry. Even the basic four reaction, oxygen-only model of Chapman (1931) includes two key photolytic reactions:



The photodissociation rate,  $j(\text{s}^{-1})$ , of such processes is given by:

$$j^i(z, \theta_0) = \int_{\Delta\lambda} \sigma_{\lambda}^i \phi_{\lambda}^i F_{\lambda}^d(z, \theta_0) d\lambda \quad (4-3)$$

where  $\sigma_{\lambda}^i$  is the wavelength dependent photodissociation cross-section for species  $i$  ( $\text{cm}^2$ )  
 $\phi_{\lambda}^i$  is the corresponding wavelength dependent quantum yield (nd)  
 $F_{\lambda}^d$  is the available dissociative flux at wavelength  $\lambda$ , altitude  $z$ , and solar zenith angle  $\theta_0$  (photons  $\text{cm}^{-2} \text{s}^{-1} \text{\AA}^{-1}$ ).

The time of day,  $t$ , determines the value of the local solar zenith angle  $\theta_0$  as described in Appendix A. The dissociative flux is given by the angle integrated specific

intensity  $I_\lambda$  (photons  $\text{cm}^{-2} \text{s}^{-1} \text{\AA}^{-1} \text{sr}^{-1}$ )

$$F_\lambda^d(z, \theta_0) = \int_{\Omega} I_\lambda(z, \theta_0) d\Omega \quad (4-4)$$

where  $I_\lambda$  is the solution to the general radiative transfer equation (Lenoble, 1977):

$$\begin{aligned} (\bar{\Omega} \cdot \bar{\nabla}) I_\lambda(\bar{r}, \bar{\Omega}) = \\ -\beta_\lambda(\bar{r}) [I_\lambda(\bar{r}, \bar{\Omega}) - J_\lambda(\bar{r}, \bar{\Omega})] \end{aligned} \quad (4-5)$$

where  $\bar{r}$  is a position vector,  $\bar{\Omega}$  is a unit vector in the direction along which variations in the intensity are sought,  $\beta_\lambda (\text{m}^{-1})$  is the total extinction coefficient describing the loss in intensity due to both scattering and absorption processes, and  $J_\lambda$  is the source function determined by scattered contributions to the intensity field.

Solution of equation (4-5) for a given model atmosphere requires an understanding of both: (a) the geometry of the atmosphere and (b) the relevant transfer processes (i.e., absorption, scattering) involved at a given wavelength. For example, in the simplest case, assuming a plane-parallel (PP) atmosphere, (appropriate for  $\theta_0 \lesssim 80^\circ$ )  $\bar{\Omega}$  reduces to the local normal  $\hat{n}$  and dependence on  $\bar{r}$  to that on altitude,  $z(\text{km})$ . If additionally scattering is neglected (i.e., pure absorption (PA)], the source function  $J_\lambda$  is identically zero and a simple form for  $F_\lambda^d$  emerges:

$$F_\lambda^{d, PP, PA} = F_\lambda T_\lambda^{PP}(z, \theta_0) \quad (4-6)$$

where  $\pi F_\lambda$  is the unattenuated solar flux at the top of the atmosphere and  $T_\lambda^{PP}(z, \theta_0)$  is the transmission function from the top of the atmosphere to altitude  $z$  along a path at solar zenith angle  $\theta_0$  given by:

$$T_{\lambda}^{PP}(z, \theta_0) = \exp\left\{-\sec\theta_0 \sum_{i=1}^K [\sigma_{\lambda}^i N_V^i(z)]\right\} \quad (4-7)$$

for K total absorbers where  $N_V^i(z)$  is the vertical column density ( $\text{cm}^{-2}$ ) for absorber i from level z to space. The quantity in brackets is the corresponding vertical (or normal) optical depth,  $\tau_V^i$ .

When scattering is included in the plane-parallel (PP) geometry, a variety of techniques are available to solve the radiative transfer equation (see Hansen and Travis, 1974; Lenoble, 1977). However, near dawn and dusk, the large solar zenith angles characterizing these situations ( $\theta_0 \gtrsim 80^\circ$ ) necessitate consideration of the Earth's sphericity in evaluating path extinction of incident solar radiation. Thus, even in the pure absorption (PA) case described above, the transmission function (4-7) must be modified to account for Earth curvature. Appropriate modifications are discussed in §4.3.

When scattering processes are additionally to be included, appropriate solutions to the general radiative transfer equation (4-5) must be sought. These will be described in §4.4.

### 4.3 Optical Paths in a Spherical Shell Atmosphere

#### 4.3.1 Geometric Considerations

As the solar zenith angle,  $\theta_0$ , approaches  $90^\circ$  (i.e., near dawn and dusk), equation (4-7) suggests that the transmission of all incident solar radiation (regardless of wavelength) approaches zero very rapidly. This is contrary to experience. It is generally recognized that application of the plane-parallel approximation becomes inappropriate in these special cases and furthermore other physical

phenomena such as refraction enter the problem. To facilitate evaluation of diurnally dependent dissociative fluxes, it is desirable to consider formulations which allow for a smooth transition between plane-parallel situations and those constrained by the spherical shell nature of the atmosphere. Ideally values of the solar zenith angle greater than  $90^\circ$  should be admitted to account for illumination of higher altitudes (above the terminator) at predawn and post-dusk times. In this section, generalizations of the direct solar beam transmission function analogous to equation (4-7) are discussed. The significance of this function twofold: (1) when scattering is neglected, it determines the locally available dissociative flux, and (2) when scattering is treated, it additionally enters into the calculation of the primary source function for scattering.

#### 4.3.2 Air Mass Factor Formulation

Transmission of incident solar radiation of wavelength  $\lambda$  along a ray path  $s$  at solar zenith angle  $\theta_0$  to the local normal  $\hat{n}$  at altitude  $z$  will be given by the transmission function  $T$ :

$$T_\lambda(z, \theta_0) = \exp [-\tau_\lambda(z, \theta_0)] \quad (4-8)$$

where the slant path optical depth  $\tau_\lambda(z, \theta_0)$  is defined as:

$$\tau_\lambda(z, \theta_0) = \sum_i^K \sigma_\lambda^i \left[ \int_0^{s(z, \theta_0)} n^i(s') ds' \right] \quad (4-9)$$

where:  $n^i(s)$  is the number density of the  $i^{\text{th}}$  species along geometric ray path  $s$  ( $\text{cm}^{-3}$ )

and  $ds'$  is the incremental path length along the ray path from source to level specified.

This expression allows for extinction due to  $K$  optically active species. The quantity in brackets may be defined

as the slant path column density ( $\text{cm}^{-2}$ ) of species  $i$  or:

$$N^i(z, \theta_0) = \int_0^{s(z, \theta_0)} n^i(s') ds' \quad (4-10)$$

In the plane-parallel (PP) limit, the incremental path length,  $ds'$ , and its projection on the local normal vector  $\hat{n}$ ,  $dz'$ , are related by:

$$ds' = \sec \theta_0 dz' \quad (4-11)$$

yielding:

$$\tau_\lambda(z, \theta_0) = \sec \theta_0 \sum_i^K \sigma_\lambda^i N_V^i(z) \quad (4-12)$$

where

$$N_V^i(z) = \int_z^\infty n^i(z') dz' \quad (4-13)$$

and

$$N^i(z, \theta_0) = \sec \theta_0 N_V^i(z) \quad (4-14)$$

Here  $N_V^i(z)$  is the vertical column density of species  $i$  from level  $z$  to the top of the atmosphere along the normal vector. The ratio of slant path to vertical column density defines a plane-parallel slant path air mass factor for all  $i$  and  $z$ :

$$M_{PP}^i(\theta_0) = \frac{N^i(z, \theta_0)}{N_V^i(z)} = \sec \theta_0 \quad (4-15)$$

Thus, from equation (4-12), the slant path optical depth may be determined from:

$$\tau_\lambda(z, \theta_0) = \sum_i^K \tau_V^i M^i(z, \theta_0) \quad (4-16)$$

where  $\tau_V^i$  is the wavelength dependent vertical optical depth above level  $z$  given by:

$$\tau_V^i(z) = \sigma_\lambda^i N_V^i(z) \quad (4-17)$$

The approach employed in equation (4-16) may be applied to situations where the plane-parallel approximation is not applicable by formulating appropriate generalized functions,  $M^i(z, \theta_0)$ .

#### 4.3.3 The Chapman Function

For grazing incidence (values of  $\theta_0$  approaching and greater than  $90^\circ$ ), the geometry of the problem is illustrated schematically in Figure 4-1. The atmosphere is assumed to be spherically symmetric, that is the number density profiles are of the form:

$$n^i = n^i(r) \quad (4-18)$$

where

$$r = R + z \quad (4-19)$$

and  $R$  is the planetary radius. (The value of  $R$  is assumed to be 6371 km, the Earth's radius at about  $35^\circ\text{N}$ .) Neglecting refraction, from simple geometric considerations:

$$(R + z) \sin\theta_0 = (R + z') \sin\theta' \quad (4-20)$$

and

$$ds' = dz' \sec\theta' = dz' \left[ 1 - \left( \frac{R+z}{R+z'} \right)^2 \sin^2\theta_0 \right]^{-1/2} \quad (4-21)$$

The desired slant column density at  $z$  along the path at solar zenith angle  $\theta_0$  will be [from (4-10)]:

$$N^i(z, \theta_0) = \int_z^\infty n^i(z') \left[ 1 - \left( \frac{R+z}{R+z'} \right)^2 \sin^2\theta_0 \right]^{-1/2} dz' \quad (4-22)$$

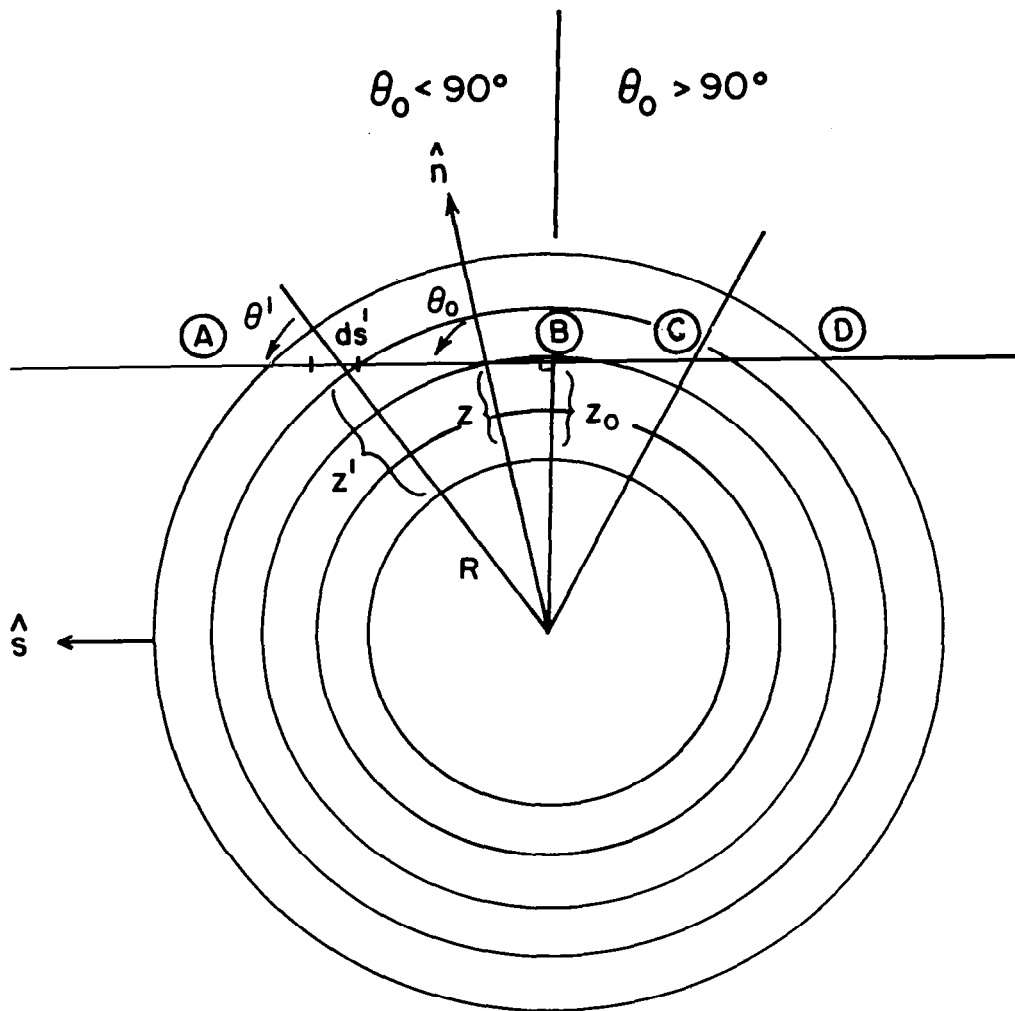


Figure 4-1  
Tangent Path Geometry.

Assuming a number density distribution with constant scale height  $H^i$ :

$$n^i(z') = n^i(z) \exp(-z'/H^i) \quad (4-23)$$

and using  $\theta'$  as the integration variable, (4-22) may be expressed as:

$$\begin{aligned} N^i(z, \theta_0) &= \\ n^i(z) H^i X^i \sin \theta_0 \int_0^{\theta_0} \csc^2 \theta' \exp X^i \left(1 - \frac{\sin \theta_0}{\sin \theta'}\right) d\theta' & \\ &= n^i(z) H^i \text{Ch}(X^i, \theta_0) & \\ &= n^i(z) H^i M_{\text{Sp}}^1(z, \theta_0) \end{aligned} \quad (4-24)$$

where  $\text{Ch}(X^i, \theta_0)$  is the Chapman (1931) function and the parameter  $X^i$  is:

$$X^i = (R + z)/H^i \quad (4-25)$$

This expression has been tabulated by Wilkes (1954) and is valid for  $\theta_0 \leq 90^\circ$ . Figure 4-2 compares the Chapman function  $M_{\text{Sp}}^1(\theta_0)$  with the plane-parallel air mass factor (i.e.,  $\sec \theta_0$ )  $M_{\text{PP}}(\theta_0)$  for a uniformly mixed gas ( $\text{O}_2$  or M).  $M_{\text{Sp}}^1(\theta_0)$  assumes a constant scale height equal to 8.0 km. For  $\theta_0 > 90^\circ$ , the Chapman function has been analytically extended using (see Figure 4-1):

$$\begin{aligned} N^i(z, \theta_0 > 90^\circ, \text{A} \rightarrow \text{C}) &= 2N^i(z_0, \theta_0 = 90^\circ, \text{A} \rightarrow \text{B}) \\ &\quad - N^i(z, 180 - \theta_0, \text{C} \rightarrow \text{D}) \end{aligned} \quad (4-26)$$

although this approach is not appropriate as discussed by Swider (1964). Note that  $M_{\text{PP}}$  and  $M_{\text{Sp}}^1$  diverge as  $\theta_0$  approaches  $90^\circ$ . From equation (4-16) the slant path optical depth may be expressed as:

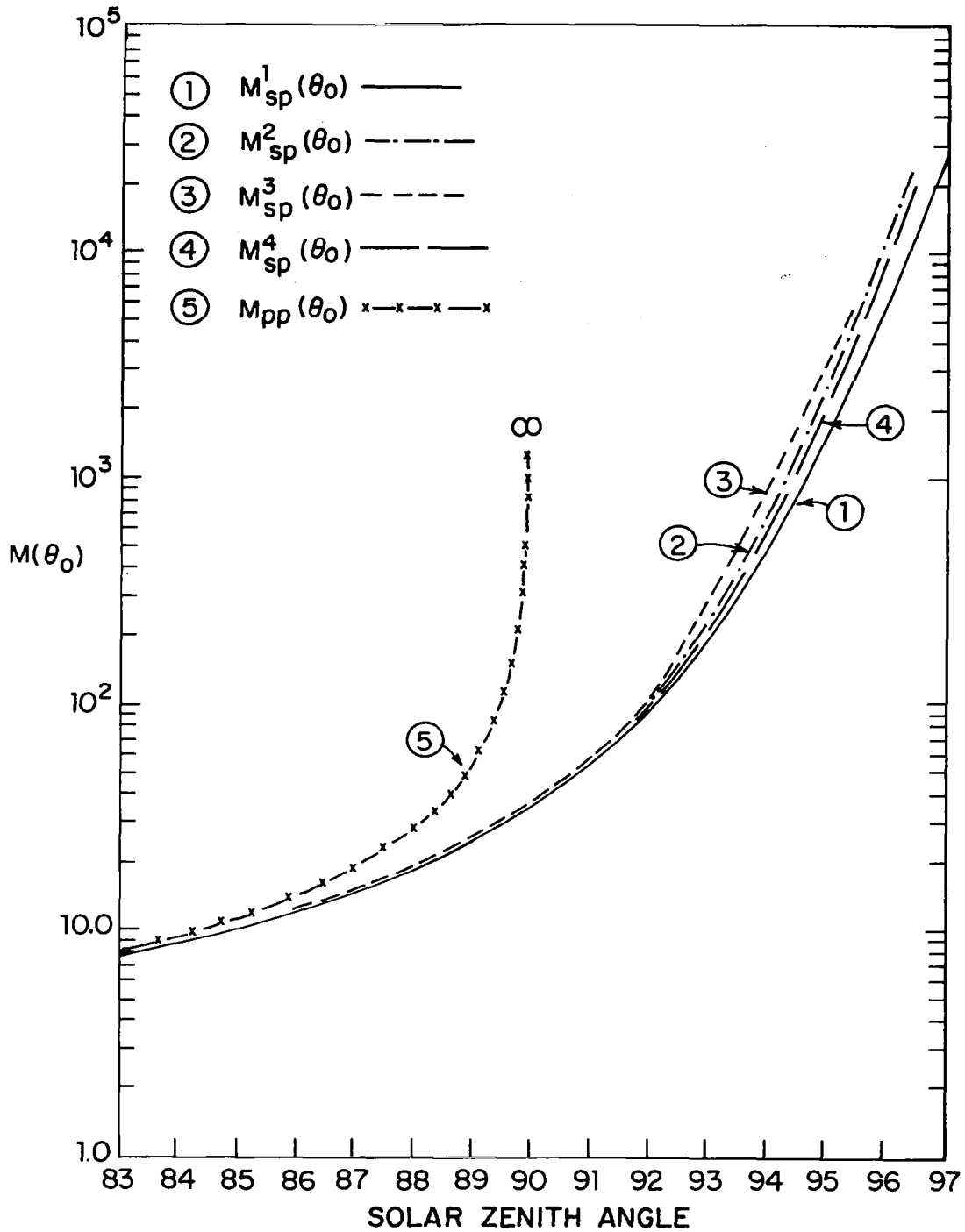


Figure 4-2

Comparison of air mass factors  $M(\theta_0)$  for: (1) Chapman function, (2) Generalized Chapman function, (3) Numerical, (4) Numerical with Refraction, and (5) Plane Parallel.

$$\tau_{\lambda}(z, \theta_0) = \sum_i^K \tau_V^i \text{Ch}(X^i, \theta_0) \quad (4-27)$$

with appropriate choice of  $X^i$ . Extensions to the Chapman function include work by Swider (1964) who investigated atmospheres with scale height gradients and Green and Martin (1966) who generalized the analysis for various density distributions.

#### 4.3.4 Other Analytical Treatments

Swider (1964) noted that in the terrestrial atmosphere scale height variations with altitude occur and values of the Chapman function are most sensitive to parameters (scale heights and number densities) near the lowest altitude level encountered along the appropriate ray path. For zenith angles greater than  $90^\circ$ , this level is near the grazing altitude (or tangent height)  $z_0$ . (see Figure 4-1). By incorporating these considerations simplified approximations have been derived by numerous authors including those by Smith and Smith (1972) from the work of Swider (1964) and Fitzmaurice (1964). For  $\theta_0 \leq 90^\circ$ :

$$M_{Sp}^2(z, \theta_0 \leq 90^\circ) = \left(\frac{\pi}{2} X_z^i\right)^{\frac{1}{2}} \exp(y^i)^2 \text{erfc } y^i \quad (4-28)$$

Noting that  $M_{Sp}^2(z, \theta_0 = 90^\circ) \sim \left(\frac{\pi}{2} X_z^i\right)^{\frac{1}{2}}$  relation equation (4-27) can be used to derive an expression for  $\theta_0 > 90^\circ$ :

$$M_{Sp}^2(z, \theta_0 > 90^\circ) = \left(\frac{\pi}{2} X_{z_0}^i\right)^{\frac{1}{2}} \frac{H_0^i}{H_z^i n_z^i} [2n_0^i - n_z^i \exp(y^i)^2 \text{erfc } y^i] \quad (4-29)$$

where:  $n_0^i$  = number density at tangent height  $z_0$ .  
 $n_z^i$  = number density at level  $z$

$$\begin{aligned}
H_0^i &= \text{scale height at tangent height} \\
H_z^i &= \text{scale height at level } z \\
x_0^i &= (R+z_0)/H_0^i \\
x_z^i &= (R+z)/H_z^i \\
y^i &= (x_z^i/2)^{1/2} |\cos\theta_0|
\end{aligned}$$

and  $\text{erfc} = \text{complimentary error function } (=1-\text{erf})$ .  
 Expression (4-29) accounts for scale height variability in a realistic terrestrial atmosphere. Figure 4-2 compares air mass factors  $M_{\text{Sp}}^2$  as a function of solar zenith angle with the constant scale height Chapman function.  $M_{\text{Sp}}^2$  was evaluated using the scale height and total number density profiles of the U.S. Standard Atmosphere (1976).

#### 4.3.5 Numerical Forms (including refractive effects)

Slant path column density  $N^i(z, \theta_0)$  [and hence air mass  $M(z, \theta_0)$ ] may be explicitly evaluated by numerical integration of the line integral in equation (4-10) along the appropriate ray path. Advantages offered by this approach include capabilities to: (a) incorporate realistic number density profiles,  $n^i(s')$ , for each species, and (b) include the effects of refraction within the atmosphere.

Arbitrary number density profiles may be incorporated into the analysis by integrating equation (4-22) with suitable quadrature for a specified profile  $n^i(z')$  taken as a series of concentric locally homogeneous shells. The resultant air mass factor  $M_{\text{Sp}}^3(\theta_0)$  using the number density profile cited above is also illustrated in Figure 4-2. For comparison, previously discussed air mass factors are also provided.

The effect of refraction on optical path for zenith angles,  $\theta_0 > 90^\circ$ , is schematically illustrated in Figure

4-3. In the absence of refraction, the appropriate optical path integral is along (b) at tangent height  $z_0$ , for rays reaching altitude  $z$  at astronomical zenith angle,  $\theta_0$ . The unrefracted tangent height is simply determined geometrically:

$$z_0 = (R + z)\sin(180-\theta_0) - R \quad (4-30)$$

for  $\theta_0 > 90^\circ$ . With refraction, the apparent angle of arrival is  $\theta'_0$  and the minimum height of the refracted ray is  $z'_0$ . For monotonically decreasing density profiles the minimum height of the refracted path is always greater than that for the unrefracted path, Snider (1975):

$$z'_0 - z_0 > 0 \quad (4-31)$$

Sample calculations of the error in the minimum height due to refraction equation (4-31) performed using the procedure described in Appendix B are shown in Figure 4-4 for values of  $z = 25, 35, 45, 55, 65$  km. Note that the error is greatest for high altitudes at large zenith angles (low minimum heights). Since the column density for  $\theta_0 > 90^\circ$  is most sensitive to the relevant number density near the tangent altitude [ $n_0$ , see equation (4-29)], the effect of refraction is to decrease the air mass. Neglecting refraction, therefore, causes air mass to be overestimated (Snider, 1975).

Calculations of refracted air mass factor  $M_{Sp}^4(\theta_0)$  follow a procedure based on Selby and McClatchey (1972). Essentially, equation (4-22) is modified by a factor dependent on the phase refractive index of air,  $\tilde{m}(z)$  with the resultant air mass factor given by (see Appendix B):

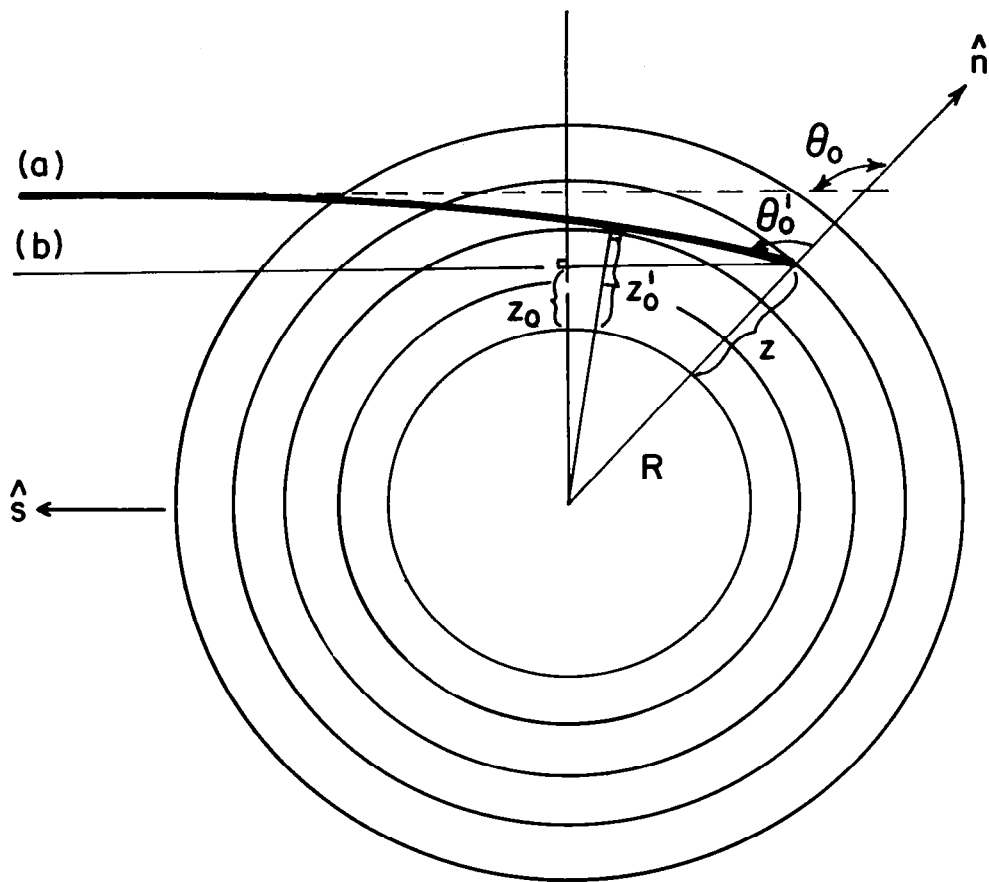


Figure 4-3  
 Effect of Refraction on Tangent Path.

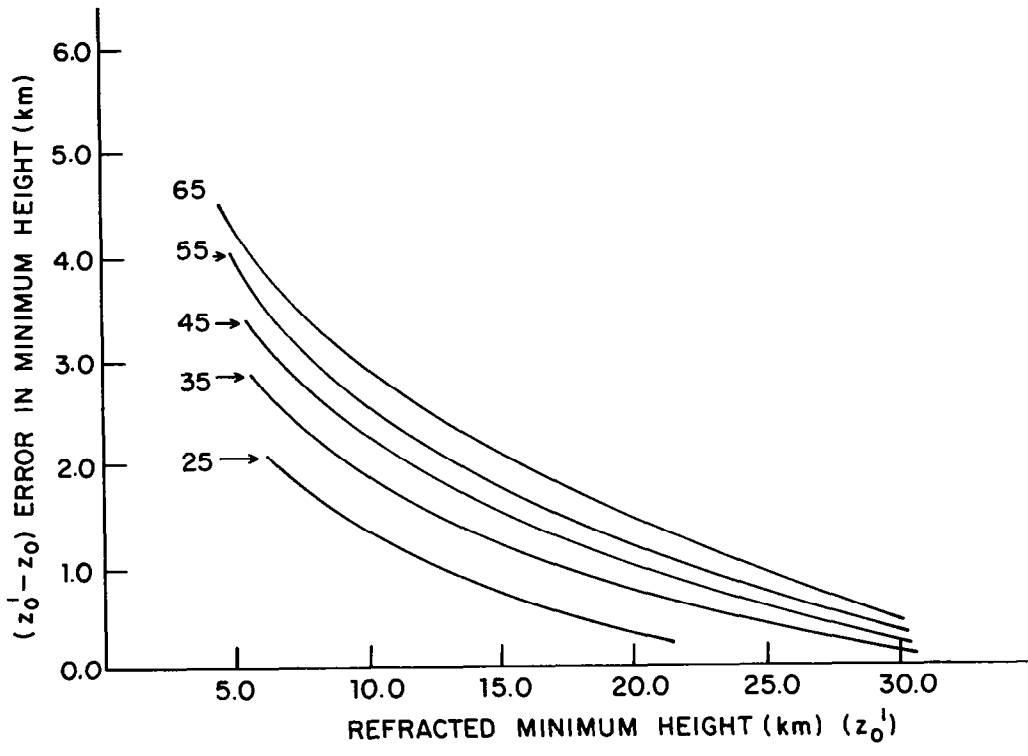


Figure 4-4  
 Calculated Error in Tangent Height Due to Refraction at  
 Indicated Altitude.

$$M_{Sp}^4(z, \theta_o) = \frac{1}{n^i(z) H_z} \int_z^\infty n^i(z') \left\{ 1 - \left[ \frac{(R+z)\tilde{m}(z)}{(R+z')\tilde{m}(z')} \right]^2 \right. \\ \left. \sin^2 \theta_o \right\}^{-\frac{1}{2}} dz' \quad (4-32)$$

Results based on the procedure detailed in Appendix B are also illustrated in Figure 4-2. Note that the refracted air mass is less than that for a realistic profile ignoring refraction (i.e.,  $M_{Sp}^3$ ). This error for selected angles is given in Table 4-1. The error increases markedly for large solar zenith angles.

#### 4.3.6 Summary

The differences among the various spherical approaches illustrated in Figure 4-2 is not as striking as that between the plane-parallel and spherical treatments. To avoid time consuming line integrals and yet retain the scale height dependence of the true atmosphere we have retained the  $M_{Sp}^2(\theta_o)$  approach (which is intermediate in value). As applied to model calculations of solar beam extinction, optical paths are evaluated using equation (4-16) such that:

$$\tau_\lambda(z, \theta_o) = \sum_{i=1}^K \tau_v^i M^i(z, \theta_o) \quad (4-33)$$

where  $M^i(z, \theta_o) = \sec \theta_o \quad \theta_o < 80^\circ$

$M^i(z, \theta_o) = M_{Sp}^2(\theta_o) \quad \theta_o \geq 80^\circ$

In the current treatment three species (i.e., sources of extinction) are handled (i.e.,  $K=3$ ):  $O_2$ ,  $O_3$ , and Rayleigh scattering (M). Appropriate choices of scale height and number density profiles are used in (4-28, 4-29) depending on whether air mass factors for ( $O_2$ , M) or  $O_3$  are

TABLE 4-1

## Computed Air Masses and Error in Neglecting Refraction

<u><math>\theta_0</math></u>	<u><math>M_{Sp}^3 (\theta_0)</math></u>	<u><math>M_{Sp}^4 (\theta_0)</math></u>	<u><math>\Delta (\%)</math></u>
92.3	126.4	122.0	3.7
94.0	700.5	580.8	20.6
95.2	4177.6	2999.	39.2
96.4	22030.	15328.	43.7

being calculated. Thus, the transmission function in a spherical shell atmosphere  $T_{\lambda}^{Sp}(z, \theta_0)$  [analogous to equation (4-7)] becomes:

$$T_{\lambda}^{Sp}(z, \theta_0) = \exp - \left[ \sum_{i=1}^K \tau_{\nu}^i M^i(z, \theta_0) \right] \quad (4-34)$$

and the dissociative flux due to attenuation (including scattering of the direct solar beam (but excluding multiply scattered contributions) is :

$$F_{\lambda}^{d, Sp} = F_{\lambda} T_{\lambda}^{Sp}(z, \theta_0) \quad (4-35)$$

For ozone, a similar approach is adopted (valid above 25 km) modifying the ozone scale height to be equal to 2/3 the ambient pressure scale height. This assumption is based on a simple first order ozone profile determined by photochemical equilibrium. Calculations indicate an error of less than 5 percent down to 30 km using this approach (see Fig. 4-5).

#### 4.4 Treatment of Multiple Scattering in the Spherical Shell Geometry

##### 4.4.1 The General Problem

Solutions presented in the previous section (equations 4-34, 4-35) neglect contributions to the dissociative flux due to the scattered or diffuse intensity field at a given level. To include multiply scattered radiation in the spherical shell geometry, the radiative transfer equation (4-5) must be treated with appropriate definition of the  $(\bar{\Omega} \cdot \bar{\nabla})$  operator and source function  $J_{\lambda}(\bar{r}, \bar{\Omega})$ . While the problem of multiple scattering in spherical shell atmospheres has been treated in the study of stellar interiors (cf. Chandrasekhar, 1960) the problem is somewhat simpler

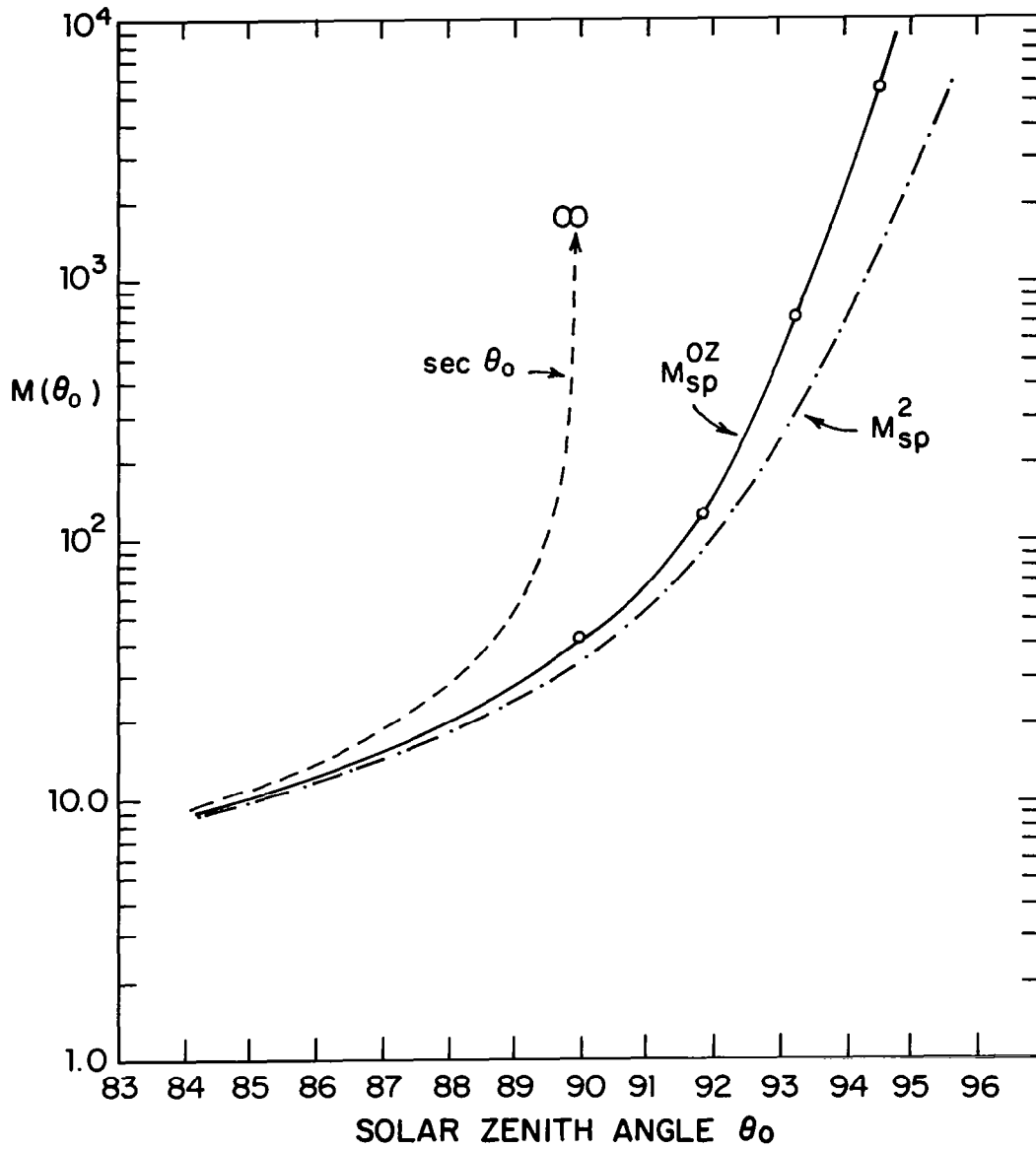


Figure 4-5

Air mass factors for ozone ( $M_{sp}^{OZ}$ ) and oxygen absorption and Rayleigh scattering ( $M_{sp}^2$ ).

in that case since both the source function and atmosphere have spherical symmetry. In the present context however, the spherical shell atmosphere is externally illuminated by plane-parallel radiation and overall symmetry is lost. Thus, while it is relatively straightforward to write down the relevant form of the radiative transfer equation (see Fymat, 1977), methods of solution may be tedious.

An examination of alternative approaches to the problem indicates three general methodologies:

- (a) Monte Carlo - (Collins and Wells, 1965; Marchuk and Mikhailov, 1967; Antyufeyev and Nazaraliyev, 1973)
- (b) the DART method - (Whitney et al. 1973; Whitney, 1977; Whitney and Malshow, 1977)
- (c) approximate semi-analytical methods-(Shettle and Green, 1974; Sobolev, 1975).

Considerations of computational efficiency for radiative transfer schemes incorporated within the diurnal photochemical model severely constrain the applicability of approaches (a) and (b). Therefore, approximate semi-analytical techniques have been investigated. They may provide viable alternative methods of solution, especially when potential errors are assessed relative to other photochemical model uncertainties. One such approach is the "locally plane-parallel" (LPP) approximation explored by Sobolev (1975).

#### 4.4.2 Locally Plane-Parallel Approximation

The conventional plane-parallel (PP) approximation assumes a plane-parallel atmosphere uniformly illuminated by a plane-parallel source. As an approximate approach to treating the general spherical shell problem it may be assumed that the atmosphere consists of plane-parallel

layers (locally), illuminated locally, however, accounting for the spherical shell nature of the atmosphere (Sobolev, 1975). This procedure relaxes one of the assumptions of the plane-parallel approximation and should provide results with reasonable accuracy. Fundamentally, the methodology requires calculations of the primary source function for scattering exactly (that is, accounting for Earth curvature) and approximating multiple scattering using the PP approximation.

By adopting the LPP approach, equation (4-5) becomes (wavelength suffix omitted):

$$\cos \theta \frac{\partial I}{\partial \tau}(\tau, \theta) = I(\tau, \theta) - J(\tau, \theta) \quad (4-36)$$

where  $\theta$  is the local zenith angle and  $\tau(z)$  is the total vertical optical depth to altitude  $z$  given by:

$$\tau(z) = \sum_{i=1}^K \tau_V^i(z) \quad (4-37)$$

The source function at altitude  $\tau(z)$  is given by<sup>†</sup>:

$$J(\tau) = J_0(\tau) + \frac{\omega_0(\tau)}{2} \int_{-1}^{+1} I(\tau, \mu) d\mu \quad (4-38)$$

where  $\mu$  is the cosine of the zenith angle ( $\cos \theta$ ),  $\omega_0(\tau)$  is the single scattering albedo given by:

$$\omega_0(\tau) = \sigma_R n^M / \sum_{i=1}^K \sigma_i n^i \quad (4-39)$$

---

<sup>†</sup> This form and subsequent results assume isotropic scattering. Anderson and Meier (1979) have demonstrated that isotropic scattering provides a good approximation to Rayleigh multiple scattering solutions throughout the wavelength range .28-.80  $\mu\text{m}$ .

where  $\sigma_R$  is the Rayleigh (molecular) scattering cross-section (Penndorf, 1957),  $n^M$  is the total number density, and  $J_o(\tau)$  is the primary source function:

$$J_o(\tau) = \frac{\omega_o(\tau)}{4} FT [\tau(z), \theta_o] \quad (4-40)$$

Profiles of optical depth and single scattering albedo vs altitude at dissociative wavelengths are illustrated in Figures 4-6 and 4-7, respectively.

The primary source function describes the planetary illumination source. In the plane-parallel approximation,  $T$  is given by equation (4-7) or:

$$J_o^{PP}(\tau) = \frac{\omega_o(\tau)}{4} F e^{-\tau \sec \theta_o} \quad (4-41)$$

In the LPP approach, the transmission function is defined by the spherical air mass factors described in the previous section [equation (4-34)] and:

$$J_o^{SP}(\tau) = \frac{\omega_o(\tau)}{4} FT^{SP} \quad (4-42)$$

#### 4.4.3 Method of Solution

A variety of techniques are available to solve equations (4-36) and (4-38) using the spherical source function equation (4-42) in the LLP approximation to obtain the intensity field,  $I_\lambda$ , and ultimately the dissociative flux,  $F_\lambda^d$ , through equation (4-4). The approach chosen for this application treats the single integral equation of the Fredholm type obtainable from equations (4-36) and (4-38) by suitable transformation (Busbridge, 1960):

$$J(\tau) = J_o(\tau) + \frac{\omega_o(\tau)}{2} \int_0^{\tau^*} E_1(|\tau-t|) J(t) dt \quad (4-43)$$

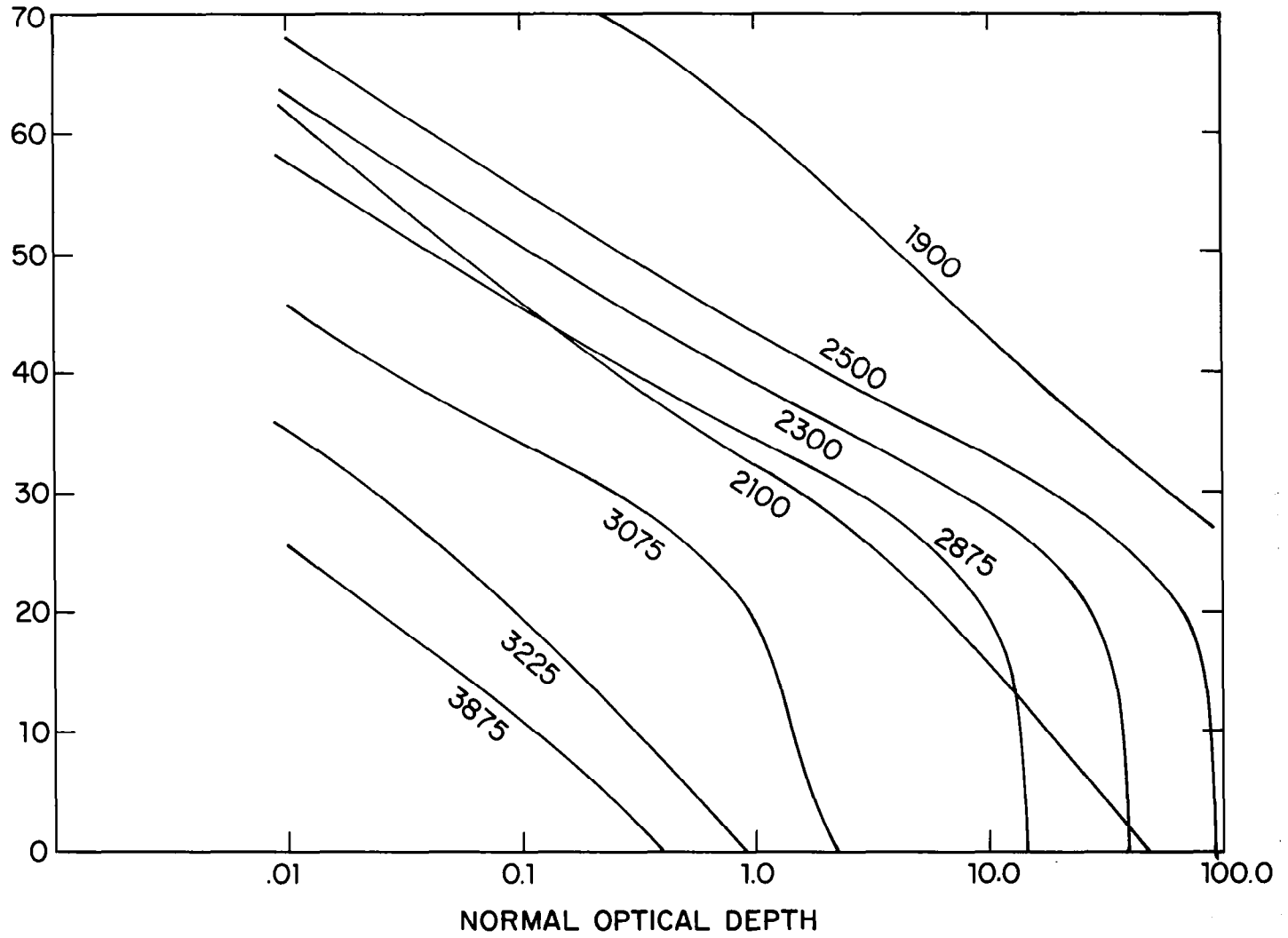


Figure 4-6  
Normal optical depth ( $\tau$ ) profile for indicated wavelength.

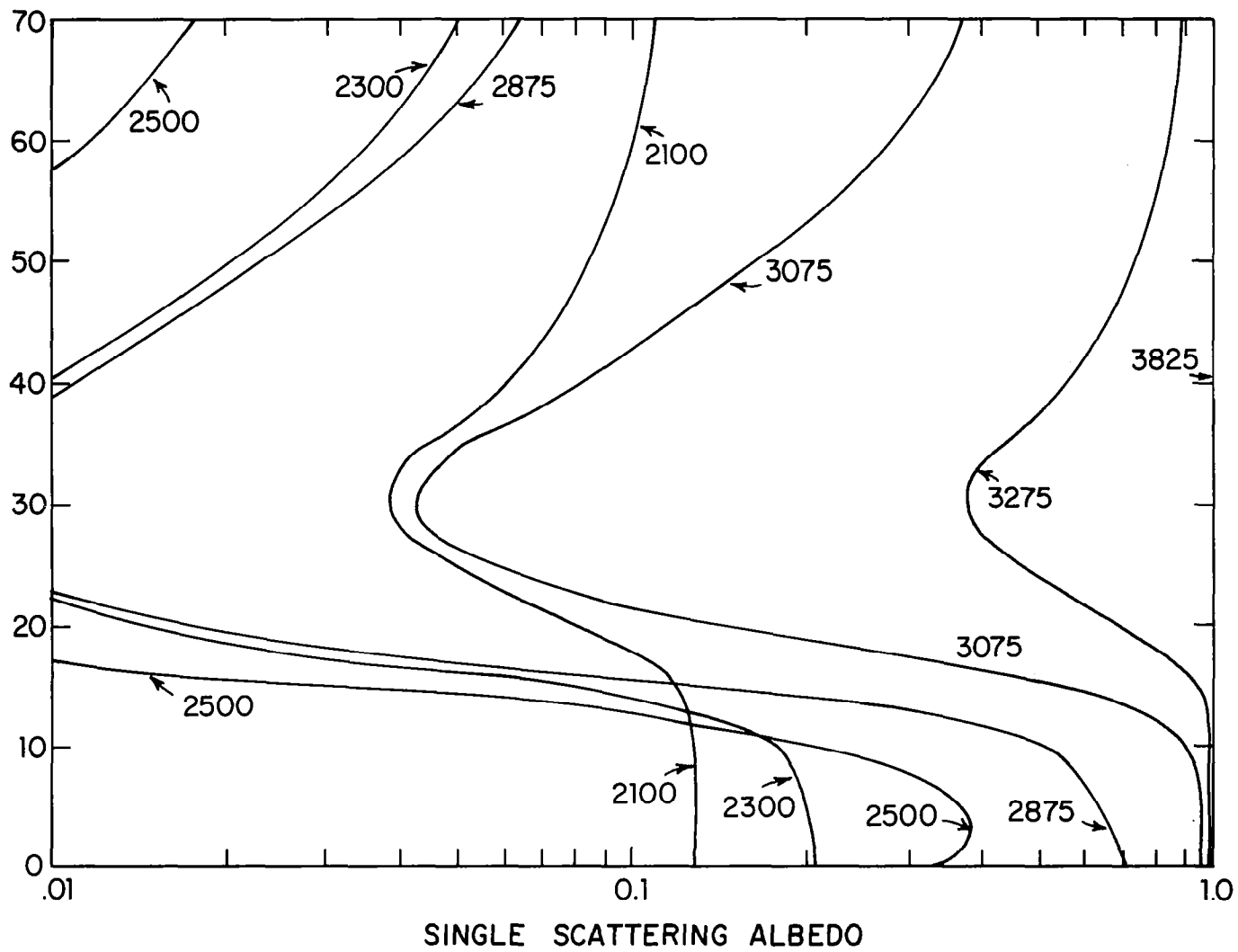


Figure 4-7

Single scattering albedo ( $\omega_0$ ) profile for indicated wavelength.

where  $E_1$  is the first exponential integral (see Appendix C) with general form:

$$E_n(x) = \int_0^1 e^{-x/\mu} \mu^{n-2} d\mu \quad (4-44)$$

and  $\tau^*$  is the total normal optical depth [i.e.,  $\tau^* = \tau(z=0)$ ]. When Lambert surface reflection of both the direct beam and scattered intensity field is included in the formulation, the integral equation for the source function becomes:

$$\begin{aligned} J(\tau) = & J_o(\tau) + \frac{\omega_o(\tau)}{2} \int_0^{\tau^*} J(t) E_1(\tau-t) dt \\ & + RE_2(\tau^*-\tau) [2 \cos\theta_o J_o(\tau^*) + \omega_o(\tau) \int_0^{\tau^*} J(t) \\ & E_2(\tau^*-t) dt] \end{aligned} \quad (4-45)$$

where  $R$  is the surface albedo. The required dissociative flux is immediately available noting:

$$F^d[\tau(z)] = \frac{4}{\omega_o[\tau(z)]} J[\tau(z)] \quad (4-46)$$

or alternatively:

$$\begin{aligned} F^d(\tau) = & FT(\tau, \theta_o) + 2 \int_0^{\tau^*} J(t) E_1(|\tau-t|) dt \\ & + 2RE_2(\tau^*-\tau) [\cos\theta_o FT(\tau^*, \theta_o) \\ & + 2 \int_0^{\tau^*} J(t) E_2(\tau^*-t) dt] \end{aligned} \quad (4-47)$$

where  $T[\tau(z), \theta_o]$  is the spherical transmission function

given by equation (4-34). The four terms in equation (4-47) above represent contributions to the dissociative flux due to: (a) attenuation of the direct solar beam, (b) the angle integrated diffuse (scattered) intensity field, (c) surface reflection of the attenuated direct solar beam, and (d) reflection of the surface incident angle integrated diffuse intensity field.

Since the source function  $J(\tau)$ , is proportional to the single scatter albedo,  $\omega_0(\tau)$ , [see equations (4-38), and (4-40)], the dissociative flux equation (4-47) reduces to the absorption only cases [equations (4-6), and (4-35)] when the albedo is identically zero (i.e., when there is no scattering).<sup>†</sup>

Solution of equation (4-45) is possible using a variety of techniques including variational methods (Sze, 1976) and iterative techniques (Irvine, 1965). Iterative techniques such as successive orders of scattering (SOS) are attractive since they easily accommodate the inhomogeneous nature of the atmosphere (as evidenced by the dependence of single scattering albedo on altitude shown in Fig. 4-7) and provide physical insight into the relative roles of single vs higher order scattering in determining dissociative fluxes. Furthermore, if only a few orders of scattering are required to reach a reasonable solution, SOS approaches may be computationally competitive with other multiple scattering treatments. SOS calculations converge rapidly to the desired accuracy for small values of single scattering albedo since the  $n^{\text{th}}$  order scattering contribution to the source function is proportional to  $\omega_0^n$  (Lenoble, 1977). Convergence slows as the albedo approaches unity

---

<sup>†</sup> With the exception of the surface reflected term which was not included in the previous development.

(very weak absorption) and computational times become prohibitive as total optical depths,  $\tau^*$ , become large (Nagel et al. 1978).

Examination of Fig. 4-7 suggests that the magnitude of the single scattering albedo will be small ( $<0.2$ ) at altitudes greater than approximately 15 km for dissociative wavelengths  $<3100 \text{ \AA}$ . Alternatively, when albedos approach unity (generally for  $\lambda > 3400 \text{ \AA}$ ), optical depths are generally less than 1.0 (see Fig. 4-6). Based on these observations an SOS treatment has been adopted to evaluate multiply scattered dissociative fluxes within the wavelength region of interest.

#### 4.4.4 Single Scattering Results

The first order effects of molecular scattering within the spherical shell atmosphere are due to single scattering. Since single scattering calculations are relatively straight-forward, it is of considerable interest to examine the degree of accuracy (compared to multiple scattering) obtainable by considering single scattering alone.

Equation (4-45) is quite amenable to a single scattering treatment by replacing the full source function,  $J$ , appearing in the integral terms with the primary term,  $J_0$  [equation (4-40)] alone. In the single scattering approximation:

$$F^d(\tau, \tau^*, \theta_0, R) = F\left\{T(\tau, \theta_0) + \frac{1}{2} \int_0^{\tau^*} f_0(t) E_1(t - \tau) dt\right. \\ \left. + RE_2(\tau^* - \tau) [2\cos\theta_0 T(\tau^*, \theta_0) + \int_0^{\tau^*} f_0(t) E_2(\tau^* - t) dt]\right\} \quad (4-48)$$

where

$$f_0(t) = \omega_0(t) T(t, \theta_0) \quad (4-49)$$

and  $T[\tau(z), \theta_0]$  is the transmission function.

Expression (4-48) is near analytical with the requirement that two integrals be evaluated. An efficient quadrature technique was developed using piecewise continuous functions and exploiting the recursion relation for exponential ( $E_n$ ) functions to evaluate the integral terms in equation (4-48) (see Appendix C).

Figures 4-8 and 4-9 summarize sample calculations of normalized dissociative fluxes (i.e.,  $F^d/F$ ) at wavelengths of 3475 Å and surface albedo 0.2 and 3075 Å,  $R = 0.0$ , respectively, for a solar zenith angle of 60°. Curve (1) [dotted] is the result for absorption only, curve (3) is the corresponding multiple scattering (MS) result from Luther and Gelinas (1976). Curve (2) is the single scattering result consisting of components (a,b,c,d) corresponding to the four terms in equation (4-48) above: (a) the attenuated direct solar beam, (b) the singly-scattered diffuse flux, (c) the surface-reflected direct solar beam, and (d) the surface-reflected singly scattered diffuse flux. At 3475 Å there is virtually complete transmission at all altitudes for a purely absorbing atmosphere. Therefore, consideration of scattering has a marked effect on the dissociative flux profile. Examining the individual contributions to the singly scattered dissociative flux (curve 2) in comparison to the MS result (curve 3), it is noted that the shape of the MS flux profile is largely determined by enhanced extinction of the direct solar beam to scattering in the lower atmosphere (curve a). As noted by Lacis and Hansen (1974), the lower atmosphere back-scatters a fraction of incident solar flux (curve b) to the upper atmosphere in a manner analogous to an effective surface reflection. Contributions due to surface reflection (curves c and d) are significant mainly in the lower atmosphere ( $z < 10$  km). Above 20 km, the SS flux profile

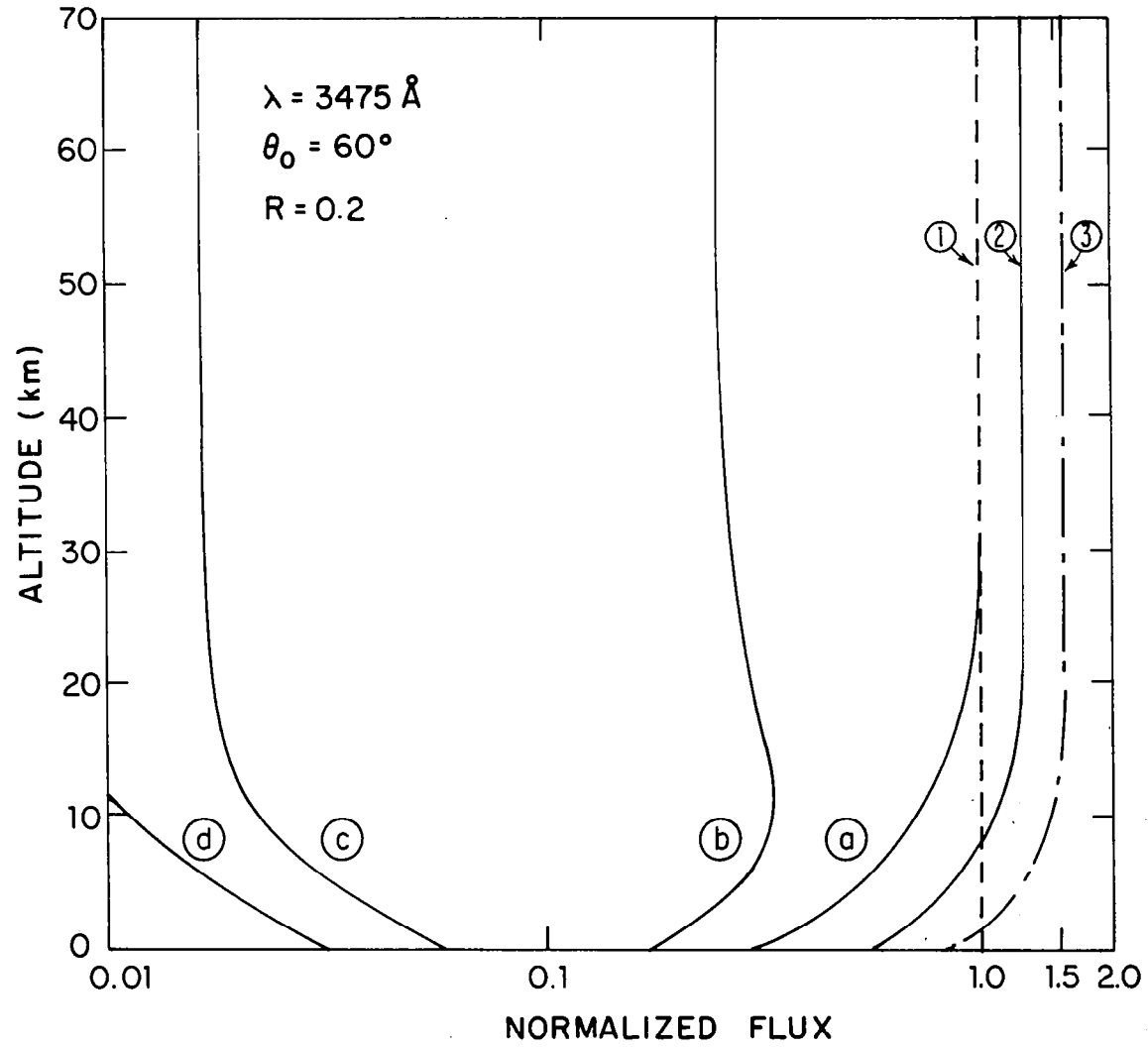


Figure 4-8  
Normalized dissociative flux profile ( $F^d/F$ ) at  $3475\text{\AA}$ ,  $\theta_0 = 60^\circ$ ,  $R = 0.2$ .

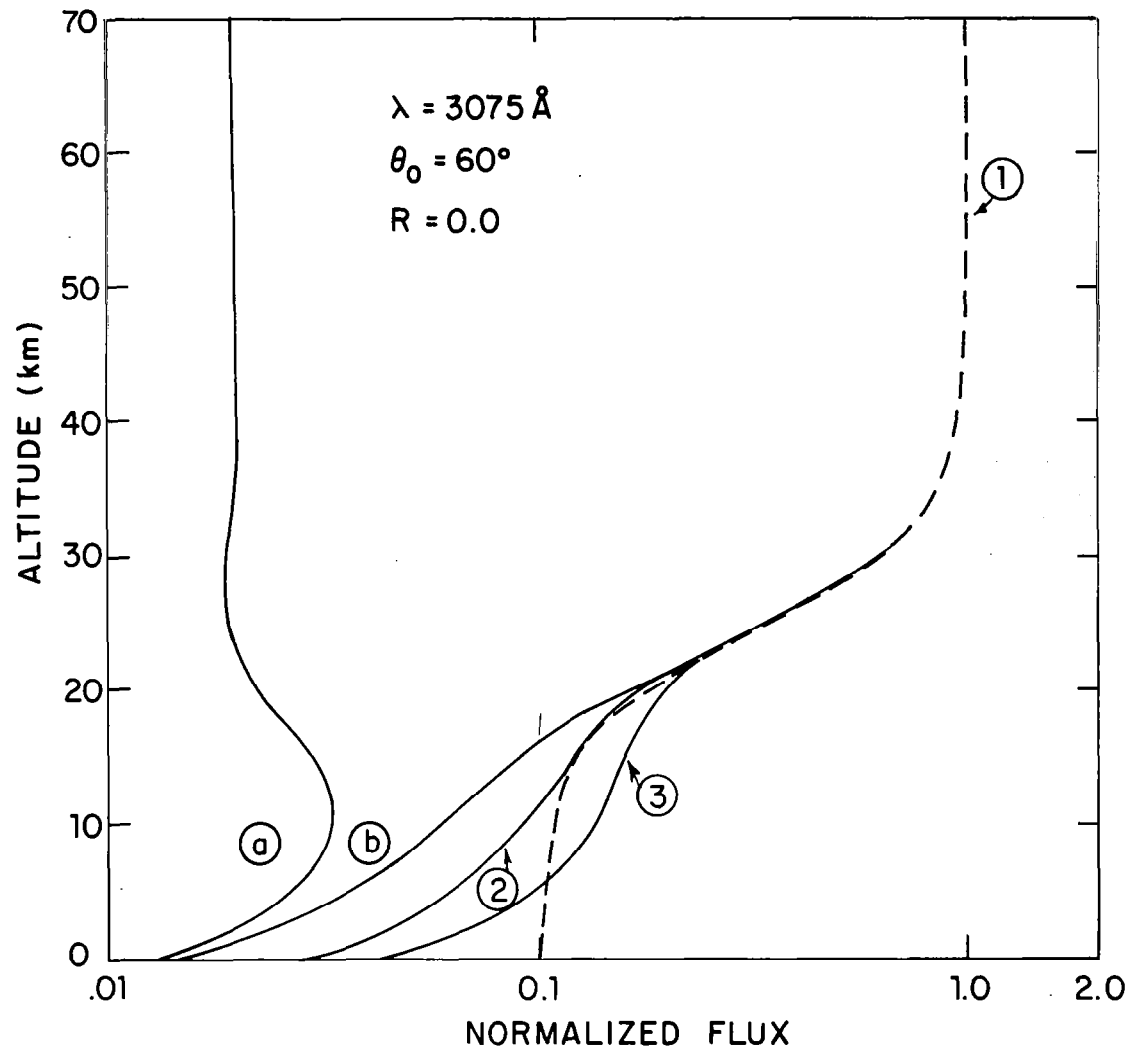


Figure 4-9  
 Normalized dissociative flux profile ( $F^d/F$ ) at  $3075\text{\AA}$ ,  $\theta_0 = 60^\circ$ ,  $R = 0.0$ .

underestimates the MS result by about 16 percent.

Absorption by the Hartley-Huggins bands of ozone dominates the dissociative flux profile for  $3075 \text{ \AA}$  at altitudes greater than 20 km. Below this level scattering contributions modify the profile from the absorption only case (curve 1). The SS results (curve 2) provide a reasonable estimate of the altitude dependence but due to increased optical depths the MS result (curve 3) is underestimated by as much as 35 percent near the surface.

Calculations described above are valid in the plane-parallel limit ( $\theta_0 = 60^\circ$ ). The spherical shell nature of the atmosphere becomes apparent at zenith angle greater than about  $80^\circ$ . Figure 4-10 shows single scattered dissociative flux profiles for solar zenith angles of  $60^\circ$ ,  $89^\circ$ ,  $92^\circ$  and  $96^\circ$ . At equinox and latitude  $30^\circ$  these zenith angles correspond to the local times given in Table 4-2 depending on whether dawn or dusk is considered. It is noteworthy that in the plane-parallel approximation dissociative fluxes at all altitudes are identically zero for  $\theta_0 \geq 90^\circ$  (i.e.,  $t \leq 0600$  or  $t \geq 1800$ ). As indicated there is no real singularity at dawn or dusk. In the approximate 14-minute period between  $\theta_0 = 89^\circ$  and  $92^\circ$ , fluxes above 30 km remain virtually unchanged. A feature which does appear at  $\theta_0 > 90^\circ$  due to the Earth's curvature is the terminator shadow which reaches a height of about 35 km approximately one-half hour before dawn and after dusk.

In order to assess the relative accuracy of the single scattering approach, multi-wavelength calculations of dissociative flux profiles in the range  $2500\text{-}4000 \text{ \AA}$  were performed using equation (4-48) for a solar zenith angle of  $60^\circ$ . Comparisons to multiple scattering results (Luther and Gelinis, 1976) for surface albedos of 0.0 and 0.25 are illustrated in Figs. 4-11 and 4-12, respectively. Plotted are percent errors defined as:

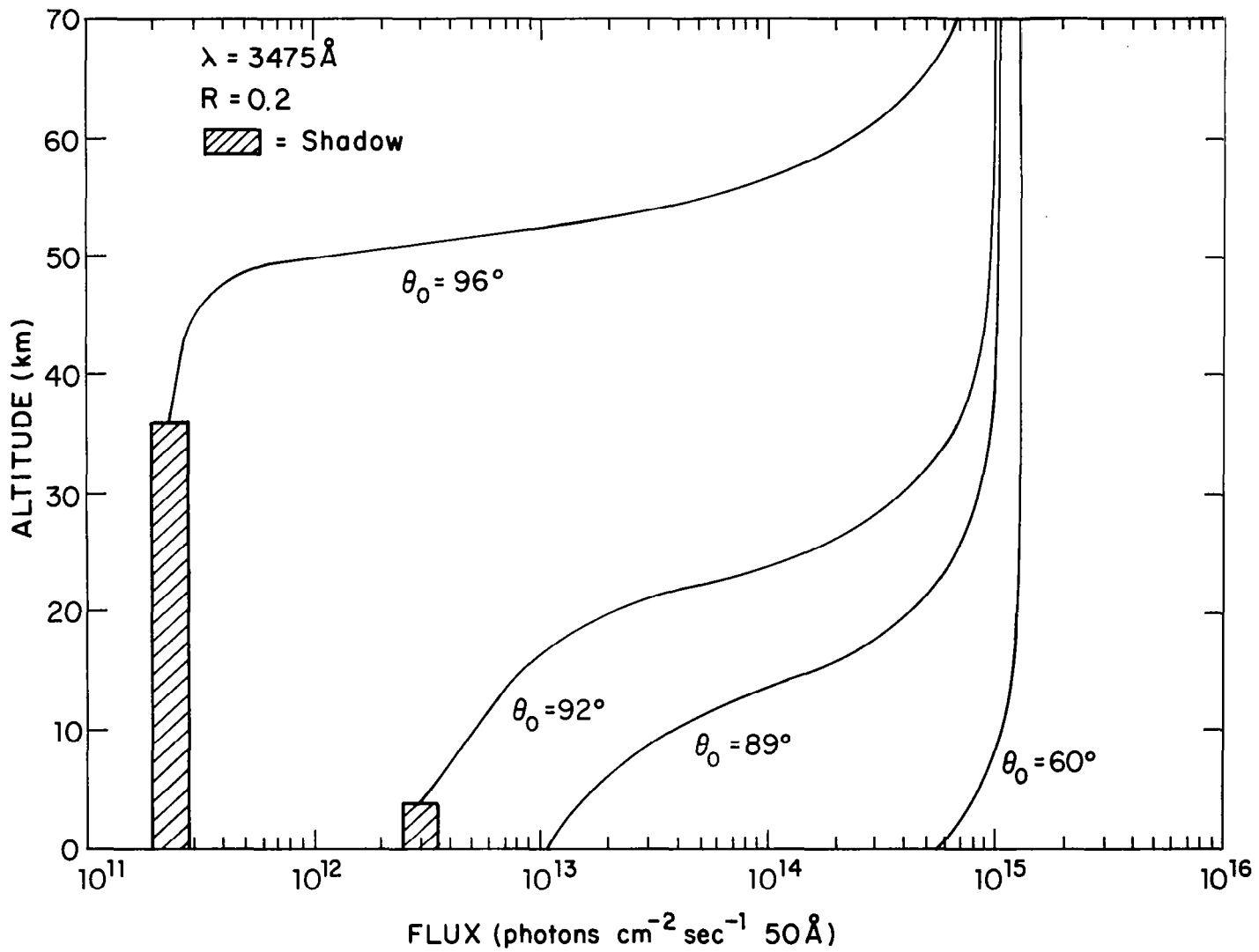


Figure 4-10

Dependence of dissociative flux profile ( $F^d$ ) on solar zenith angle in spherical geometry ( $\lambda = 3475 \text{ \AA}$ ,  $R = 0.2$ ).

TABLE 4-2

Corresponding Local Times (hr)

<u>Solar Zenith Angle</u>	<u>Dawn Hours</u>	<u>Dusk Hours</u>
60	0821	1539
89	0605	1755
90	0600	1800
92	0551	1809
96	0532	1828

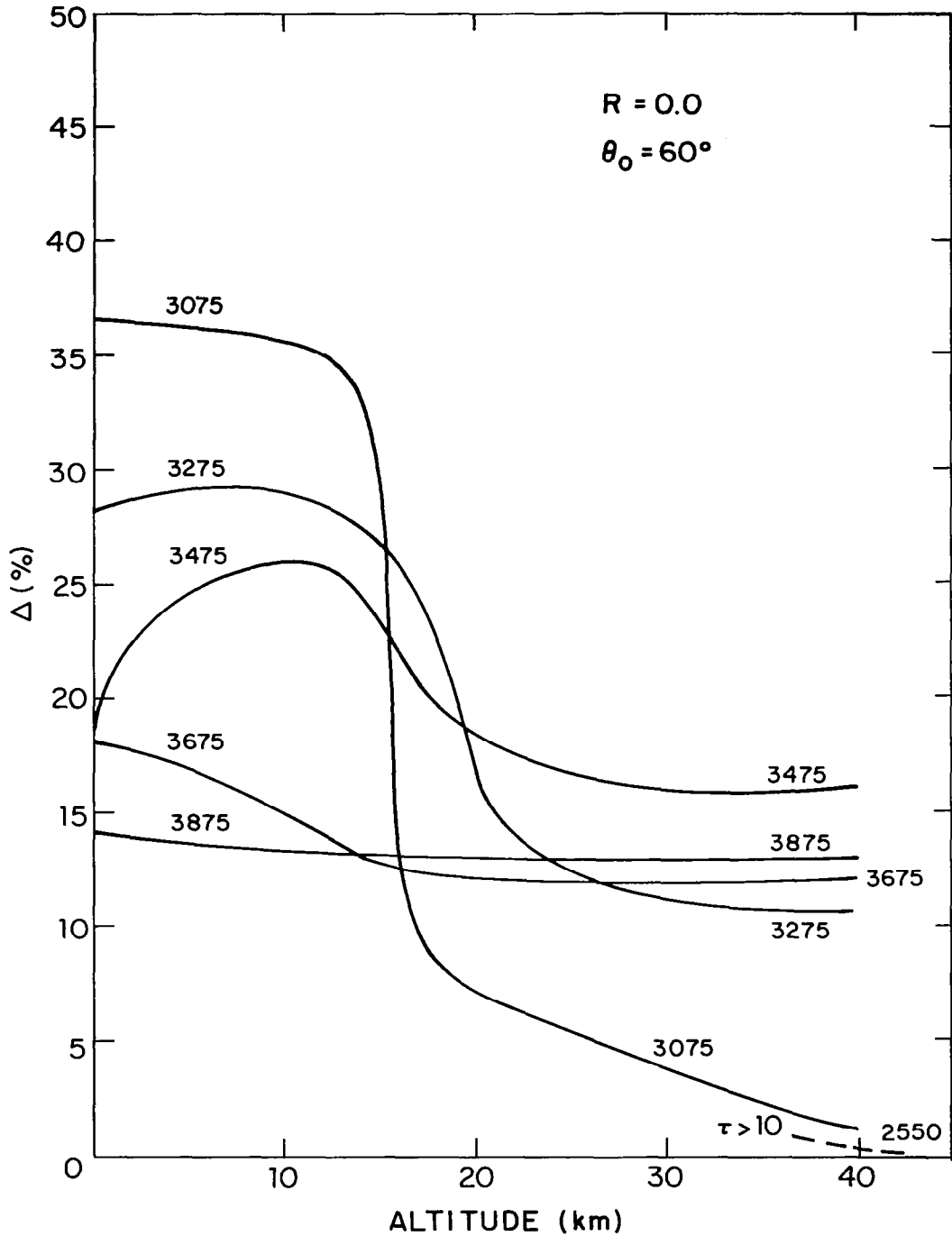


Figure 4-11  
 Percent error profile for single vs multiple scattering at indicated wavelength ( $\theta_0 = 60^\circ$ ,  $R = 0.0$ ).

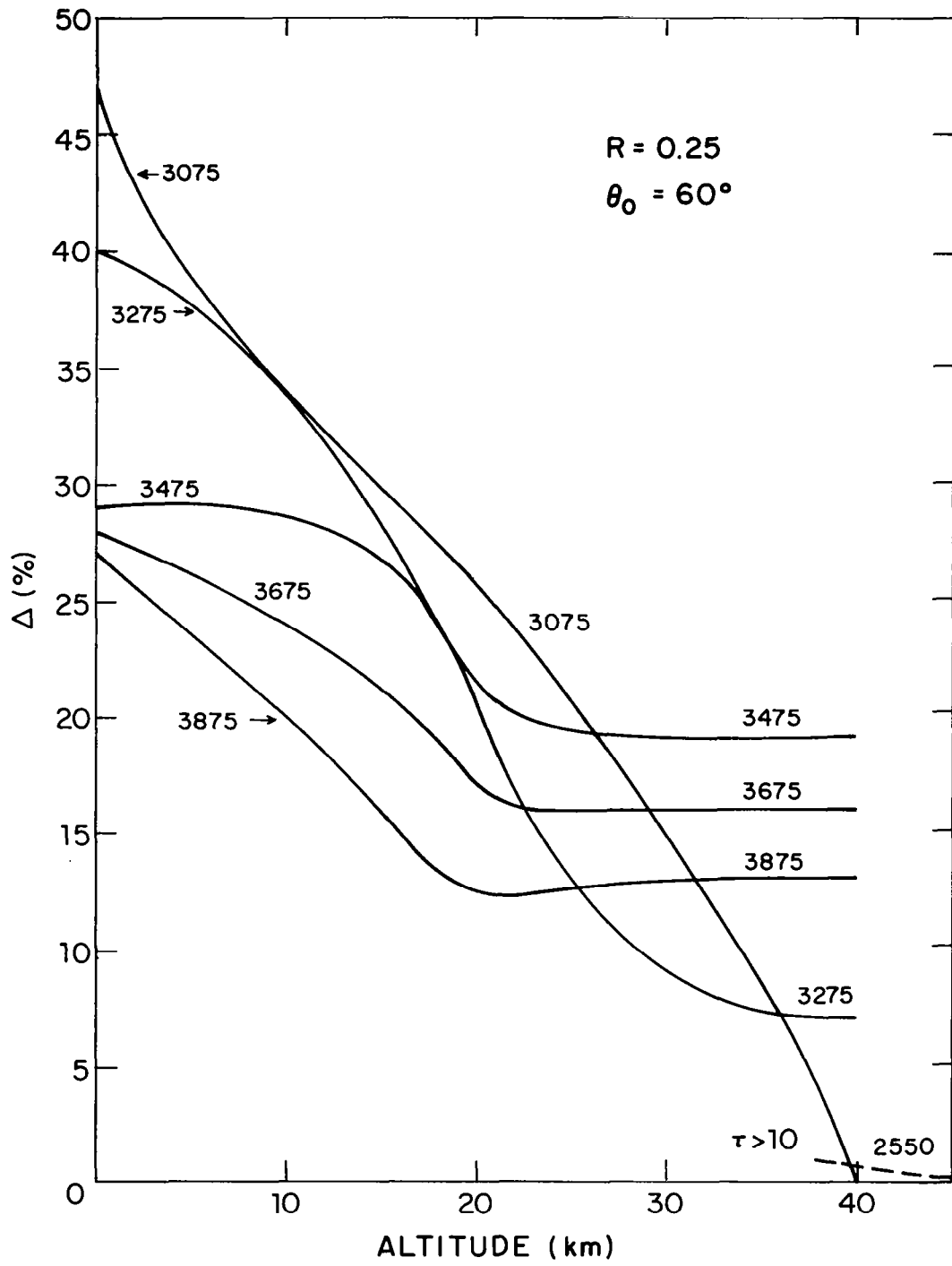


Figure 4-12

Percent error profile for single vs multiple scattering at indicated wavelength ( $\theta_0 = 60^\circ$ ,  $R = 0.25$ ).

$$\Delta(\%) = \frac{F_{MS}^d(z, \theta_0) - F_{SS}^d(z, \theta_0)}{F_{MS}^d(z, \theta_0)} \times 100\% \quad (4-50)$$

It is apparent that accuracies of greater than 25 percent can be obtained (for  $R = 0.25$ ) using a single scattering approach at all wavelengths and at altitudes greater than approximately 20 km. (Errors are enhanced by increasing surface albedo.) This implies that between 70 and 80 percent of the multiply scattered dissociative flux for these cases is due to single scattering alone. Accuracies are best for wavelengths ( $\lambda \leq 3300 \text{ \AA}$ ) where molecular absorption plays a role since single scattering dominates the diffuse flux field. For wavelengths where there is little gaseous absorption ( $\lambda > 3300 \text{ \AA}$ ) accuracies increase as total optical depth decreases.

In the lower atmosphere ( $z \lesssim 20 \text{ km}$ ) where molecular scattering dominates ( $\omega_0 \sim 1.0$ ), errors as high as 40 percent are encountered at shorter wavelengths. This is due to the high attenuation (optical depths  $> 1.0$ ) of the direct solar beam and dominance of the resultant diffuse field. Considering other constraints (such as the presence of clouds) which may limit more sophisticated approaches in the lower atmosphere the accuracy of the single scattering treatment may be deemed acceptable. This approach has been employed in subsequent calculations of diurnally dependent photodissociation rates discussed in §4.5.

#### 4.4.5 Multiple Scattering Results

When accuracies greater than those available from single scattering calculations are required equation (4-45) may be solved by successive orders of scattering (see section 4.4.3). This treatment provides additional insight into the relative role of higher order scattering in

determining the dissociative flux profile.

The dissociative flux due to  $(n + 1)^{\text{th}}$  order scattering is evaluated by generalizing equation (4-47):

$$F_{n+1}^d(\tau) = F_o^d(\tau, \theta_o) + 2 \int_0^{\tau^*} J_n(t) E_1(|\tau-t|) dt \quad (4-51)$$

$$+ 2R E_2(\tau^*-\tau) [\cos\theta_o F_o^d(\tau^*, \theta_o) + 2 \int_0^{\tau^*} J_n(t) E_2(\tau^*-t) dt]$$

where

$$F_o^d(\tau, \theta_o) = FT(\tau, \theta_o) \quad (4-52)$$

and

$$J_n(\tau) = \frac{\omega_o(\tau)}{4} F_n^d(\tau, \theta_o) \quad (4-53)$$

For example, the first order (single) scattering solution [equation (4-48)] corresponds to  $n = 0$ .

Trial calculations based on equation (4-51) are illustrated in Fig. 4-13 for a wavelength of  $3475 \text{ \AA}$ , solar zenith angle of  $60^\circ$  and surface albedo of 0.25. At this wavelength the single scattering albedo profile is near unity throughout the atmosphere (Fig. 4-7) and the total optical depth is about 0.6 (Fig. 4-6). Based on these optical parameters, calculations in this wavelength region represent a worse case situation for multiple scattering, i.e., one where the contributions to the dissociative flux due to multiple scattering are maximum, especially in the lower atmosphere. It is instructive, therefore, to ascertain the order of scattering required to achieve the multiple scattering result for this constraining case and the improved accuracy (with respect to multiple scattering) incurred with each successive order of scattering. Convergence to the multiple scattering solution (within 0.5%)

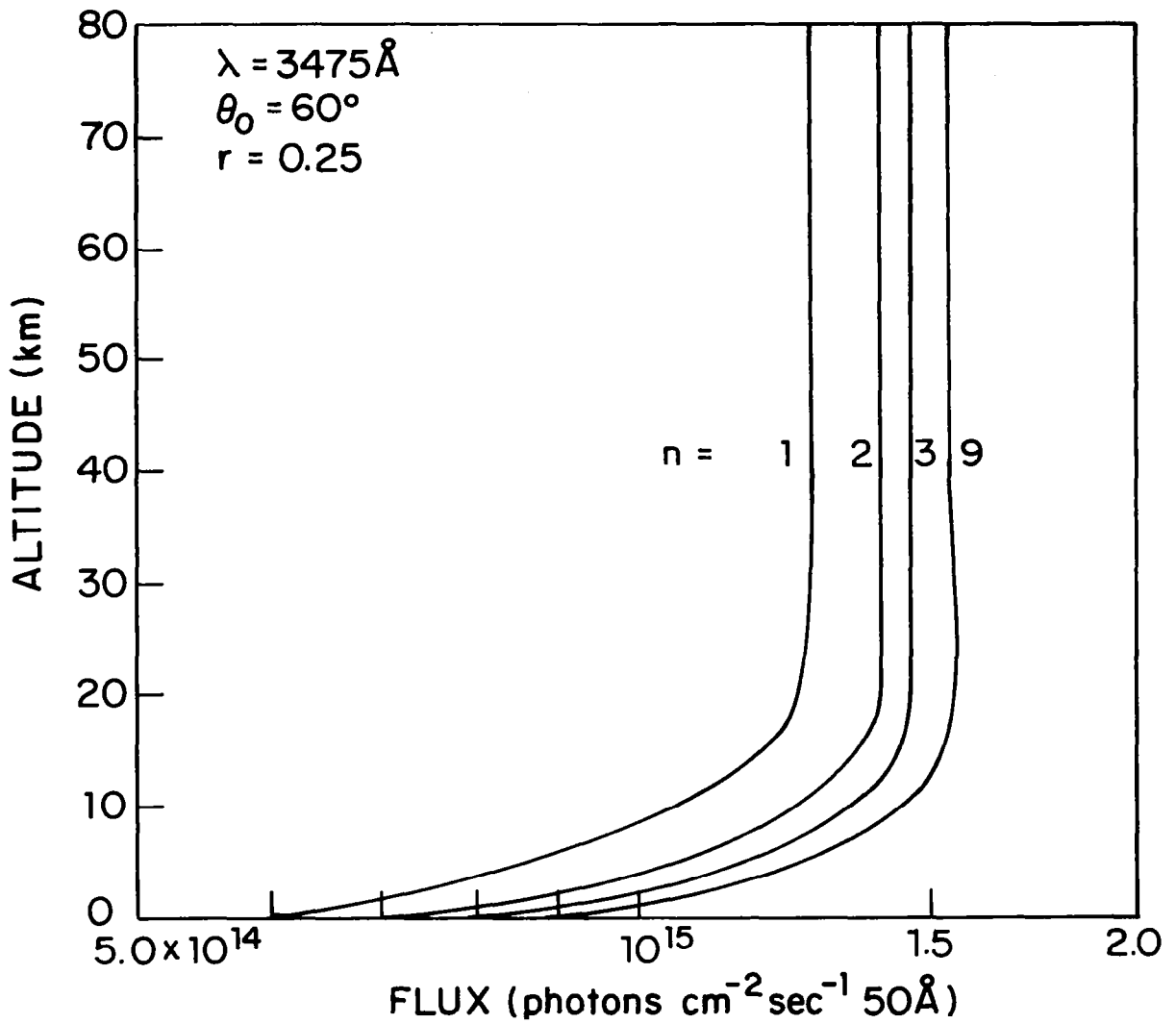


Figure 4-13

Multiply scattered dissociative fluxes by successive orders treatment where  $n$  is the order of scattering ( $\lambda = 3475 \text{ \AA}$ ,  $\theta_0 = 60^\circ$ ,  $R = 0.25$ ).

requires 9 iterations, however, even a second or third iteration drastically improves the result. For the case illustrated as much as 95 percent of the dissociative flux in the upper atmosphere may be attributed to three orders of scattering.

This may be seen explicitly in Fig. 4-14 which illustrates the percent error defined as:

$$\Delta(\%) = \frac{(F_{MS}^d - F_n^d)}{F_{MS}^d} \times 100\% \quad (4-54)$$

as a function of iteration number for a wavelength of 3275 Å at altitudes of 10, 25 and 40 km. To achieve comparable levels of accuracy approximately one more iteration is required in the lower atmosphere (10 km) than in the upper atmosphere. In this example, the single scattering albedo in the lower atmosphere is approximately unity while the mean albedo in the upper atmosphere ( $z > 20$  km) is about 0.5. The total optical depth is closer to unity. As expected based on the previous discussion of the SOS treatment for multiple scattering, convergence to a desired accuracy requires consideration of fewer orders of scattering for albedos less than unity (i.e., above 20 km).

With the methodology for treating multiple scattering formulated in this manner (as a logical extension of the single scattering approach) and the required algorithms in place, comprehensive sensitivity analyses of wavelength dependent dissociative fluxes and photodissociation rates to higher orders of scattering may be undertaken. However, computational costs for each wavelength increase linearly with the order of scattering considered. Due to the finite resources available within the present study, the decision was made to concentrate, therefore, on constraining cases

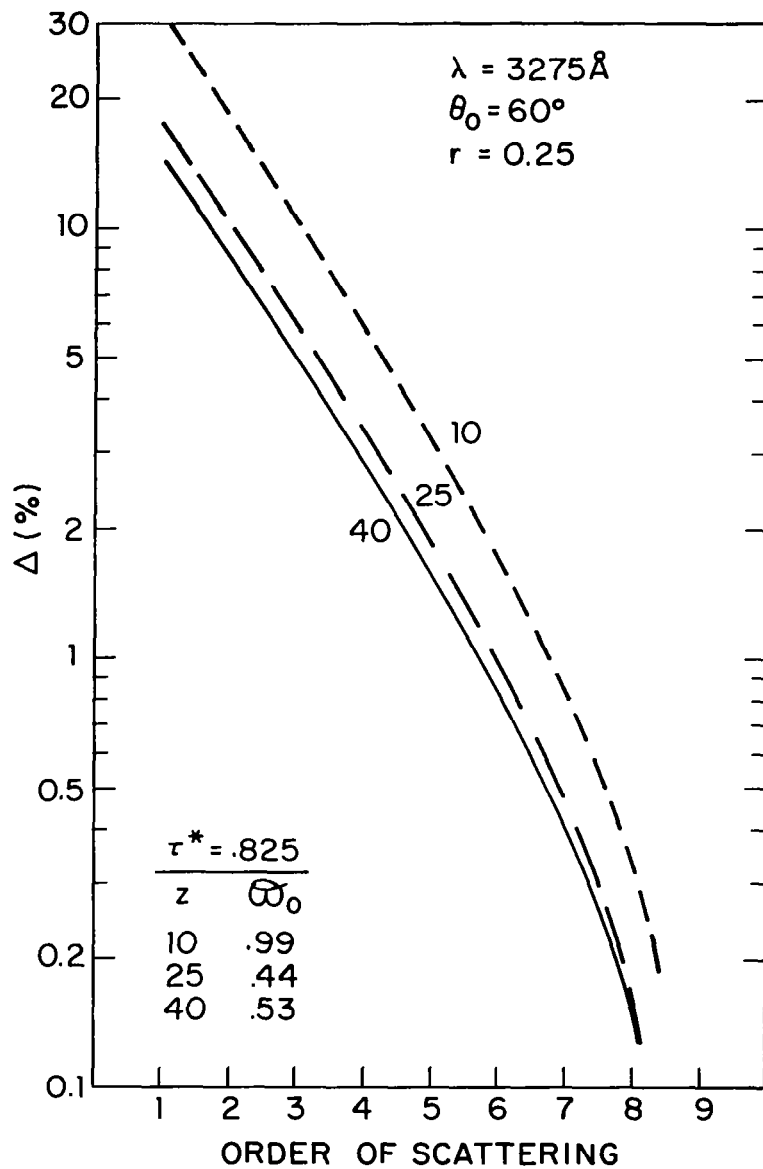


Figure 4-14

Percent error vs multiple scattering result for indicated order of scattering at altitudes of 10, 25, 40km ( $\lambda=3475\text{\AA}$ ,  $\theta_0 = 60^\circ$ ,  $R= 0.25$ ).

such as those described above. For similar reasons, results presented in subsequent sections are based on terminating the multiple scattering code after one iteration. As previously discussed, this insures accuracies in dissociative fluxes on the order of 20-30 percent throughout most of the atmosphere above the tropopause.

#### 4.5 Application to Diurnally Dependent Photodissociation Rates

As a prerequisite to calculation of diurnal variations of radical species in the spherical shell geometry, techniques described above were applied to evaluation of photodissociation rates. Single-scattered dissociative fluxes [equation (4-48)] were computed as a function of wavelength, altitude, and solar zenith angle (time of day) and corresponding dissociation rates were evaluated using equation (4-3) and appropriate cross-section data. Table 4-3 lists the set of dissociative reactions treated in the analysis. For example, Fig. 4-15 illustrates the vertical profile of the ratio of single scattered (SS) dissociation rate to that for pure absorption for reaction 11 in Table 4-3 evaluated at a solar zenith angle of  $45^\circ$  and surface albedo of 0.2. For comparison, multiple scattering (MS) results are presented obtained using a variational approach to solve equation (4-45) (Sze, 1976). Multiple scattering results for a slightly higher surface albedo ( $R = 0.25$ ) are also included (Luther et al. 1978). Results indicate that single scattering accounts for 75-85 percent of the total (i.e., MS) photodissociation rate in the upper atmosphere ( $z > 20$  km).

The difference between plane-parallel and spherical shell geometries is highlighted by examining variation of computed photodissociation rates at times near the local terminator. Figure 4-16 shows the rates for reactions 11 and 20 in Table 4-3 at altitudes of 25 and 40 km near dusk.

TABLE 4-3

## Photolysis Processes

1.  $O_2 + h\nu \rightarrow 2O$
2.  $O_3 + h\nu \rightarrow O(^1D) + O_2$
3.  $O_3 + h\nu \rightarrow O(^3P) + O_2$
4.  $H_2O + h\nu \rightarrow H + OH$
5.  $N_2O + h\nu \rightarrow N_2 + O$
6.  $CH_3Cl + h\nu \rightarrow CH_3 + Cl$
7.  $CFC1_3 + h\nu \rightarrow CFCl_2 + Cl$
8.  $CF_2Cl_2 + h\nu \rightarrow CF_2Cl + Cl$
9.  $CCl_4 + h\nu \rightarrow CCl_3 + Cl$
10.  $HCl + h\nu \rightarrow H + Cl$
11.  $NO_2 + h\nu \rightarrow NO + O$
12.  $NO_3 + h\nu \rightarrow NO + O_2$
13.  $NO_3 + h\nu \rightarrow NO_2 + O$
14.  $N_2O_5 + h\nu \rightarrow NO_3 + NO_2$
15.  $HNO_3 + h\nu \rightarrow OH + NO_2$
16.  $H_2O_2 + h\nu \rightarrow 2OH$
17.  $HO_2 + h\nu \rightarrow H + O_2$
18.  $ClO + h\nu \rightarrow Cl + O$
19.  $HOCl + h\nu \rightarrow OH + Cl$
20.  $ClONO_2 + h\nu \rightarrow ClO + NO_2$

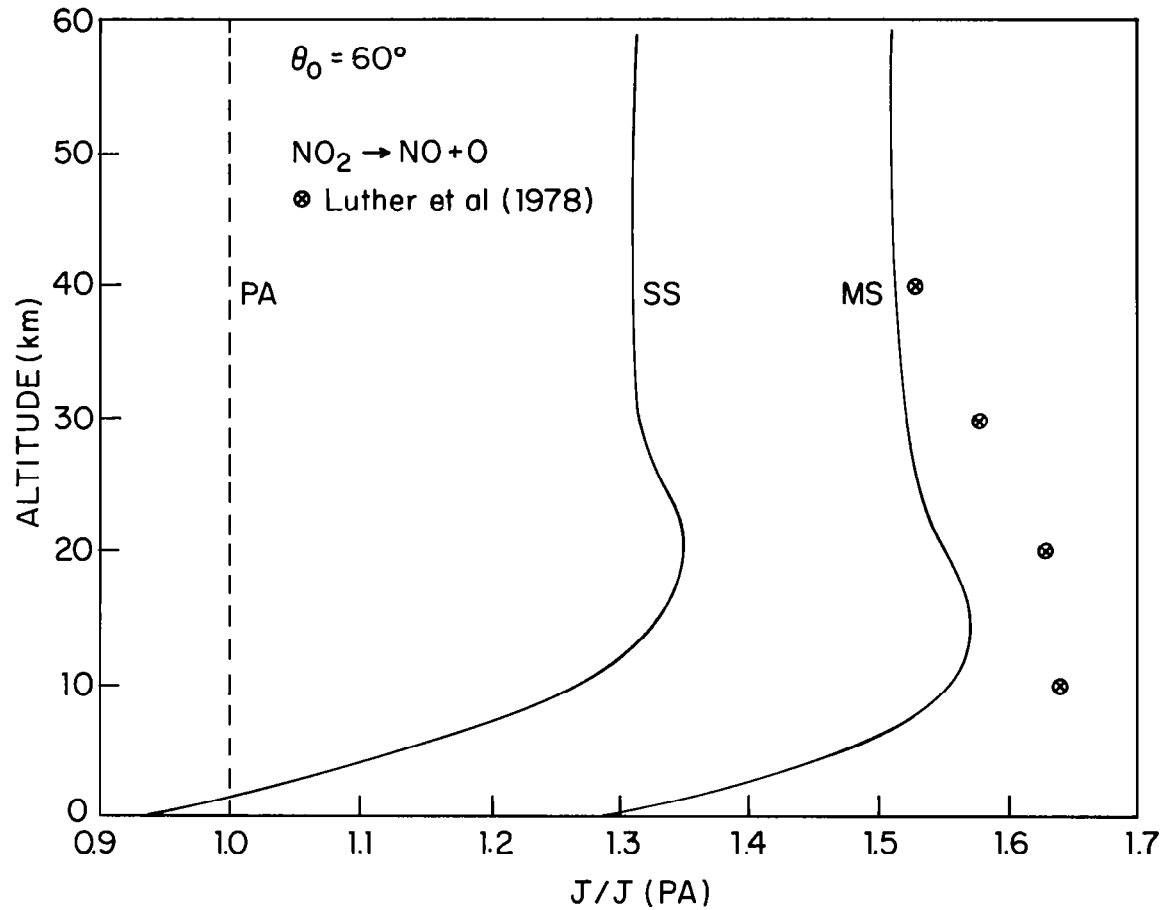


Figure 4-15

Comparison of photodissociation rate for process  $\text{NO}_2 \xrightarrow{h\nu} \text{NO} + \text{O}$  evaluated by successive order treatment truncated after one iteration (i.e., single scattering) to multiple scattering result ( $\theta_0 = 60^\circ$ ,  $R = 0.2$ ).

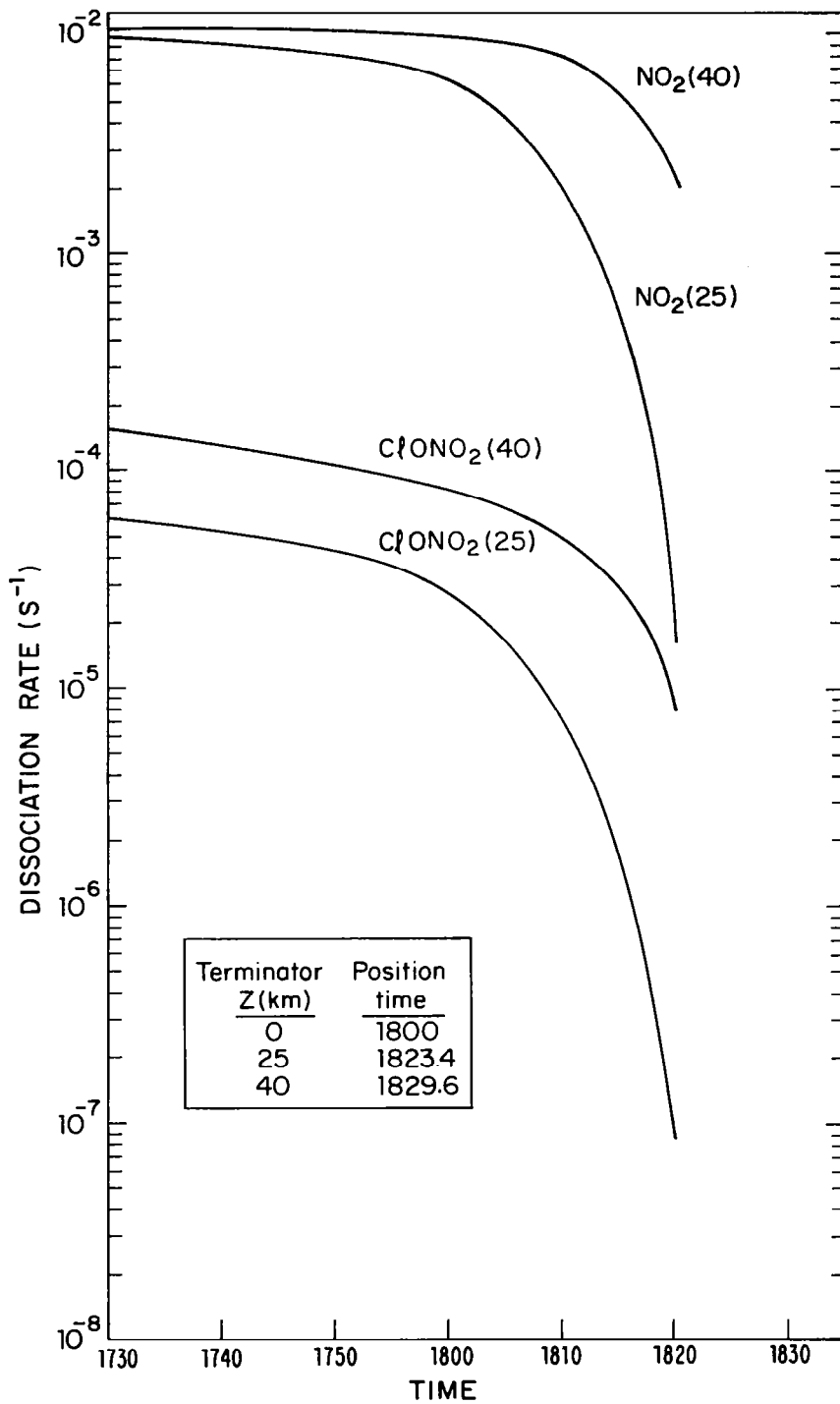


Figure 4-16

Diurnally dependent photodissociation rates for NO<sub>2</sub> and ClONO<sub>2</sub> at z = 25, 40km.

As indicated in the inset, sunset at the surface occurs at 1800 for the case considered (equinox, 30° latitude). In the plane-parallel treatment, photodissociation rates at all altitudes become identically zero at this time. As indicated by the terminator position times for 25 and 40 km (1823.4 and 1829.6, respectively), the first order effect of sphericity at elevations above the surface is to extend the length of the day.<sup>†</sup> This amounts to about 3/4 and 1 hour, respectively, at 25 and 40 km (due to dawn/dusk symmetry).

#### 4.6 Diurnal Calculations

Time dependent altitude profiles of free radical species (e.g., ClO, ClONO<sub>2</sub>, HCl, H<sub>2</sub>O<sub>2</sub>, HO<sub>2</sub>, OH, NO, NO<sub>2</sub>) were obtained by performing diurnal calculations using numerical procedures described in Appendix D. Photodissociation rates used in the diurnal simulations included: (a) molecular scattering effects, (b) surface reflection (a surface albedo of 0.2 was used throughout the wavelength region) and (c) consideration of the spherical shell geometry of the Earth's atmosphere. Treatment of these factors has been discussed in previous sections. Single scattered dissociative fluxes were employed as a first order treated. As noted above (§4.5) this approximation accounts for the bulk of molecular scattering within the wavelength interval. In conducting the diurnal calculations, long-lived species (such as N<sub>2</sub>O, O<sub>3</sub>, CH<sub>4</sub>, etc.) were held fixed and vertical transport was neglected.

Figures 4-17a and b illustrate time dependent results for ClONO<sub>2</sub>, OH, NO<sub>2</sub>, ClO and HO<sub>2</sub>. An altitude of 40 km was chosen for demonstration purposes. The solid species

---

<sup>†</sup>These times neglect refraction.

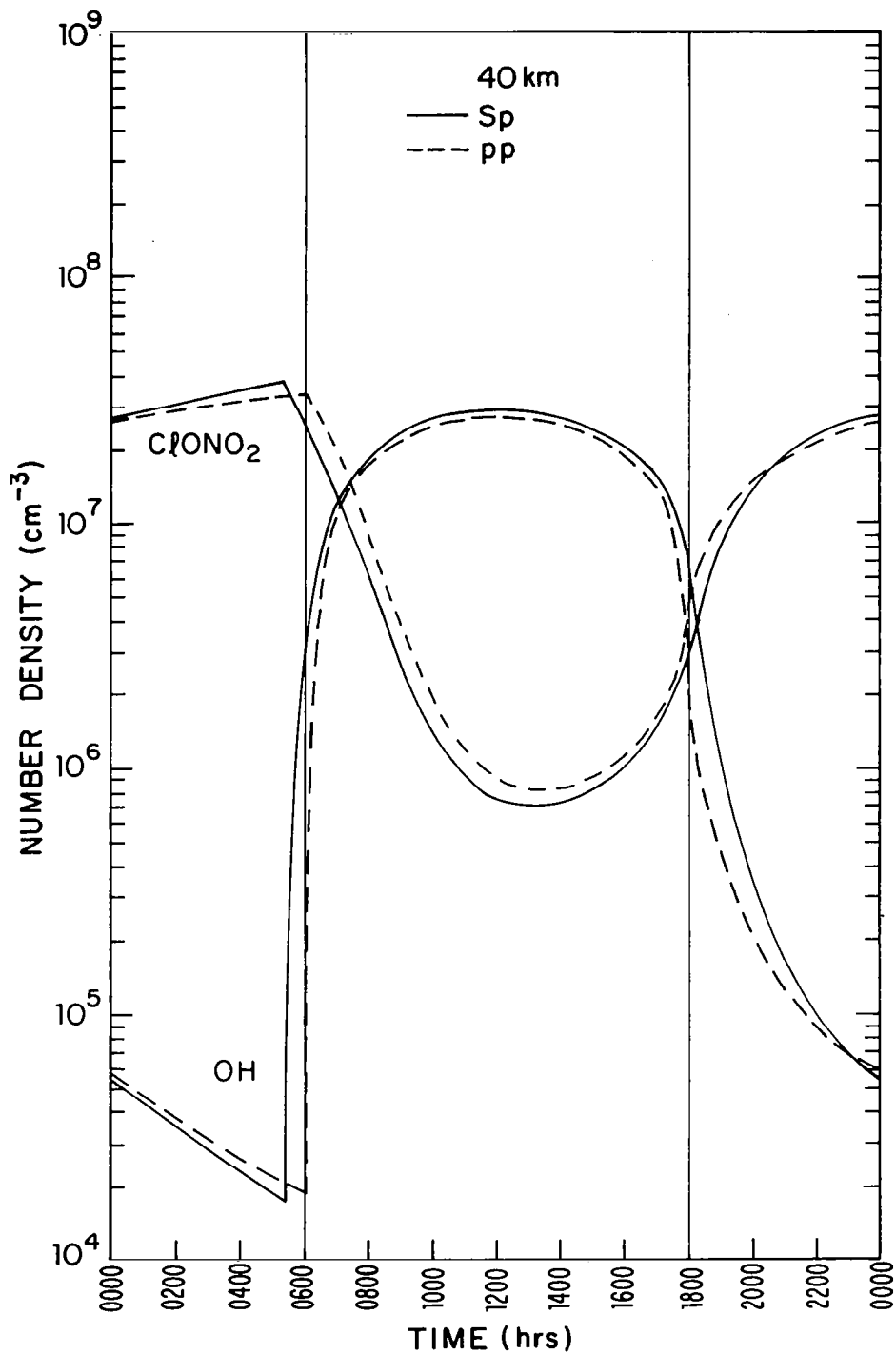


Figure 4-17a

Comparison of diurnal variation of ClONO<sub>2</sub> and OH using absorption only-plane parallel treatment (dotted) and scattering-spherical treatment (full) at z = 40km.

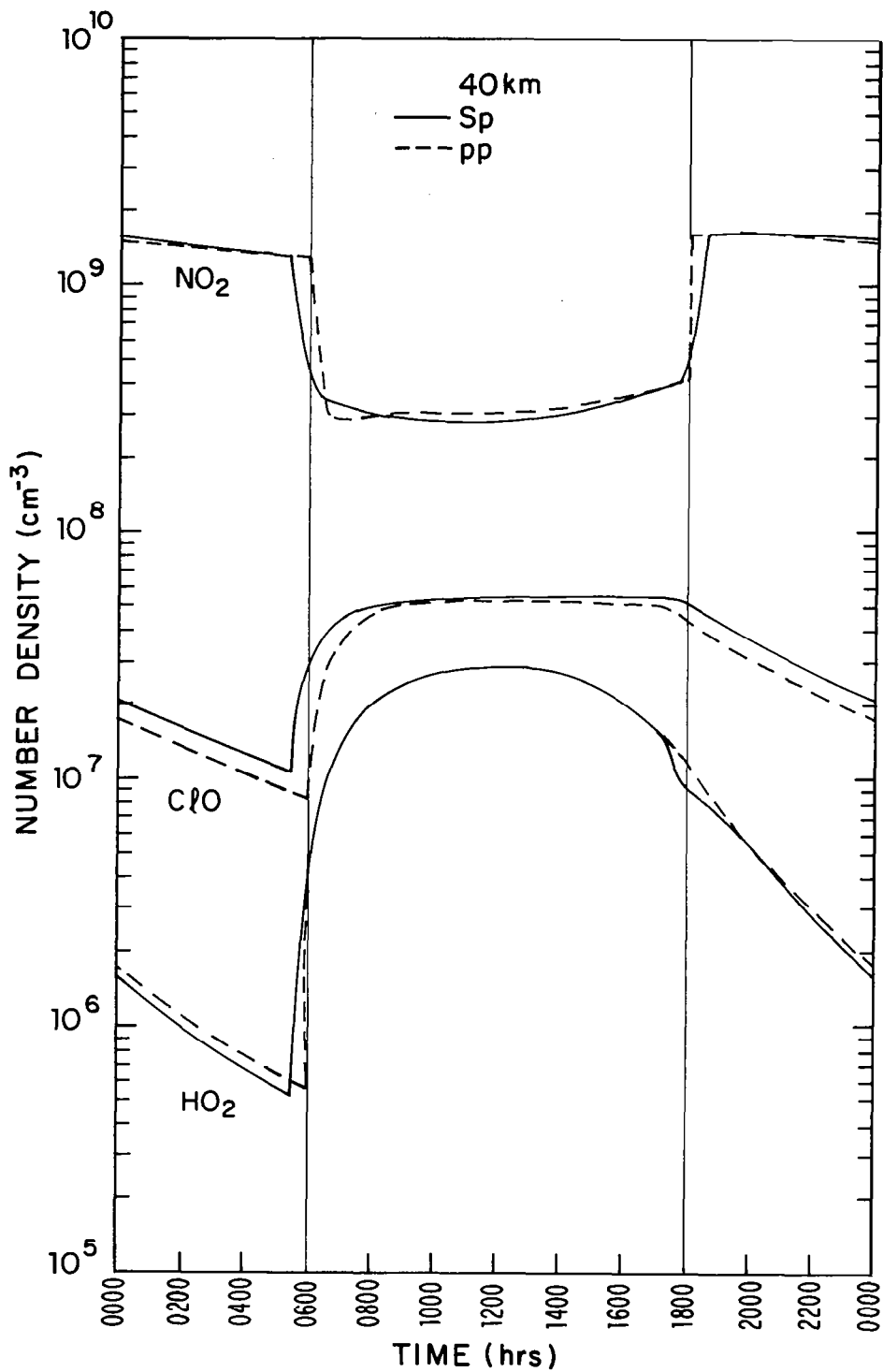


Figure 4-17b

Comparison of diurnal variation of NO<sub>2</sub>, ClO, and HO<sub>2</sub> using absorption only-plane parallel treatment (dotted) and scattering-spherical treatment (full) at  $z = 40\text{km}$ .

abundance curves refer to the spherical shell (Sp), single scattering result. For comparison, plane-parallel (PP), pure absorption results (dotted curves) are also provided. The time scale refers to local time at equinox and 30° north latitude. Times of dawn (0600) and dusk (1800) at the surface ( $z=0$  km)<sup>†</sup> are indicated by light vertical lines.

#### 4.6.1 Role of Sphericity

Comparing the two sets of results, the gross effect of sphericity on the diurnal variation of free radical abundances is to accelerate the onset of photochemical production (of OH, ClO and HO<sub>2</sub>) and loss (of ClONO<sub>2</sub> and NO<sub>2</sub>) at dawn and delay termination of these processes at dusk by approximately one-half hour. Thus, at 40 km sphericity effectively increases the length of the day by about an hour (neglecting refraction). Since many photolysis processes have time constants of seconds to minutes, specification of precise local dawn and dusk (i.e., at altitude) is of considerable interest for determining the transition times between daytime and nighttime chemistries.

As a consequence of these "phase" lags, the plane-parallel approach may seriously miscalculate abundances of photochemically active species in the dawn/dusk transition period. A case in point is the dawn OH concentration (Fig. 4-17a). In the plane-parallel treatment this is a nighttime value, however, when Earth curvature is considered the atmosphere at this time is already about one-half into daylight and the corresponding OH concentration is two orders of magnitude higher. The result is not as striking for ClO (Fig. 4-17b) whose major source (photolysis of

---

<sup>†</sup>Or at all altitudes in the plane-parallel approximation.

ClONO<sub>2</sub>) has a longer lifetime.

Several gross features of the diurnal variation of those species illustrated in the figures are worth noting. These include: (a) the marked difference between daytime and nighttime species abundances alluded to above (sometimes varying by orders of magnitude), (b) the relatively slow variation of concentrations with time during mid-day and nighttime hours, (c) the contrasting rapid variation during the post-dawn/dusk transition periods and (d) the absence of symmetry about local noon (1200 hr).

These properties may be understood by considering the dependence of modeled abundances on the presence of key photolysis processes during the day, their absence at night, and the rapid variation of the primary source of dissociative flux (the Sun) during dawn/dusk transitional periods. The relative constancy of concentrations near midday validates the uses of steady state simulation approaches for many applications. One aspect which may not be immediately intuitive is the daily asymmetry with respect to noontime values. Although photodissociation rates (which to first order are functions of solar zenith angle only) are symmetric about noon, photolysis processes must compete with other production and loss mechanisms which do not necessarily "follow the Sun". Post-dawn and post-dusk time dependence is characteristic of the locally dominant chemistry and thus, distinctive time constants contribute to the post-dusk apparent log linear behavior. The attributes discussed above with respect to Figures 4-17a,b are evidently dependent on the particular species under discussion, however, additional calculations indicate that they also depend on altitude.

#### 4.6.2 Role of Molecular Scattering

The near noontime values shown in Figs. 4-17a and b

provide a calibration point on the relative role of scattering. For these times of day, the present calculations reduce to the plane-parallel case and the only difference between solid and dotted curves is the treatment of first order scattering in the former case. As illustrated, the difference between the two calculations is not appreciable. However, the magnitude and sign of the concentration difference near noon is consistent with other calculations of the effect of multiple scattering (Luther et al. 1978). At this altitude (40 km) consideration of scattering appears to be of minor consequence, however, additional calculations indicate that the effect is appreciable at lower altitudes. This behavior is understandable upon examination of individual contributions to the relevant dissociative fluxes (see Figs. 4-8, 4-9; §4.4.4). They suggest that the attenuated direct solar beam dominates in the upper atmosphere while diffuse contributions become progressively more important toward the troposphere (i.e., within 2-3 pressure scale heights of the surface).

#### 4.7 Implications for Remote Sensing

Previous sections have described a methodology for including the effects of Earth curvature and molecular scattering in the simulation of diurnally dependent free radical species concentrations. Ultimately, the utility of extensions to existing theory may be evaluated based on their application to either the interpretation of new measurements or existing data inconsistent with previous theory. In this section implications of the work described above are discussed with reference to emerging measurement techniques based on remote sensing.

Historically, most relevant species profile data have been collected during daylight hours. This choice is

based in part on logistical constraints and in part to take advantage of the relative constancy of species concentrations during mid-day. Such data sets obviate the need for other than steady state modeling for most practical purposes.

Requirements for global monitoring of stratospheric trace species have motivated recent developments in remote sensing technology including use of the solar occultation approach (Russell and Drayson, 1972; Russell et al., 1977; Chu and McCormick, 1979; Menzies, 1979). An inherent characteristic of the experimental configuration in this technique is a sensor field of view with line of sight integrating across the terminator. As illustrated in the previous section, the number densities of photochemically active species may vary by orders of magnitude during dawn and dusk. It is evident from these results that since there is such a radical time rate of change, photochemical equilibrium (i.e., steady state) models may introduce uncertainties in the interpretation of data obtained by such techniques.

In principal, most inversion methods for obtaining vertical species profiles from occultation data such as analytical treatments (Roble and Hays, 1972) and the onion peel approach (McKee et al., 1969) rely on the assumption of spherical symmetry and stratification in the distribution of the relevant absorbers. Since lines of sight in the occultation mode essentially look through varying local times and altitudes, this requires that observed species are time invariants (i.e., depend on altitude only). The gross features of the diurnal calculations described in §5.6 suggest that this is not true for many radical species. Qualitatively, it is expected that inversion results based on spherical symmetry considerations will be least affected for individual species with suppressed

diurnal variations (such as ClO as contrasted with OH or NO). Furthermore, the character of the dawn/dusk asymmetries noted previously suggest that, due to the generally more rapid variation of photochemically active species in the post-dawn transition period, reduced accuracies may be expected for dawn occultation as compared to dusk occultations. These assessments are generally confirmed by recent simulations of inversions (Boughner et al., 1980).

Based on these considerations it may be useful to investigate approaches to incorporating a priori information on diurnal variations within the inversion algorithm. In this context the occultation techniques can be outlined as follows. The radiation of wavelength  $\lambda$  received at the sensor for a line of sight  $s$  with tangent height  $z_0$  (see Fig. 4-1) will be given by the solution to (4-36):

$$I_{\lambda}[s(z_0)] = I_{\lambda}(\infty)T_{\lambda}[s(z_0)] + \int_0^{s(z_0)} J_{\lambda}(s')dT_{\lambda}(s') \quad (4-55)$$

where  $I_{\lambda}(\infty)$  is the unattenuated solar radiance,  $T_{\lambda}$  is the transmission function along the line of sight equation (4-8), and  $J$  is the local source function [determinable from equation (4-45)]. If scattering can be ignored, this reduces to:

$$I[s(z_0)] = I(\infty)T[s(z_0)] \quad (4-56)$$

where [in analogy to equation (4-9)]:

$$T = \exp - \sum_{i=1}^K \sigma^i \int_0^{s(z_0)} n^i(s')ds' \quad (4-57)$$

Ignoring refraction, the line integral can be written in terms of altitude noting from the geometry:

$$\begin{aligned}
 ds(z_0, z') &= (z' + R)[z' + R]^2 + (z_0 + R)^2]^{-\frac{1}{2}} dz' \\
 &= G(z_0, z') dz'
 \end{aligned}
 \tag{4-58}$$

yielding

$$\tau(z_0) = \ln \left[ \frac{I(\infty)}{I(z_0)} \right] = 2 \sum_{i=1}^K \sigma^i \int_{z_0}^{\infty} n^i(z') G(z_0, z') dz' \tag{4-59}$$

This expression assumes that the relevant absorber is a function of altitude only (i.e, spherically symmetric) and is amenable to inversion by one of the techniques described above.

Diurnal simulation provide an understanding of the true variation of photochemically active absorbers along the line of sight. Figs. 4-17a,b, for example, essentially indicate:

$$n(s') = n[z', \theta(t)] \tag{4-60}$$

where  $\theta$  is the local solar zenith angle given by:

$$\theta = \sin^{-1} [(R + z_0)/(R + z')] \tag{4-61a}$$

on the solar side of the path and

$$\theta = \pi - \sin^{-1} [(R + z_0)/(R + z')] \tag{4-61b}$$

on the anti-solar side where  $\theta = \pi/2$  denotes the terminator. Noting diurnal variations equation (4-59) may be generalized as:

$$\tau(z_0) = \sum_{i=1}^K \sigma^i \int_{z_0}^{\infty} [n^i(z', \theta) + n^i(z', \pi - \theta)] G(z_0, z') dz' \tag{4-62}$$

A form analogous to equation (4-59) is obtainable by introducing a shape function describing the spherical asymmetry obtainable from diurnal simulations (Boughner et al., 1980):

$$D^i(z_o, z') = \left[ \frac{n^i(z', \theta) + n^i(z', \pi - \theta)}{2n^i(z', \pi/2)} \right] \quad (4-63)$$

yielding:

$$\tau(z_o) = \sum_{i=1}^K \sigma^i \int_{z_o}^{\infty} n^i(z', \pi/2) K^i(z_o, z') dz' \quad (4-64)$$

where the kernel is:

$$K^i(z_o, z') = D^i(z_o, z') G(z_o, z') \quad (4-65)$$

For time invariant species  $D^i = 1$  and equation (4-64) reduces to the spherically symmetric case.

Equation (4-64) is a Fredholm equation of the first kind defined generally as:

$$h(y) = \int_a^b K(x, y) f(x) dx \quad (4-66)$$

where  $h(y)$  represents the data and  $f(x)$  the desired function. In operator form equation (4-66) may be written as:

$$Kf = g \quad (4-67)$$

In this form a number of powerful generalized inverse techniques such as Phillips (1962) and Twomey (1950) are applicable which do not assume spherical symmetry. Furthermore, questions regarding uncertainties introduced in simulating the required kernel function equation (4-63) and other typical sources of noise such as those introduced in linearization and quadrature of equation (4-64) may be

addressed by examining optimal smoothing parameters,  
selecting suitable regularization functions, and employing  
appropriate inversion constraints (such as non-negativity).

## 5. SUMMARY AND RECOMMENDATIONS

This section summarizes some of the major findings of the tasks described in the previous sections. The reader is referred to the individual sections for more detailed description of results.

### 5.1 Model Sensitivity Studies

As discussed in Section 2 the results of 1-D model simulated ozone perturbations to high altitude aircraft operations are subject to major uncertainties particularly as regards rate constant data related to OH chemistry. Sensitivity studies indicate that calculated OH concentration profiles are most sensitive to values adopted for the reactions listed in Table 2-1. Perturbation calculations were performed for three model scenarios corresponding to high (model A) and low (models B and C) values of stratospheric OH concentration. Model C investigates the potential role of peroxyntic acid ( $\text{HO}_2\text{NO}_2$ ) as a sink for OH and provides indicators of OH concentration (e.g.,  $\text{ClO}$ ,  $\text{HNO}_3/\text{NO}_2$ ,  $\text{HF}/\text{HCl}$ ) in best agreement with measurements. Model A tends to predict an increase in column ozone for both low (15 km) and high (20 km)  $\text{NO}_x$  injections. The low OH models (B and C), however, predict a small (<1%) increase for the low altitude injection, but a fairly significant reduction for the high altitude case (-5.5%, model C). More reliable kinetic data is needed to differentiate between the models discussed.

Additionally, it is noted that injection of  $\text{NO}_x$  may perturb both local stratospheric and surface temperatures. Thus, climatic changes should be considered in addition to column ozone perturbations.

## 5.2 Two-Dimensional Zonal-Mean Modeling

The application of Eulerian averaging processes to zonal-mean models introduces a number of undesirable features associated with the eddy flux contributions to transport. The feasibility of some kind of Lagrangian approach as an alternative averaging methodology is attractive from the standpoint that eddy terms are avoided. However, difficulties arise in the implementation of the formulation and in interpretation of mixing ratio results in comparison with observations. Several areas are identified for additional research before the Generalized Lagrangian Mean (GLM) tracer equation may be applied to zonal modeling.

In the short term, numerical tracer experiments comparing Eulerian and GLM approaches may be performed deriving the required Lagrangian velocity components for given three-dimensional motion fields. One potential avenue for research would concentrate on cases with small disturbances using a more precise treatment of the diabatic heating rate to generate Lagrangian velocity fields.

Longer term research may be profitably directed to examining the interpretation of the basic continuity equation and in reformulating the momentum equation by defining more generalized differential operators.

## 5.3 Remote Sensing

The role of multiple scattering and Earth sphericity on the calculation of diurnally dependent photodissociation rates and trace species concentrations was examined in Section 4 with particular emphasis on dawn and dusk.

Calculations of slant path air mass factors indicated that sphericity should be considered in evaluating the primary source function for scattering for solar zenith angles greater than about  $80^\circ$ . Evaluation of profiles of

atmospheric optical depth and single scatter albedo at dissociative wavelengths suggested that a successive order of scattering (SOS) approach may be viable at all altitudes. A locally plane-parallel (LPP) treatment of the radiative transfer equation was adopted to treat the spherical geometry. Comparison of single scattered dissociative flux profiles with multiple scattering results indicated that between 70 and 80 percent of multiply scattered flux above 20 km can be accounted for by single scattering alone. In the lower atmosphere where molecular scattering dominates errors as high as 40 percent are encountered, however, accuracies comparable to those in the upper atmosphere can be achieved by considering an additional order of scattering. Convergence to the multiple scattering result (within 0.5%) requires about 9 orders of scattering, however, 5 percent accuracy is available in the upper (lower) atmosphere with only 3 (4) orders. Diurnal calculations of trace species indicate that the gross effect of sphericity on diurnal variation is to accelerate the onset of photolytic processes at "plane-parallel" dawn and delay their termination at "plane-parallel" dusk.

Based on the results of diurnal trace species variation across the terminator region, it is recommended that a potential approach to the inversion problem in the occultation geometry may be consideration of generalized inverse techniques not relying on assumptions of spherical symmetry. In this manner the shape of the kernel function may be estimated to first order using a priori calculations of diurnal trace species concentrations.

## APPENDIX A

### Earth-Sun Geometry

As in the plane-parallel case, the transmission path for solar radiation incident at a specified altitude,  $z$  (km), will be a function of the local solar zenith angle,  $\theta_0$ . The solar zenith angle may be defined from the scalar product of the local surface normal vector,  $\hat{n}$ , and the Sun's direction vector,  $\hat{s}$ . In a celestial coordinate system with origin fixed at the Earth's center, the unit normal vector will be a function of latitude,  $\lambda$ , and local hour angle, HA. The unit solar direction vector,  $\hat{s}$ , will depend on the Sun's declination angle,  $\delta$ . The required relationship between solar zenith angle, latitude, solar declination angle and hour angle is given by:

$$\cos\theta_0 = \sin\delta \sin\lambda + \cos\delta \cos\lambda \cos\text{HA} \quad (\text{A-1})$$

Solar declination angle,  $\delta$ , may be approximated as:

$$\sin\delta = 0.3978 \sin[.9863(d-80)] \quad (\text{A-2})$$

where  $d$  is the day of the year (1 Jan. = 1, 20 Mar. = 80, etc.). Note that  $\delta$  is zero at the equinoxes, and has maxima  $|\delta| = 23^\circ 27'$  at the solstices.

The hour angle, HA, is defined as identically zero at local noon, 1200h, (Sun's direction vector along observer's meridian) when the Sun's zenith angle is smallest:

$$\cos\theta_0(1200) = \sin\delta \sin\lambda + \cos\delta \cos\lambda \quad (\text{A-3})$$

Conversely, sunrise and sunset times may be defined as corresponding to solar zenith angles of  $90^\circ$ . The length of the day in hours is then given by:

$$\text{LOD} = \frac{2}{15} \cos^{-1}[-\tan\delta \tan\lambda] \quad (\text{A-4})$$

Thus hour angle may be written as:

$$HA(\text{deg}) = 15(12.00-t) + \epsilon \quad (\text{A-5})$$

where 15 is the Earth's angular rotation rate ( $^{\circ}\text{h}^{-1}$ ) and  $\epsilon$  is a correction for the equation of time. Equations (A-1), (A-2) and (A-5) define a solar zenith angle for a given date, time, and latitude.

Additionally, the local normal,  $\hat{n}$ , and the Sun's direction vector,  $\hat{s}$ , define a plane of incidence pictured in Fig. (A-1). This plane contains the subsolar point (SSP) where the solar zenith angle is zero and the required local normal vector,  $\hat{n}$ . For solar zenith angles which are sufficiently small (say  $\theta_0 < 80^{\circ}$ ), a plane-parallel treatment will suffice. For situations near sunrise and sunset, however, the Earth's sphericity is a critical consideration. Figure (A-1) illustrates a number of relevant cases. Local normal  $\hat{n}_1$  denotes a situation with  $\theta_0$  approaching  $90^{\circ}$ . In this case the usual plane parallel treatment ( $\sec\theta_0$ ) will overestimate the relevant optical path. As illustrated by local normal  $\hat{n}_2$ , the solar zenith angle  $\theta'_0$  may be  $>90^{\circ}$  at elevations above the surface. For these situations the upper atmosphere may be illuminated while the lower atmosphere is not. The shadow height will be given by:

$$\begin{aligned} Z_s &= R(\csc\theta_0 - 1) \\ &= R(\sec U - 1) \end{aligned} \quad (\text{A-6})$$

where U is the solar depression angle defined as:

$$\theta_0(>90^{\circ}) = 90^{\circ} + U \quad (\text{A-7})$$

and R is the Earth's radius ( $6371 \times 10^3 \text{m}$ ). Thus for  $U = 8^{\circ}$  sunrise occurs at an altitude of  $62.6 \times 10^3 \text{m}$ . This corresponds to about 0523 local time at equinox at  $30^{\circ}\text{N}$ . [These calculations and equation (A-6) ignore refractive effects which decrease  $Z_s$ .]

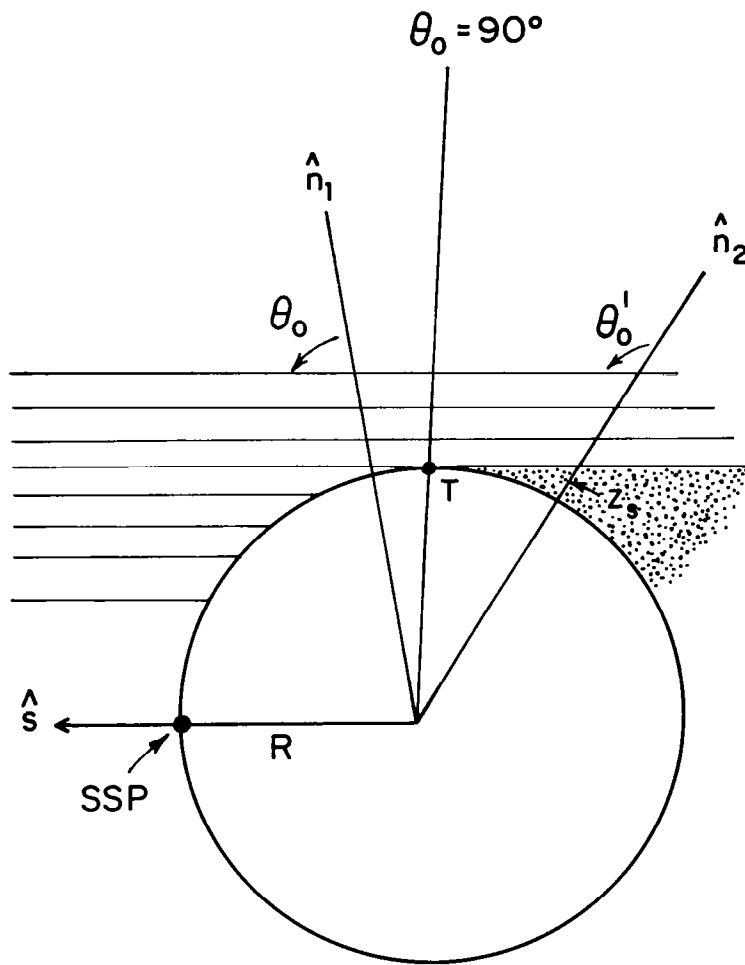


Figure A-1  
 Earth-Sun Geometry.

## APPENDIX B

### Procedure for Refracted Air Mass Calculation

Calculations follow a procedure based on Selby and McClatchey (1972). Essentially, equation (4-22) is modified by a factor dependent on the phase refractive index of air,  $\tilde{m}(z)$  with the resultant air mass factor given by:

$$M_{Sp}^4(z, \theta_o) = \frac{1}{n^i(z) H_z} \int_z^\infty n^i(z') \left\{ 1 - \left[ \frac{(R+z)\tilde{m}(z)}{(R+z')\tilde{m}(z')} \right]^2 \sin^2 \theta_o \right\}^{-\frac{1}{2}} dz' \quad (B-1)$$

The phase refractive index of air  $\tilde{m}(z)$  is given by Edlen's (1966) expression:

$$[\tilde{m}(z) - 1.0] \times 10^6 = (77.6 + \frac{.0459}{\lambda^2}) \frac{P(z)}{T(z)} - P_{H_2O} (43.49 - \frac{0.347}{\lambda^2}) \quad (B-2)$$

where  $\lambda$  = wavelength in microns ( $\mu\text{m} = 10^3 \text{nm}$ )  
 $P$  = pressure (atm = 101.325 kPa)  
 $T$  = temperature (K)

$P_{H_2O}$  = partial pressure of water vapor (atm = 101.325 kPa)

The geometry of the refraction calculation is illustrated in Fig. (B-1). Following Selby and McClatchey (1972), the path integral is performed using the local solar zenith angle as the integration variable. For initial solar zenith angle  $\theta_{j+1}$  incident on level  $z_{j+1}$ , geometry yields:

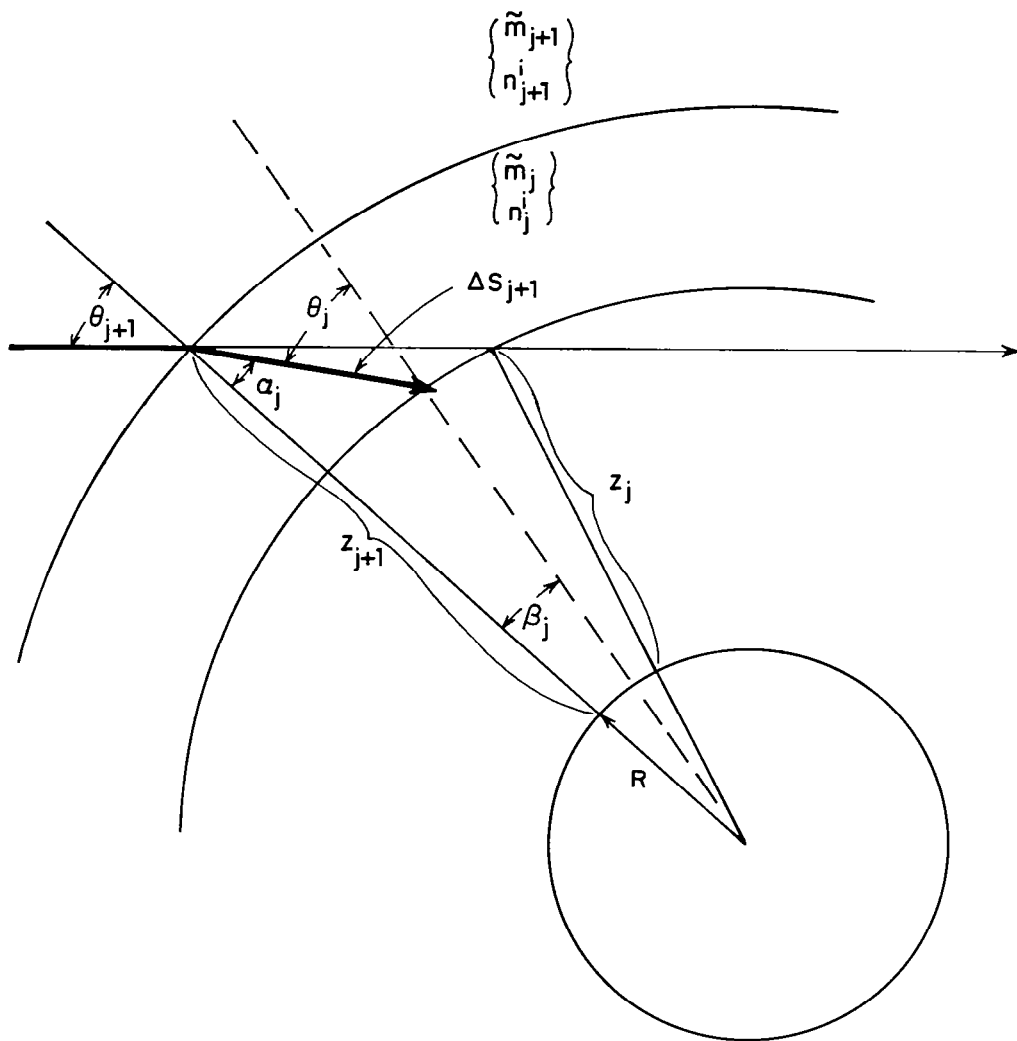


Figure B-1  
 Geometry of refraction calculation.

$$\frac{R+z_{j+1}}{\sin\theta_j} = \frac{R+z_j}{\sin\alpha_j} \quad (\text{B-3})$$

From Snell's law:

$$\sin\alpha_j = \frac{\tilde{m}_{j+1}}{\tilde{m}_j} \sin\theta_{j+1} \quad (\text{B-4})$$

The incidence angle on the next level is obtainable from equations (B-3) and (B-4):

$$\sin\theta_j = \frac{(R+z_{j+1})}{(R+z_j)} \frac{\tilde{m}_{j+1}}{\tilde{m}_j} \sin\theta_{j+1} \quad (\text{B-5})$$

or

$$\tilde{m} \sin\theta (R+z) = \text{const} \quad (\text{B-6})$$

The increment of path length in the layer from  $z_j$  to  $z_{j+1}$  is given by:

$$\Delta s_{j+1} = (R+z_{j+1}) \frac{\sin\beta_j}{\sin\theta_j} \quad (\text{B-7})$$

where  $\beta_j$  is given by:

$$\beta_j = \theta_j - \alpha_j \quad (\text{B-8})$$

Substitution of equations (B-4), (B-5) and (B-8) into (B-7) yields:

$$\Delta s_{j+1} = \frac{(R+z_{j+1})}{\sin\theta_j} \sin \left\{ \sin^{-1} \left[ \frac{(R+z_{j+1})}{(R+z_j)} \frac{\tilde{m}_{j+1}}{\tilde{m}_j} \sin\theta_{j+1} \right] - \sin^{-1} \left[ \frac{\tilde{m}_{j+1}}{\tilde{m}_j} \sin\theta_{j+1} \right] \right\} \quad (\text{B-9})$$

APPENDIX C

Integral Quadrature Technique

Evaluation of expression (4-48) for single scattering and the general successive order of scattering relation (4-31) require calculation of integrals of the form:

$$I_n(\tau, \tau^*) = \int_0^{\tau^*} E_n(|t-\tau|) f(t) dt \quad (C-1)$$

where the  $n^{\text{th}}$  exponential integral is given by:

$$E_n(x) = \int_0^1 e^{-x/\mu} \mu^{n-2} d\mu \quad (C-2)$$

The first three exponential integrals are illustrated in Figure C-1. These integrals may be approximated as:

$$I_n(\tau, \tau^*) \approx \sum_{j=1}^N \int_{t_j}^{t_{j+1}} E_n(|t-\tau|) f(t) dt \quad (C-3)$$

where  $t_1 = 0$ ,  $t_2 = \dots$ ,  $t_{N+1} = \tau^*$

Defining:

$$F_j^n(\tau) = \int_{t_j}^{t_{j+1}} E_n(|t-\tau|) f(t) dt \quad (C-4)$$

yields:

$$I_n(\tau, \tau^*) \approx \sum_{j=1}^N F_j^n(\tau) \quad (C-5)$$

The appropriate quadrature formula is of the form:

$$F_j^n(\tau) = a_j^n(\tau) f_j + a_{j+1}^n(\tau) f_{j+1} \quad (C-6)$$

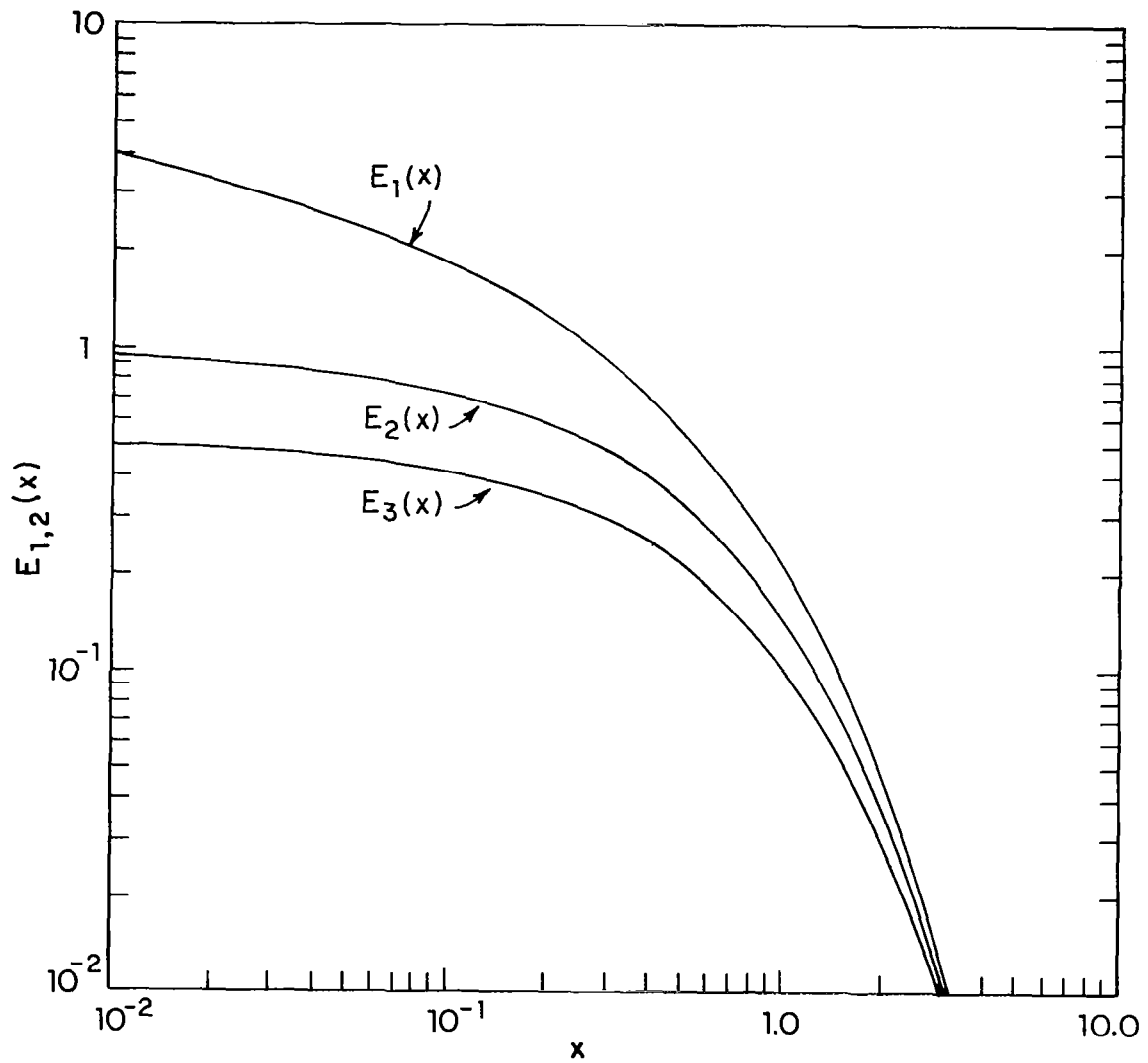


Figure C-1  
Exponential integral functions  $E_1$ ,  $E_2$ ,  $E_3$  (x).

where:

$$f_j = f(t_j) ; f_{j+1} = f(t_{j+1}) \quad (C-7)$$

If piecewise continuous (local linear interpolation) functions are used:

$$f(t) = f_j \left[ 1 - \frac{(t-t_j)}{\Delta t_j} \right] + f_{j+1} \frac{(t-t_j)}{\Delta t_j} \quad (C-8)$$

where

$$\Delta t_j = t_{j+1} - t_j \quad (C-9)$$

Substituting into equation (C-4):

$$\begin{aligned} F_j^n(\tau) = & f_j \int_{t_j}^{t_{j+1}} E_n(|t-\tau|) \left[ 1 - \frac{(t-t_j)}{\Delta t_j} \right] dt \\ & + f_{j+1} \int_{t_j}^{t_{j+1}} E_n(|t-\tau|) \frac{(t-t_j)}{\Delta t_j} dt \end{aligned} \quad (C-10)$$

From equation (C-6):

$$a_j^n = \int_{t_j}^{t_{j+1}} E_n(|t-\tau|) \left[ 1 - \frac{(t-t_j)}{\Delta t_j} \right] dt \quad (C-11)$$

$$a_{j+1}^n = \int_{t_j}^{t_{j+1}} E_n(|t-\tau|) \frac{(t-t_j)}{\Delta t_j} dt \quad (C-12)$$

Note that:

$$a_j^n + a_{j+1}^n = \int_{t_j}^{t_{j+1}} E_n(|t-\tau|) dt \quad (C-13)$$

Expressions (C-11) and (C-12) may be evaluated analytically by using the recurrence relation:

$$E_n(x) dx = -d E_{n+1}(x) \quad (C-14)$$

Taking note of absolute values the constants  $a_j^n$ ,  $a_{j+1}^n$  obtained are:

$$a_j^n(\tau) = E_{n+1}(t_j - \tau) - \frac{1}{\Delta t_j} \left\{ E_{n+2}(t_j - \tau) - E_{n+2}(t_{j+1} - \tau) \right\} \quad (C-15)$$

$$a_{j+1}^n(\tau) = -E_{n+1}(t_{j+1} - \tau) + \frac{1}{\Delta t_j} \left\{ E_{n+2}(t_j - \tau) - E_{n+2}(t_{j+1} - \tau) \right\} \quad (C-16)$$

for  $\tau \leq t_j$  and

$$a_j^n(\tau) = -E_{n+1}(\tau - t_j) - \frac{1}{\Delta t_j} \left\{ E_{n+2}(\tau - t_j) - E_{n+2}(\tau - t_{j+1}) \right\} \quad (C-17)$$

$$a_{j+1}^n(\tau) = E_{n+1}(\tau - t_{j+1}) + \frac{1}{\Delta t_j} \left\{ E_{n+2}(\tau - t_j) - E_{n+2}(\tau - t_{j+1}) \right\} \quad (C-18)$$

for  $\tau \geq t_{j+1}$ .

## APPENDIX D

### Numerical Procedures for Diurnal Calculation

The distribution of an atmospheric trace gas is governed by the continuity equation,

$$\frac{\partial n}{\partial t}(i) + \frac{\partial \phi}{\partial z}(i) = P(i) - L(i)n(i) \quad (D-1)$$

and the flux equation

$$\phi(i) = -KN \frac{\partial}{\partial z} \left( \frac{n(i)}{N} \right) \quad (D-2)$$

where  $n(i)$  is the number density of the  $i^{\text{th}}$  species,  $\phi(i)$  the vertical flux,  $P(i)$  and  $L(i)n(i)$  the chemical production and loss terms,  $K$  the eddy diffusion coefficient and  $N$  is the total air number density. In general, the chemical production and loss terms depend on other species. Equations (D-1) and (D-2) represent a system of time dependent, coupled and nonlinear differential equations with a wide range of time scales ( $10^{-3}$ - $10^6$  sec) appropriate for various species of interest.

For many applications, such as the interconversion of active chemical species, the transport term,  $\partial\phi/\partial z$ , is orders of magnitude smaller than the chemical terms and may therefore be neglected. Thus, equation (D-1) reduces to

$$\frac{dn(i)}{dt} = P(i) - L(i)n(i) \quad (D-1')$$

subject to periodic boundary conditions [i.e.,  $n(i, t=0) = n(i, t=T)$ , where  $T = 1$  day].

Equation (D-1) is replaced by a finite difference equation (Wofsy, 1977),

$$n_{\ell+1}(i) - n_{\ell}(i) = [P_{\ell+1}(i) - L_{\ell+1}(i)n_{\ell+1}(i)] \Delta t \quad (D-3)$$

where  $l$  is the time index.

Equation (D-3) represents a fully-implicit scheme and must be solved by an interactive algorithm at each time step. It can be easily shown that the finite difference scheme equation (D-3) has the following important properties:

- 1) satisfying mass conservation at every time step;
- 2) stable for both P and L at every time step.

Equation (D-3) is used to solve for the concentrations of  $O(^3P)$ ,  $O(^1D)$ ,  $O_3$ ,  $NO$ ,  $NO_2$ ,  $HNO_3$ ,  $NO_3$ ,  $N_2O_5$ ,  $Cl$ ,  $ClO$ ,  $HCl$ ,  $ClONO_2$ ,  $H$ ,  $OH$ ,  $HO_2$ ,  $H_2O_2$ . For a species with chemical time constant shorter than a day, only a few days are required to achieve periodic boundary conditions. However, for species with chemical times significantly longer than one day, over a hundred model days are usually required to achieve periodic boundary conditions. We may remedy this situation by setting the initial conditions

$$n(i, t=0) = \frac{\int_0^T P(i,t) \exp[-\int_s^T L(i,s') ds'] ds}{1 - \exp[-\int_0^T L(i,s') ds']} \quad (D-4)$$

where  $T = 1$  day. Clearly, for long-lived species the loss frequency  $L(i,t)$  satisfying

$$\int_0^T L(i,t) dt \ll 1 \quad (D-5)$$

Equation (D-4) reduces to

$$n(i, t=0) = \frac{\int_0^T P(i,t) dt}{\int_0^T L(i,t) dt} \quad (D-4')$$

In fact, if equation (D-5) is satisfied, then we have

$$n(i,t) = n(i, t=0) \text{ for } 0 \leq t \leq T$$

This procedure of adjusting initial conditions at the beginning of each model day greatly reduces the number of model days required for relaxation.

## APPENDIX E

### Initialization of Lagrangian Trajectory

[The content of this Appendix is based on work from Tung, private communication.]

Let  $\xi'(t, \overset{\circ}{\underline{x}})$  be the particle displacement trajectory of the particles located at coordinates  $\overset{\circ}{\underline{x}}$  at time  $t_0$ . It follows that the position of the particle at subsequent time  $t$  is given by

$$\underline{\tilde{S}}(t, \overset{\circ}{\underline{x}}) = \overset{\circ}{\underline{x}} + \underline{\tilde{\xi}}'(t, \overset{\circ}{\underline{x}}) \quad (\text{E-1})$$

We define the coordinate  $\underline{\tilde{x}}_0$ , and  $\underline{\tilde{\xi}}(t, \underline{\tilde{x}}_0)$  by

$$\underline{\tilde{x}}_0 = \overline{\underline{\tilde{S}}(t, \overset{\circ}{\underline{x}})} \quad (\text{E-2})$$

$$\underline{\tilde{\xi}}(t, \underline{\tilde{x}}_0) = \underline{\tilde{S}}(t, \overset{\circ}{\underline{x}}) - \underline{\tilde{x}}_0 \quad (\text{E-3})$$

Note that equation (E-3) implies

$$\overline{\underline{\tilde{\xi}}(t, \underline{\tilde{x}}_0)} = 0 \quad (\text{E-4})$$

If in addition  $\underline{\tilde{\xi}}(t, \underline{\tilde{x}}_0)$  satisfies equation (3.3.2b),  $\underline{\tilde{\xi}}$  can then be used as a disturbance induced displacement vector in Lagrangian averaging.

The Eulerian velocity  $\underline{\tilde{v}}(t, \underline{\tilde{S}})$  is given by

$$\frac{d}{dt} \underline{\tilde{S}} = \underline{\tilde{v}}(t, \underline{\tilde{S}}) \quad (\text{E-5})$$

From equation (E-3) it follows that

$$\begin{aligned}
\bar{v}(t, \bar{S}) &= \frac{d}{dt} \bar{x}_o + \frac{d}{dt} \bar{\xi}(t, \bar{x}_o) & (E-6) \\
&= \bar{v}(t, \bar{x}_o) + \frac{\partial}{\partial t} \bar{\xi}(t, \bar{x}_o) + \frac{d\bar{x}_o}{dt} \cdot \nabla_{\bar{x}_o} \bar{\xi}(t, \bar{x}_o) \\
&= \bar{v}(t, \bar{x}_o) + \left( \frac{\partial}{\partial t} + \bar{v}(t, \bar{x}_o) \cdot \nabla_{\bar{x}_o} \right) \bar{\xi}(t, \bar{x}_o)
\end{aligned}$$

If we apply the Eulerian mean operator to equation (E-6) we obtain

$$\overline{\bar{v}(t, \bar{S})} = \bar{v}(t, \bar{x}_o) \quad , \quad (E-7)$$

since  $\overline{\bar{x}_o} = \bar{x}_o \rightarrow \overline{\bar{v}(t, \bar{x}_o)} = \bar{v}(t, \bar{x}_o)$  and  $\overline{\bar{\xi}(t, \bar{x}_o)} = 0$ .

However, from the definition of the Lagrangian mean, we have

$$\overline{\bar{v}(t, \bar{S})} = \overline{\bar{v}(t, \bar{x}_o) + \bar{\xi}(t, \bar{x}_o)} = \bar{v}^L \quad (E-8)$$

Combining equations (E-7) and (E-8), we obtain

$$\bar{v}^L = \bar{v}(t, \bar{x}_o)^\dagger \quad (E-9)$$

Substituting equation (E-9) into equation (E-6), we have

$$\left( \frac{\partial}{\partial t} + \bar{v}^L \cdot \nabla_{\bar{x}_o} \right) \bar{\xi}(t, \bar{x}_o) = \bar{v}(t, \bar{S}) - \bar{v}^L(t, \bar{x}_o) \quad (E-10)$$

---

<sup>†</sup>The result here is similar to that presented in Andrew and McIntyre (1978) pp. 615-616.

which is identical to equation (3.3.2b). Thus,  $\xi(t, \underline{x}_o)$  can be used for Lagrangian averaging and is directly related to trajectory motion of the particles.

Note that in the above definition, the GLM operations depend on the choice of time  $t_o$  at which the particles are labelled by  $\underline{x}_o$ . In terms of  $\xi(t, \underline{x}_o)$ , this is characterized by the fact that  $\xi(t_o, \underline{x}_o) = 0$ . A different initialization, i.e., choice of  $t_o^*$  and  $\underline{x}_o^*$  can lead to different averaged values for some quantities (see McIntyre, 1979).

## APPENDIX F

### High Altitude Aircraft Emissions

As a consequence of projected high altitude aircraft operations, appreciable quantities of combustion products of fossil-origin fuels may be emitted into the ambient atmosphere. Typical aviation fuels consist primarily of a mixture of higher hydrocarbon petroleum distillates (e.g., Jet A - "kerosene",  $C_9H_{20}$ - $C_{16}H_{34}$ ; Jet B - "naptha",  $C_6H_{14}$ - $C_7H_{16}$ ) and inherent residual impurities such as sulfur and heavy metals. Exhaust product constituents may be categorized as: (1) products of complete combustion including water vapor ( $H_2O$ ) and carbon dioxide ( $CO_2$ ), (2) products of incomplete combustion including carbon monoxide ( $CO$ ) and hydrocarbons ( $HC$ ), and (3) products due to residual impurities such as sulfur ( $S$ ) and its oxides ( $SO_2$ ), and oxides of nitrogen ( $NO_x$ ). This discussion focuses on the evaluation of aircraft related yearly source strengths ( $MT\ yr^{-1}$ ) for  $H_2O$ ,  $CO$ ,  $S$  and  $NO_x$ . Total emissions are dependent both on intrinsic emission characteristics of individual aircraft/engine configurations as given by the emission index and fleet related modes of operation including total number of aircraft and cruising time per day.

Emissions of individual pollutants and pollutant groups are quantified in terms of relevant emission indices, EI, which are the number of grams of pollutant produced for each kilogram of fuel consumed. In general, EI are dependent on engine type, mode of operation (cruise, idle, etc.), cruise power setting, flight altitude, and cruising speed. However, EI have been recommended for typical cruise conditions for performing atmospheric model calculations (Grobman and Ingebo, 1974).

An upper limit to the emission index may be evaluated

based on stoichiometric considerations assuming perfect combustion efficiency. For example, for a kerosene mixture (Jet A), a water vapor emission index  $EI(H_2O)$  of about 1400 g/kg fuel is predicted. Higher order distillates such as naphtha produce slightly higher yields of  $H_2O^*$ . Measurements indicate slightly lower values of emission index (CIAP, 1975) and 1250 g/kg fuel is the recommended value for cruise conditions and all engine types.

The emission of sulfur, primarily as  $SO_2$ , is determined by the fuel stock sulfur content which is expressed as percent by weight, % (w/w). This abundance is controllable by implementing available fuel desulfurization techniques. Current average aviation fuel sulfur contents are 0.05 percent (w/w) with a maximum allowable value of 0.30 percent (w/w) (CIAP, 1975). These values suggest typical and worse case  $EI(S)$  of 0.5 and 3.0 g/kg fuel, respectively.

Elevated combustion zone temperatures and the presence of radicals such as O, N, and OH facilitate the formation of oxides of nitrogen which would not be energetically favored under ambient conditions. Since  $NO_x$  emissions are highly dependent on operating conditions, values at cruise conditions are assumed. It is necessary to distinguish between near term (present day) and far term design concepts in assigning  $NO_x$  emission indices (Poppoff et al., 1978) since future technological advances are planned to reduce  $NO_x$  emissions by a factor of 6 (Reck, 1978).

---

\* It is notable that  $H_2O$  emission indices for coal-derived fuels suggested for implementation in certain advanced SST (ASST) design concepts (Witcofski, 1978) are significantly higher. For example, synthetic liquid natural gas (SYN-LNG) has a  $EI(H_2O)$  of about 2300 g/kg fuel while that for liquid hydrogen ( $LH_2$ ) is near 9000 g/kg fuel. On an energy equivalent basis, these emissions are 60 and 160 percent higher, respectively, than Jet A (Witcofski, 1978).

Typical near term emissions [ $EI(NO_x) = 18 \text{ g/kg fuel}$ ] are based on the Olympus 593 engine as described in Lohmann and Riecke (1977); this value is consistent with that given by Grobman and Ingebo (1974). The corresponding far term technology estimate is  $3 \text{ g/kg fuel}$ . Values of  $EI(NO_x)$  are summarized in Table F-1.

Assessment of potential perturbations to atmospheric chemistry and global climate due to aircraft exhaust emissions is dependent on the total fleet-derived source strength,  $R_i (\text{MT yr}^{-1})$  for each pollutant species, which is defined as

$$R_i = (EI)_i M \phi T_f / 10^{12} \quad (\text{F-1})$$

where  $M$  is the number of aircraft in the proposed nominal fleet,  $\phi (\text{kg fuel hr}^{-1})$  the engine fuel flow rate at cruise altitude and  $T_f (\text{hr/yr})$  the yearly cruise time in hours for each aircraft. Typical source strengths based on the given emission indices and a nominal fleet of 500 aircraft are evaluated and presented in Table F-1. In these calculations, we assume an average engine fuel flow rate of  $3.78 \times 10^4 \text{ kg fuel hr}^{-1}$ , which is based on a "Type A" aircraft as defined in Poppoff et al. (1978) and described in Baber and Swanson (1976). Cruise time is taken to be 7 hr per day per aircraft.

Equivalent aircraft production rates  $P_a$  are evaluated assuming injection of  $NO_x$  as pure  $NO^\dagger$  and distributing it uniformly over the globe in a 1 km thick spherical shell (to be centered at the cruise altitudes of 15.2 and

---

<sup>†</sup>The assumption of pure  $NO$  production is only approximately true. The volume fraction of  $NO$ , however, is equal to 90-95 percent (CIAP, 1975) of the total  $NO_x$  emissions.

18.3 km). Based on these assumptions, the given aircraft characteristics are converted to equivalent production rates using:

$$P_a = (7.82 \times 10^{-2}) M(EI) \quad (F-2)$$

Calculations based on equations (F-1) and F-2) for  $NO_x$  are summarized in Table F-2. Ozone perturbation sensitivity analysis will be performed on these values.

## REFERENCES

- Andrew, D.G., and McIntyre, M.Z. (1978) An Exact Theory of Non-Linear Waves in a Lagrangian-Mean Flow. J. Fluid Mech., 89, 609.
- Anderson, D.E., and Meier, R.R. (1979) Effects of Anisotropic Multiple Scattering on Solar Radiation in the Troposphere and Stratosphere. Appl. Optics, 18, 1955.
- Antyufeyev, V.S., and Nazararaliyev, M.A. (1973) A New Modification of the Monte Carlo Method for Solution of Problems in the Theory of Light Scattering in Spherical Atmosphere. Atmos. Oceanic Phys., 9, 463.
- Baber, H.T., Jr., and Swanson, E.E. (1976) Advanced Supersonic Technology Concept AST-100 Characteristics Development in a Baseline-Update Study. NASA TM X-72815.
- Borucki, W.J., Whitten, R.C., Watson, V.R., Woodward, H.T., Niegel, C.A., Capone, C.A., and Becker, T. (1976) Model Prediction of Latitude Dependent Ozone Due to Supersonic Operations. AIAA J., 14, 1738.
- Boughner, R., Larsen, J.C., and Natarajan, M. (1980) The Influence of NO and ClO Variations at Twilight or the Interpretation of Solar Occultation Measurements. Geophysical Res. Letters, Vol. 7, No. 4, Apr. 1980, pp. 231-234.
- Buijs, H.L., Vail, G.L., Tremblay, G., and Kendall, D.J.W. (1980) Measurement of the Volume Mixing Ratios for HCl and HF in the Stratosphere. Geophysical Res. Letters, Vol. 7, No. 3, Mar. 1980, pp. 205-208.

- Busbridge, I.W. (1960) *The Mathematics of Radiative Transfer*. Cambridge Univ. Press.
- Callis, L.B., Ramanathan, V., Boughner, R.E., and Barkstrom, B.R. (1975) *The Stratosphere: Scattering Effects, A Coupled 1-D Model, and Thermal Balance Effects*. Fourth Conference on CIAP, U.S. DOT, 224-233.
- Callis, L.B. (1974) *The Importance of Rayleigh Scattering on Photochemical Processes in the Stratosphere*. Paper presented at the 1974 Fall Annual Meeting, Dec. 12-17, AGU.
- Chandrasekhar, S. (1960) Radiative Transfer. Dover.
- Chang, J.S. (1976) In Halocarbons: Effects on Stratospheric Ozone. NAS Report, Washington, D.C.
- Chapman, S. (1931) *The Absorption and Dissociative or Ionizing Effect of Monochromatic Radiation in an Atmosphere on a Rotating Earth. II, Grazing Incidence*. Proc. Phys. Soc., 43, 483.
- Chu, W.P., and McCormick, M.P. (1979) *Inversion of Stratospheric Aerosol and Gaseous Constituents from Spacecraft Solar Extinction Data in the .38-1.0  $\mu$ m Wavelength Region*. Appl. Optics, 18, 1404.
- Collins, D.G., and Wells, M.B. (1965) *Monte Carlo Codes for Study of Light Transport in the Atmosphere*. Rep. RRA-T54, Vols. 1 and 2, Fort Worth, TX, Radiation Research Assoc.

- Crutzen, P.J. (1971) Ozone Production Rates in an Oxygen-Hydrogen-Nitrogen Oxide Atmosphere. J. Geophys. Res., 76, 7311.
- Crutzen, P.J. (1970) The Influence of Nitrogen Oxides on the Atmospheric Ozone Content. Quart. J. Roy. Meteor. Soc., 96, 320.
- Danielson, E.F. (1968) Stratospheric-Tropospheric Exchange Based on Radioactivity, Ozone and Potential Vorticity. J. Atmos. Sci., 25, 502.
- Duewer, W.H., Wuebbles, D.J., Ellsaesser, H.W., and Chang, J.S. (1977) NO<sub>x</sub> Catalytic Ozone Destruction: Sensitivity to Rate Coefficients. J. Geophys. Res., 82, 935.
- Dunkerton, T. (1978) On the Mean Meridional Mass Motions of Stratosphere and Mesosphere. J. Atmos. Sci., 35, 2325.
- Edlen, B. (1966) Meteorologia, 2, 12.
- English, J.M., Oliver, R.C., and Forney, A.K. CIAP (1975) Propulsion Eggluents in the Stratosphere. DOT TST-75-52. U.S. Dept. of Transportation.
- Evans, W.V., Kerr, J.B., Wardle, D.I., McConnell, J.C., Ridley, B.A., and Schiff, H.I. (1976) Intercomparison of NO, NO<sub>2</sub>, and HNO<sub>3</sub> Measurements with Photochemical Theory. Atmosphere, 14, 189.
- Farmer, C.B., and Raper, O.F. (1977) The HF:HCl Ratio in the 14-38 km Region of the Stratosphere. Geophys. Res. Lett., 4, 527.

- Fitzmaurice, J.A. (1964) Simplification of the Chapman Function for Atmospheric Attenuation. Appl. Optics., 3, 640.
- Fontanella, J.C., Girand, A., Gramont, L., and Louisnard, N. (1975) Vertical Distribution of NO, NO<sub>2</sub>, and HNO<sub>3</sub> As Derived From Stratospheric Absorption Infrared Spectra. Appl. Optics, 14, 825.
- Fymat, A. (1977) Inversion Methods in Temperature and Aerosol Remote Sounding: Their Commonality and Differences, and Some Unexplored Approaches. Inversion Methods in Atmospheric Remote Sounding. A. Deepak (ed.) Academic Press, 429-463.
- Graham, R.A., Winer, A.M., and Pitts, J.N., Jr. (1978) Pressure and Temperature Dependence of the Unimolecular Decomposition of HO<sub>2</sub>NO<sub>2</sub>. J. Chem. Phys., 68, 4505.
- Green, A.E.S., and Martin, J.D. (1966) Generalized Function in The Middle Ultraviolet: Its Science and Technology. A.E.S. Green (ed.) Wiley, 140-157.
- Green, J.S.A. (1970) Transfer Properties of Large Scale Eddies and the General Circulation of the Atmosphere. Quart. J. Meteor. Soc., 96, 157.
- Grobecker, A.J., Coronti, S.C., and Cannon, R.H., Jr. CIAP (1974) The Effects of Stratospheric Pollution by Aircraft. DOT-TST-75-50, U.S. Dept. of Transportation.

- Grobman, J., and Ingebo, R.D. (1974) Forecast of Jet-Engine Exhaust Emissions for Future High Altitude Commercial Aircraft. Proc. Third Conference on the Climatic Impact Assessment Program. Rep. No. DOT-TSC-OST-74-15, U.S. Dept. of Transportation.
- Hansen, J.E., and Travis, L.D. (1974) Light Scattering in Planetary Atmospheres. Space Sci. Rev., 16, 527.
- Harris, J.E. (1978) Ratio of HNO<sub>3</sub> to NO<sub>2</sub> Concentration in Daytime Stratosphere. Nature, 274, 235.
- Harris, J.E., Moss, D.G., Swann, N.R., Neill, G.F., and Gildwang, P. (1976) Simultaneous Measurements of H<sub>2</sub>O, NO<sub>2</sub> and HNO<sub>3</sub> in the Daytime Stratosphere From 15 to 35 km. Nature, 259, 300.
- Harris, J.E. (1976) The Distribution of Water Vapor in the Stratosphere. Rev. Geophys. Space Phys., 14, 565.
- Harwood, R.S., and Pyle, J.A. (1977) Studies of the Ozone Budget Using a Zonal Mean Circulation Model and Linearized Photochemistry. Quart. J. Roy. Meteorol. Soc., 103, 319.
- Harwood, R.S., and Pyle, J.A. (1975) A Two-Dimensional Mean Circulation Model for the Atmosphere Below 80 km. Quart. J. Roy. Meteorol. Soc., 101, 723.
- Herman, J.R. (1979) The Response of Stratospheric Constituents to a Solar Eclipse, Sunrise and Sunset. J. Geophys. Res., 84, 3701.

- Hidalgo, H., and Crutzen, P.J. (1977) The Tropospheric and Stratospheric Composition Perturbed by NO<sub>x</sub> Emissions of High-Altitude Aircraft. J. Geophys. Res., 82, 5833.
- Hinds, M.K. (1979) Studies of Residence Times of Chlorofluorocarbons Using a Two-Dimensional Model. Meteor. Mag., 108, 22.
- Holton, J.R. (1975) The Dynamics Meteorology of the Stratosphere and Mesosphere. Mesosphere. Meteor. Monog., 15, No. 37.
- Howard, C.J., and Evenson, K.M. (1977) Kinetics of the Reaction of HO<sub>2</sub> with NO. Geophys. Res. Lett., 4, 437.
- Irvine, W.M. (1965) Multiple Scattering by Large Particles. Ap. J., 142, 1563.
- Johnston, H.S. (1971) Reduction of Stratospheric Ozone by Nitrogen Oxide Catalysts from Supersonic Transport Exhaust. Science, 173, 517.
- Kida, H. (1977) A Numerical Investigation of the Stratospheric General Circulation and Stratospheric Tropospheric Mass Exchange, II. Lagrangian Motion of the Atmosphere. J. Meteor. Soc. Japan, 55, 71.
- Krishnamurti, T.N. (1961) The Subtropical Jet Stream of Winter. J. Meteor., 18, 172.
- Lacis, A.A., and Hansen, J.E. (1974) A Parameterization for the Absorption of Solar Radiation in the Earth's Atmosphere. J. Atmos. Sci., 31, 118.

Lenoble, J. (ed.) (1977) Standard Procedures to Compute Atmospheric Radiative Transfer in a Scattering Atmosphere. IAMAP, Boulder, CO.

Loewenstein, M., Borucki, W.J., Savage, H.F., Borucki, J.E., and Whitten, R.C. (1978) Geographical Variations of NO and O<sub>3</sub> in the Lower Stratosphere. J. Geophys. Res., 83, 1875.

Logan, J.A., Prather, M.J., Wofsy, S.C., and McElroy, M.B. (1978) Atmospheric Chemistry: Respond to Human Influence. Phil. Trans. Roy. Soc., 290, 187.

Lohmann, R.A., and Riecke, G.T. (1977) Analytical Screening of Low Emissions, High Performance Duct Burners for Supersonic Cruise Aircraft Engines. NASA CR-135157.

Lorentz, E.N. (1967) The Nature and Theory of the General Circulation of the Atmosphere. WMO No. 218.

Louis, J.F., London, J., and Danielson, E.F. (1974) The Interaction of Radiation and Meridional Circulation of the Stratosphere Proceedings of the IAMAP/IAPSO Combined First Special Assemblies, Melbourne, Australia, Vol. II, 1205.

Luther, F.M. (1973) Monthly Mean Values of Eddy Diffusion Coefficients in the Lower Stratosphere. AIAA paper 73, 495. AIAA/AMS Conference, Denver, CO.

Luther, F.M., and Gelinas, R.J. (1976) Effect of Molecular Multiple Scattering and Surface Albedo on Atmospheric Photodissociation Rates. J. Geophys. Res., 81, 1125.

- Luther, F.M., Wuebbles, D.J., Duewer, W.H., and Change, J.S. (1978) Effect of Multiple Scattering on Species Concentrations and Model Sensitivity. J. Geophys. Res., 83, 3563.
- Mahlman, J.D. (1975) Some Fundamental Limitations of Simplified Transport Model. Proceedings of the Earth CIAP Conference. Ref. 132. U.S. Dept. of Transportation.
- Mahlman, J.D. (1973) On the Maintenance of Polar Front Jet Stream. J. Atmos. Sci., 30, 544.
- Mahlman, J.D. (1969) Heat Balance and Mean Meridional Circulation in Polar Stratosphere During Sudden Warmings in January, 1958. Mon. Wea. Rev., 97, 534.
- Mahlman, J.D., Levy, H., II, and Maxim, W.J. (1980) Three-Dimensional Traces Structure and Behavior as Simulated in Two Ozone Precursor Experiments. J. Atmos. Sci., 37, 655.
- Marchuk, G.I., and Mikhailov, G.A. (1967) Results of the Solution of Some Problems in Atmospheric Optics by a Monte Carlo Method. Atmos. Oceanic Phys., 3, 227.
- Matsuno, T. (1980) Lagrangian Motion of Air Parcels in the Stratosphere in the Presence of Planetary Waves. Pure Appl. Geophys., 118, 189.
- Matsuno, T., and Nakamura, K. (1979) The Eulerian and Lagrangian Mean Meridional Circulations in the Stratosphere at Time of Sudden Warming. J. Atmos. Sci., 36, 680.

McConnell, J.C., and Evans, W.F.J. (1978) Implications of Low Stratospheric Hydroxyl Concentrations for CFM and SST Scenario Calculations of Ozone Depletion. EOS Trans. AGU, 59, 1978.

McDonald, J. (1971) Presentation Before the Department of Commerce Technical Advisory Board on Environmental Aspects of the Supersonic Transport, Boulder, CO., March 17-18.

McElroy, M.B., and McConnell, J.C. (1971) Nitrous Oxide: A Natural Source of Stratospheric NO. J. Atmos. Sci., 28, 1095.

McElroy, M.B., Wofsy, S.C., Penner, J.E., and McConnell, J.C. (1974) Atmosphere Ozone: Possible Impact of Stratospheric Aviation. J. Atmos. Sci., 31, 287.

McIntyre, M.E. (1979) Towards the Lagrangian Mean Description of Stratospheric Circulation and Chemical Transport. To appear in Phil. Trans. Roy. Soc. A.

McKee, T.B., Whitman, R.I., and Lambiotte, J.J. (1969) A Technique to Infer Atmospheric Temperature Using Horizon Radiance Profiles. NASA TN D-5068.

Menzies, R.T. (1979) Remote Measurements of ClO in the Stratosphere. Geophys. Res. Lett., 6, 151.

Molina, L.T., and Molina, M.J. (1980) UV Absorption of Cross-Section of HO<sub>2</sub>NO<sub>2</sub> Vapor. Report to U.S. Dept. of Trans. High Altitude Pollution Program Rep. No. FAA-EE-80-07.

- Murgatroyd, R.J., and Singleton, F.S. (1961) Possible Meridional Circulations in Top Stratosphere and Mesosphere. Quant. J. Meteor. Soc., 87, 125.
- Nagel, M.R., Quenzel, H., Kweta, W., and Wendling, R. (1978) Daylight Illumination-Color-Contrast Tables. Academic Press.
- NASA (1979) The Stratosphere: Present and Future. R.D. Hudson (ed.) NASA Ref. Publ. 1049, NASA Goddard Space Flight Center.
- NASA (1977) Chlorofluoromethanes and the Stratosphere. NASA RP-1010, Washington, D.C.
- Newell, R.A., Wallace, J.M., and Mahaney, J.R. (1966) The General Circulation of the Atmosphere and its Effects on the Movement of Trace Substances. II. Tellus, 18, 363.
- Nicolet, M., and Vergison (1971) L'oxyde Azoteux dans la Straospere. Aeron. Acta., A-91.
- Oort, A.H., and Rasmussen, E.M. (1971) Atmospheric Circulation Statistics. NOAA Prof. Paper 5. National Oceanic and Atmospheric Administration.
- Penndorf, R. (1957) Tables of the Refractive Index for Standard Air and the Rayleigh Scattering Coefficient for the Spectral Region Between 0.2 and 20.0  $\mu\text{m}$  and Their Application to Atmospheric Optics. J. Opt. Soc. Am., 47, 176.

- Phillips, D.L. (1962) A Technique for the Numerical Solutions at Certain Integral Equations of the First Kind. J. Assoc. Comput. Mach., 9, 97.
- Plumb, R.A. (1979) Eddy Fluxes of Conserved Quantities by Small Amplitude Waves. J. Atmos. Sci., 36, 1699.
- Poppoff, I.G., Whitten, R.C., Turco, R.P., and Capone, L.A. (1978) An Assessment of the Effects of Supersonic Aircraft Operations on the Stratospheric Ozone Content. NASA RP-1026.
- Reck, G.M. (1978) In An Assessment of the Effect of Supersonic Aircraft Operations on the Stratospheric Ozone Content. NASA RP-1026.
- Reed, R.J., and German, K.E. (1965) A Contribution to the Problem of Stratospheric Diffusion by Large-Scale Mixing. Mon. Wea. Rev., 93, 313.
- Riehl, H., and Fultz, D. (1957) Jet Stream and Large Waves in a Steady Rotating-Dishpan Experiment: Structure of the Circulation. Quart. J. Roy. Meteor. Soc., 83, 215.
- Roble, R.G., and Hays, P.B. (1972) A Technique for Recovering the Vertical Number Density Profile of Atmospheric Gases from Planetary Occultation Data. Planet. Space Sci., 20, 1727.
- Russell, J.M., and Drayson, S.R. (1972) The Influence of Atmospheric Ozone Using Satellite Horizon Measurements in the  $1042 \text{ cm}^{-1}$  Band. J. Atmos. Sci., 29, 376.

- Russell, J.M., Park, J.H., and Drayson, S.R. (1977) Global Monitoring of Stratospheric Halogen Compounds from a Satellite Using Gas Filter Spectroscopy in the Solar Occultation Mode. Appl. Opt., 16, 607.
- Sawyer, J.S. (1965) The Dynamical Problems of the Lower Stratosphere. Quart. J. Roy. Meteor. Soc., 91, 407.
- Selby, J.E.A., and McClatchey, R.A. (1972) Atmospheric Transmittance from 0.25 to 28.5 Micrometers: Computer Code LOWTRAN 2. Tech. Rep. AFCRL-72-0745, Air Force Geophys. Labs.
- Shettle, E.P., and Green, A.E.S. (1974) Multiple Scattering Calculation of the Middle Ultraviolet Reaching the Ground. Appl. Opt., 13, 1967.
- Smith, F.L., III, and Smith, C. (1972) Numerical Evaluation of Chapman's Grazing Incidence Integral  $Ch(X, \chi)$ . J. Geophys. Res., 77, 3592.
- Snider, D.E. (1975) Refractive Effects in Remote Sensing of the Atmosphere with Infrared Transmission Spectroscopy. J. Atmos. Sci., 32, 2178.
- Sobolev, V.V. (1975) Light Scattering in Planetary Atmospheres. Pergamon Press, NY.
- Swider, W., Jr. (1964) The Determination of the Optical Depth at Large Solar Zenith Distances. Planet Space Sci., 12, 761.
- Sze, N.D. (1976) Variational Methods in Radiative Transfer Problems. J. Quant. Spectros. Radiat. Trans., 16, 763.

- Sze, N.D. (1978) Stratospheric Fluorine: A Comparison Between Theory and Measurements. Geophys. Res. Lett., 5, 781.
- Sze, N.D., and Ko, M.K.W. (1980) Photochemistry of COS, CS<sub>2</sub>, CH<sub>3</sub>Sch<sub>3</sub>, and H<sub>2</sub>S: Implications for the Atmospheric Sulfur Cycle. Atmos. Environ., 14, 1223.
- Sze, N.D., and Ko, M.K.W. (1979) CS<sub>2</sub> and COS in Stratospheric Sulfur Budget. Nature, 280, 308.
- Turco, R.P., Whitten, R.C., Poppoff, I.G., and Capone, L.A. (1978) SSTs, Nitrogen Fertilizer and Stratospheric Ozone. Nature, 276, 805.
- Twomey, S. (1950) On the Numerical Solution of Fredholm Integral Equations of the First Kind by the Inversion of the Linear System Produced by Quadrature. J. Assoc. Comput. Mach., 10, 99.
- U.S. Standard Atmospheric Supplement (1966), U.S. Government Printing Office, Washington, D.C.
- Vupputuri, R.K.R. (1973) Numerical Experiments on the Steady State Meridional Structure and Ozone Distribution in the Stratosphere. Mon. Wea. Rev., 101, 510.
- Vupputuri, R.K.R. (1979) The Structure of the Natural Stratosphere and the Impact of Chlorofluoromethanes on the Ozone Layer Investigated in a 2-D Time Dependent Model. Pure and Appl. Geophys., 117, 448.
- Wang, W.C., and Sze, N.D. (1980) Coupled Effects of Atmospheric N<sub>2</sub>O and O<sub>3</sub> on the Earth's Climate. Nature, Vol. 286, 589.

- Wang, W.C., Yung, Y.L., Lacis, A.A., Mo. T., and Hansen, J.E. (1976) Greenhouse Effects Due to Man-Made Perturbations of Trace Gases. Science, 194, 685.
- Whitney, C. (1977) Extending Radiative Transfer Models by Use of Bayes' Rule. J. Atmos. Sci., 34, 766.
- Whitney, C.K., and Malchow, H.L. (1978) Study of Radiative Transfer in Scattering Atmosphere. AFGL-TR-78-0101.
- Whitney, C.K., Var, R.E., and Gray, C.R. (1973) Research Into Radiative Transfer Modeling and Applications- Atmospheric Physics. AFCRL-TR-73-0420.
- Whitten, R.C., Borucki, W.J., Watson, V.R., Shimazaki, T., Woodward, H.T., Niegel, C.A., Capone, L.A., and Becker, T. (1977). The NASA Ames Research Center One- and Two-Dimensional Stratospheric Models. Part 2: The Two-Dimensional Model. NASA TP-1003.
- Widhopf, G.F. (1975) A Two-Dimensional Photochemical Model of the Stratosphere Including Initial Results of Inert Tracer Studies. Proc. Fourth Conf. on CIAP. T. Hand, and A. Broderick (eds.) DOT-TSC-OST-75-38, 316.
- Wiin-Neilsen, A., and Sela, J. (1971) On the Transport of Quasi-Geostrophic Potential Vorticity. Mon. Weath. Rev., 99, 447.
- Wilkes, M.V. (1954) A Table of Chapman's Grazing Incidence Integral  $Ch(X, \chi)$ . Proc. Phys. Soc., B67, 304.

Witcofski, R.D. (1978) Progress in Coal Derived Fuels for Aviation Systems. NASA TM-78696.

Wofsy, S.C. (1976) Interactions of CH<sub>4</sub> and CO in the Earth's Atmosphere. Ann. Rev. Earth Planet Sci., 4, 441.

Wofsy, S.C., and McElroy, M.B. (1973) On Vertical Mixing In the Upper Stratosphere and Lower Mesosphere. J. Geophys. Res., 78, 2819.

1. Report No. NASA CR-3410	2. Government Accession No.	3. Recipient's Catalog No.	
4. Title and Subtitle ATMOSPHERIC STUDIES RELATED TO AEROSPACE ACTIVITIES AND REMOTE SENSING TECHNOLOGY		5. Report Date March 1981	6. Performing Organization Code
		8. Performing Organization Report No.	
7. Author(s) N. D. Sze, R. G. Isaacs, M. Ko, and M. B. McElroy		10. Work Unit No.	
9. Performing Organization Name and Address Atmospheric and Environmental Research, Inc. 872 Massachusetts Avenue Cambridge, Massachusetts 02139		11. Contract or Grant No. NAS1-15943	
		13. Type of Report and Period Covered Contractor Report August 1979-May 1980	
12. Sponsoring Agency Name and Address National Aeronautics and Space Administration Washington, DC 20546		14. Sponsoring Agency Code	
		15. Supplementary Notes Langley Technical Monitor: Linwood B. Callis, Jr. Final Report	
16. Abstract This report describes the results of a three-phase program of atmospheric studies related to aerospace activities and remote sensing technology. Parallel investigations were conducted relating to: (a) the sensitivity of 1-D photochemical model simulated column ozone perturbations due to a projected fleet of 1000 aircraft cruising 7 hours per day at altitudes of 15-16 and 18-19 km to uncertainties in kinetic rate constant data determining modeled OH concentrations and eddy diffusivity profile parameterization, (b) a comparison of the inherent strengths and weaknesses of Eulerian and Lagrangian averaging processes in the development of multidimensional models and investigation of approaches to applying the Generalized Lagrangian Mean (GLM) formalism to zonal-mean models, (c) the role of multiple scattering and Earth curvature in the evaluation of diurnally dependent photodissociation rates and trace species variations and approaches for including a priori information on diurnal trace species variation in occultation based inversion algorithms.			
17. Key Words (Suggested by Author(s)) Ozone Stratosphere Photochemistry Transport Radiative Transfer		18. Distribution Statement  Unclassified - Unlimited  Subject Category 46	
19. Security Classif. (of this report) Unclassified	20. Security Classif. (of this page) Unclassified	21. No. of Pages 140	22. Price A07